GUIDING OF ELECTROMAGNETIC ENERGY IN SUBWAVELENGTH PERIODIC METAL STRUCTURES

Thesis by

Stefan Alexander Maier

In Partial Fulfillment of the Requirements

for the Degree of

Doctor of Philosophy

California Institute of Technology

Pasadena, California

2003

(Defended January 24th 2003)

Acknowledgements

It is my great pleasure to thank the many people that have supported me during my thesis work at Caltech and beyond.

Most of all, thanks is due to my advisor Harry Atwater, whose belief in the success of this project never faltered during the last three years. I cannot recall a single day when he was not willing to discuss obstacles and progress associated with my research, and his constant support and encouragements have been exemplary.

Mark Brongersma deserves most credits for allowing a smooth transition from course work into active research. During his postdoctoral work in our group, he started out the initial investigations into the properties of ordered metal nanoparticle chains, and was of great help in the planning of the first experiments. Most of the knowledge and skills I acquired during this project I owe to him. The void he left after his far-too-early disappearance to Stanford was filled by Pieter Kik, who has supported my research ever since. Pieter's often intuitive insight into physical processes and his strong background in optical experiments were of great help with this thesis.

I also had the great pleasure to work with a number of enthusiastic collaborators outside of Caltech. Thanks to Sheffer Meltzer of the University of Southern California for his willingness to contribute to this project with his invaluable experience as a surface chemist. He assembled a great number of nanoparticle structures using his dedicated atomic force micromanipulation system. During the last months of this work, Elad Harel of the University of California in San Diego continued in Sheffer's footsteps.

For me, it was always a daunting task to conduct experiments whose success or failure depend on the ordered arrangement of nanoscale structures and thus heavily on the

quality of the samples. But as it turned out there was no reason for worry since I was working with the very best - Richard Muller, Paul Maker and Pierre Echternach of the Jet Propulsion Laboratory in Pasadena. Thanks to them for their invaluable help with electron beam lithography.

The experimental part of this work has benefited a lot from discussions about near-field optical microscopy with Aaron Lewis of Nanonics Imaging Ltd. in Jerusalem. I am very grateful for his aid in setting up a reliable and intricate near-field microscopy station.

Funding for this work was mainly provided by the National Science Foundation through the Center of the Science and Engineering of Materials at Caltech and the Air Force Office of Scientific Research.

During my stay in Harry's group I was lucky to be surrounded by a number of great fellow students. I especially want to thank Luke Sweatlock for a lot of good and fun discussions and Robb Walters for providing a great office atmosphere.

I would never have had the pleasure of meeting all these fine people had it not been for two advisors that especially influenced me during my studies at Technische Universität München. Thanks to Fred Koch and Dmitri Kovalev for their training and encouragement, and for the great times in the beer gardens.

And of course, nothing would have been and is possible without Mag.

Abstract

The miniaturization of optical devices to spatial dimensions akin to their electronic device counterparts requires structures that guide electromagnetic energy with a lateral confinement below the diffraction limit of light. This cannot be achieved using conventional optical waveguides or photonic crystal defect waveguides. Thus, a size mismatch between electronic and optical integrated devices exists and needs to be overcome.

In this thesis, the possibility of employing plasmon-polariton excitations in "plasmon waveguides" consisting of closely spaced metal nanoclusters with a subwavelength cross section for the confinement and guiding of electromagnetic energy is examined both theoretically and experimentally. The feasibility of energy transport with mode sizes below the diffraction limit of visible light over distances of several hundred nanometers is demonstrated.

As a macroscopic analogue to nanoscale plasmon waveguides, the transport of electromagnetic energy in the microwave regime of the electromagnetic spectrum along structures consisting of closely spaced centimeter-scale metal rods is investigated. The dispersion relation for the propagation of electromagnetic waves is determined using full-field electrodynamic simulations, showing that information transport occurs at a group velocity of $0.65c$ for fabricated structures consisting of centimeter-scale copper rods excited at 8 GHz ($\lambda = 3.7$ cm). The electromagnetic energy is highly confined to the arrays, and the propagation loss in a straight array is about 6 dB/16 cm. Routing of energy around 90-degree corners is possible with a power loss of 3-4 dB, and tee structures for the splitting of the energy flow and for the fabrication of an all-optical

modulator are investigated. Analogies to plasmon waveguides consisting of arrays of nanometer-size metal clusters are discussed.

The possibility of guiding electromagnetic energy at visible frequencies with mode sizes below the diffraction limit is analyzed using an analytical point-dipole model for energy transfer in ordered one-dimensional arrays of closely spaced metal nanoparticles. It is shown that such arrays can work as plasmon waveguides that guide electromagnetic energy on the nanoscale. Energy transport in these arrays occurs via near-field coupling between metal nanoparticles, which sets up plasmon modes. This coupling leads to coherent propagation of energy with group velocities exceeding the saturation velocity of electrons in semiconductor devices. The point-dipole model suggests the feasibility of complex guiding geometries such as 90-degree corners and tee structures for the routing of electromagnetic energy akin to the fabricated macroscopic guiding structures, and the possibility of an all-optical modulator operating below the diffraction limit is suggested.

The interparticle coupling in plasmon waveguides is examined using finite-difference time-domain (FDTD) simulations. Local excitations of plasmon waveguides show direct evidence for optical pulse propagation below the diffraction limit of light with group velocities up to $0.06c$ in plasmon waveguides consisting of arrays of spherical noble metal nanoparticles in air. The calculated dispersion relation and group velocities correlate well with predications from the simple point-dipole model. A change in particle shape to spheroidal particles shows up to a threefold increase in group velocity for structures that can be fabricated using electron beam lithography. Pulses with transverse polarization are shown to propagate with negative phase velocities antiparallel to the energy flow.

Plasmon waveguides consisting of spherical and spheroidal gold and silver nanoparticles were fabricated using electron beam lithography with lift-off on ITO coated quartz slides. Far-field polarization spectroscopy reveals the existence of longitudinal and transverse collective plasmon-polariton modes. Measurements of the polarization dependent extinction confirm that the collective modes arise from near-field optical interactions. The key parameters that govern the energy transport are determined for various interparticle spacings and particle chain lengths using measurements of the resonance frequencies of the collective plasmon modes. For spherical Au nanoparticles with a diameter of 50 nm and an interparticle spacing of 75 nm, the energy attenuation of the plasmon waveguide is 6 dB/30 nm. This loss can be reduced and the energy attenuation length conversely increased by approximately one order of magnitude by using spheroidal silver nanoparticles as building blocks of plasmon waveguides, which show an enhanced interparticle coupling and a decreased plasmon damping.

Near-field optical microscopy allows for the local optical analysis and excitation of plasmon waveguides. Using the tip of a near-field optical microscope as a local excitation source and fluorescent polystyrene nanospheres as detectors, experimental evidence for energy transport over a distance of about 0.5 μm is presented for plasmon waveguides consisting of silver rods with a 3:1 aspect ratio and a center-to-center spacing of 80 nm. Ways to further improve the efficiency of energy guiding in plasmon waveguides and possible applications are discussed.

Table of Contents

Table of Figures

Chapter 1 Introduction

1.1 Towards nanoscale optical devices

The miniaturization of optical devices to size dimensions akin to their electronic counterparts is a major goal of current research efforts in optoelectronics, photonics and semiconductor manufacturing. A high integration of optical components allowing the fabrication of all-optical chips for computing and sensing requires both a confinement of the guided optical modes to small dimensions and the ability to route energy around sharp corners. Current technologies that are driving a revolution in the fabrication of integrated optical components are planar waveguides, optical fibers and photonic crystals, which can confine and guide electromagnetic energy in spatial dimensions in the micron and sub-micron regime (Figure 1-1).

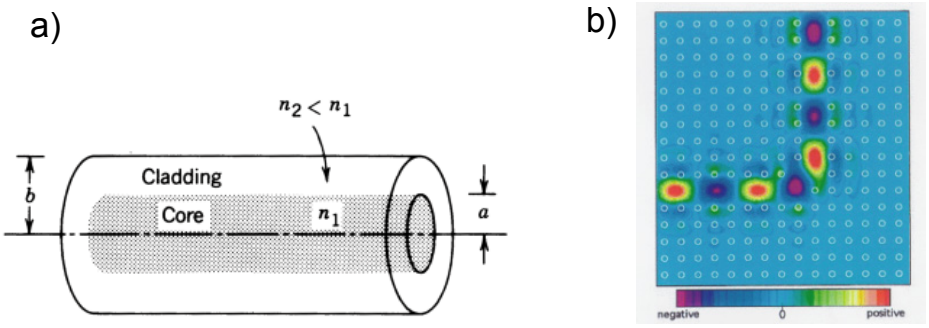

Figure 1-1 (color): Optical fibers and photonic crystals. a) Sketch of an optical fiber that confines and guides light by total internal reflection (after [1]). b) Finite-difference time-domain simulation of a guided light mode in a 90-degree corner photonic crystal defect waveguide (after [2]).

Whereas waveguides based on the principle of total internal reflection such as optical fibers do not allow for the guiding of light around sharp corners with a bending radius considerably smaller than the wavelength of light λ [1], bend engineering of defect modes in photonic crystals has enabled the fabrication of defect waveguides with complex guiding geometries [2, 3]. The further integration of active devices such as defect mode lasers into photonic crystals [4] will ensure a prominent spot for this technology in the creation of optical chips.

The size and density of optical devices employing these technologies is nonetheless restricted by the diffraction limit $\lambda/2n$ of light, which imposes a lower size limit of a few hundred nanometers on the optical mode size. Thus, a size mismatch between highly integrated electronic devices with lateral dimensions of a few tens of nanometers and optical guiding components persists and needs to be overcome.

1.2 Surface plasmons as a way to overcome the diffraction limit

The diffraction limit for the guiding of electromagnetic energy can be overcome if the optical mode is converted into a non-radiating mode that can be confined to lateral dimensions smaller than the diffraction limit. Prominent examples that have been the focus of intense research over the last couple of decades are surface plasmon-polaritons in metals. Plasmons are coherent oscillations of the conduction electrons of the metal against the static positive background of the metal ion cores. Whereas plasmons in bulk metal do not couple to light fields, a two-dimensional metal surface can sustain plasmons if excited by light either via evanescent prism coupling or the help of surface corrugations to ensure momentum matching [5]. Such surface plasmons propagate as coherent electron

oscillations parallel to the metal surface and decay evanescently perpendicular to it. Thus, the electromagnetic energy is confined to dimensions below the diffraction limit perpendicular to the metal surface. Corrugations can further act as light-scattering centers for surface plasmons, allowing for the fabrication of interesting optical devices such as an all-optical transistor [6].

A further confinement of energy-guiding surface plasmon modes can be achieved using metal nanowires instead of extended surfaces. In nanowires, the confinement of the electrons in two dimensions leads to well-defined dipole surface plasmon resonances if the lateral dimensions of the wire are much smaller than the wavelength of the exiting light. Thus, the optical properties of metal nanowires can be optimized for particular wavelengths of interest, and non-regular cross sections and coupling between closely spaced nanowires allow a further tuning of the optical response [7, 8]. Indeed, the propagation of electromagnetic energy has been demonstrated along noble metal stripes with widths of a few microns [9] and along nanowires with subwavelength cross sections [10, 11], and propagation lengths of a few microns have been found. Related to this principle is the interesting idea of one-dimensional negative dielectric core waveguides, where metals instead of dielectric materials are used as the core in a waveguide with a cross section below the diffraction limit [12].

Another intriguing nanoscale system that can sustain surface plasmons are metal nanoparticles, and their interaction with light has been the focus of intense research in recent years [13, 14]. In metal nanoparticles, the three-dimensional confinement of the electrons leads to well-defined surface plasmon resonances at specific frequencies. From work on single noble metal nanoparticles, it is well established that light at the surface

plasmon resonance frequencies interacts strongly with metal particles and excites a collective motion of the conduction electrons, or plasmon [15]. These resonance frequencies are typically in the visible or infrared part of the spectrum for gold and silver nanoparticles embedded in a variety of hosts. For particles with a diameter much smaller than the wavelength λ of the exciting light, plasmon excitations produce an oscillating electric dipole field resulting in a resonantly enhanced non-propagating electromagnetic near-field close to the particle surface.

Recently, it has been suggested that near-field interactions between closely spaced metal nanoparticles in regular one-dimensional particle arrays can lead to the coherent propagation of electromagnetic energy along the arrays with lateral mode sizes below the diffraction limit [16]. For Au and Ag nanoparticles in air, energy decay lengths of a couple of hundred nanometers have been predicted. Furthermore, it was suggested that these so-called plasmon waveguides can guide electromagnetic energy around sharp corners and tee structures, and an all-optical modulator based on interference operating below the diffraction limit was proposed [17].

The use of ordered arrays of metal nanoparticles as plasmon waveguides is intriguing from both a technology oriented and a fundamental point of view. Metal nanoparticles can be fabricated using a wide arsenal of tools including electron beam lithography [18], ion beam implantation [19], colloidal synthesis [20], and self-assembly [21]. This way, metal nanoparticles of different shapes can be produced from a variety of materials, and the synthesis of core-shell composite particles offers the incorporation of novel non-linear materials for additional functionality. The fabrication of plasmon waveguides

consisting of such particles could enable the design of highly integrated optical devices and logic elements operating below the diffraction limit (Figure 1-2).

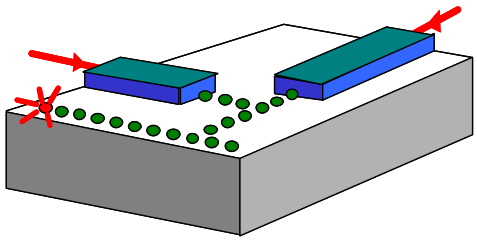

Figure 1-2 (color): Sketch of a plasmon waveguide network coupling two conventional dielectric plane waveguides.

From a fundamental point of view, a study of plasmon waveguides provides insight into the nature of optical near-fields and electromagnetic light-matter interactions on the nanoscale. The strong dipolar coupling between metal nanoparticles can also serve as a model system for the study of other dipole-coupled energy transfer structures such as quantum dot chains [22], magnetic nanoparticle arrays [23], and coupled-resonator optical waveguides [24].

1.3 Road map through this thesis

In the following chapters, the physical properties of plasmon waveguides consisting of ordered, closely spaced metal structures with subwavelength dimensions are analyzed both theoretically and experimentally.

Chapter 2 presents experiments and full-field electrodynamic simulations on macroscopic analogues to nanoscale plasmon waveguides [25-27]. The macroscopic waveguides are based on centimeter-scale metal rods with a center-to-center spacing of a

few millimeters and operate in the microwave and RF regime of the electromagnetic spectrum, akin to Yagi arrays used for the steering of RF beams. These so-called Yagi waveguides can be excited using a dipole antenna and show a strong confinement of the electromagnetic energy to the guiding structure. Linear arrays, 90-degree corner and tee waveguides are characterized, and simulation results on an all-optical modulator are presented.

The discussion of the properties of nanoscale metal nanoparticle plasmon waveguides begins in Chapter 3 with the description of a point-dipole model of energy transfer in plasmon waveguides consisting of spherical metal nanoparticles [17, 28]. The dispersion relation and group velocity for energy transport are determined, and transmission coefficients for network structures consisting of corners and tees are presented, as well as the modulation characteristic of an all-optical switch in the point-dipole limit. The important notion of plasmon damping is addressed and discussed rather extensively, to offset some contradicting and confusing descriptions of the damping processes found in the literature [29]. An experimentally accessible expression for the expected energy attenuation of plasmon waveguides is derived.

Chapter 4 extends the analytical modeling of plasmon waveguides in Chapter 3 by solving the full set of Maxwell's equations using finite-difference time-domain simulations for extended metal nanoparticles modeled via a Drude model [30, 31]. Starting from a determination of the plasmon resonance frequencies of single noble metal nanoparticles, interactions between nanoparticles located in each other's near-field are analyzed using plane-wave excitations. This way, a realistic interparticle coupling strength can be determined. Local excitation sources allow for direct determination of the

dispersion relation and characterization of optical pulse propagation in plasmon waveguides. The optimization of the guiding properties of plasmon waveguides using non-spherical particles is discussed.

The fabrication and far-field optical characterization of plasmon waveguides are presented in Chapter 5. Plasmon waveguides consisting of spherical and rod-shaped Au and Ag nanoparticles fabricated using electron beam lithography are analyzed using far-field polarization spectroscopy [28, 32, 33]. Extinction measurements allow for the determination of the interparticle coupling strength and bandwidth of energy transport, thus yielding estimates for the group velocities and energy decay lengths of the fabricated plasmon waveguides.

Chapter 6 presents a characterization of the guiding properties of plasmon waveguides using a near-field optical microscope (NSOM) [34-36]. The tip of an illumination-mode NSOM is used as a local excitation source, and fluorescent polystyrene nanospheres are used as local detectors of energy transport. Evidence for energy transport over distances of about 0.5 μm is presented for plasmon waveguides consisting of rod-shaped Ag nanoparticles. Chapter 7 summarizes the work presented in this thesis and gives an outlook on future work and applications of plasmon waveguides.

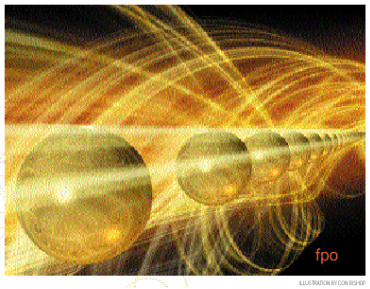

Figure 1-3 (color): Artist's rendition of a plasmon waveguide [37].

Chapter 2 Yagi waveguides

2.1 Introduction

As a large-scale analogue to nanoscale plasmon waveguides that operate in the visible part of the electromagnetic spectrum, this chapter discusses the propagation of electromagnetic energy along centimeter-scale periodic metal structures in the radio frequency regime, similar to linear Yagi antenna arrays. Figure 2-1 shows a sketch of a 7-element Yagi antenna array as it is typically used in radio frequency communications. The antenna is driven by a dipole whose beam-profile is modified by the addition of director and reflector rods to assure a directed emission and receiving of radiation [38].

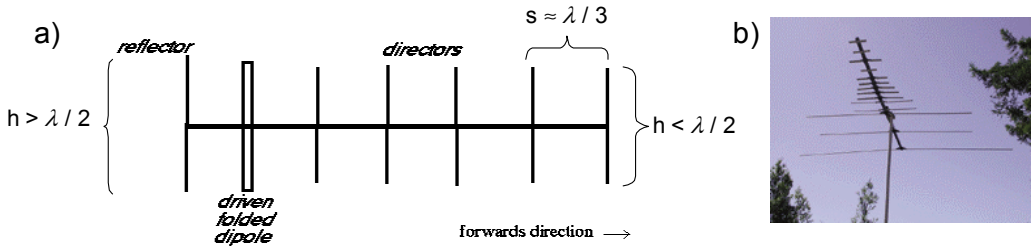

Figure 2-1 (color): Yagi antennas. a) Sketch of a linear Yagi antenna used in radio frequency communication. The beam profile is shaped by the director and reflector rods. b) Picture of a TV Yagi antenna.

A typical Yagi array (Figure 2-1 a) consists of a driven dipole source and a series of equally spaced metal rods with a height h and an inter-rod spacing s. It is well known experimentally [39] and theoretically [40, 41] that such arrays show guiding properties for electromagnetic radiation as long as $h/\lambda_F < 0.5$, where λ_F is the free-space wavelength of the electromagnetic wave emitted by the source [38-41]. Under this

condition, the phase velocity of the guided wave is less than the free-space velocity *c*. Conversely, for rods with $h/\lambda_F > 0.5$, the phase velocity is greater than *c* and the waves are reflected in the backwards direction. Conventional Yagi antenna arrays are aimed at radiating out electromagnetic energy into the far-field and have inter-rod spacings on the order of $\lambda_F/3$. Here we will describe structures with a significantly smaller spacing of $\lambda_F/20$, which allow for more efficient guiding of energy around sharp corners. Smaller spacing between adjacent rods results in a slower phase velocity [40, 41] and a stronger confinement of the electromagnetic waves to the structure due to increased near-field coupling. The following sections will describe electromagnetic simulations and experiments that examine energy propagation in straight arrays, 90-degree corners and tee structures, and an all-optical modulator based on interference will be discussed. The last part of this chapter will establish the link to nanoscale plasmon waveguides.

2.2 The dispersion of a Yagi waveguide

In order to determine the range of suitable heights and spacings for efficient Yagi waveguides, full-field electrodynamic simulations of the 10-element Yagi array depicted in Figure 2-2 were performed using an antenna simulation software (EZNEC v. 2.0). In the simulation, the axes of the rods were chosen to be in the z-direction and the center of the first rod (source) was located at $(x,y,z) = (0,0,0)$.

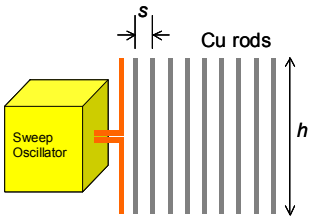

Figure 2-2 (color): Geometry of a short 10-element Yagi array for the determination of the dispersion relation using full-field electrodynamic simulations.

The first rod was driven by a center-fed current source at 8.0 GHz (λ_F =3.75 cm), and the steady state electromagnetic field distribution around the structure was determined. The heights h of the rods and the inter-rod spacings s were varied to explore their effect on the guiding and dispersion of electromagnetic waves.

Figure 2-3 shows typical distributions of the absolute value of the z-component of the electric field vector $|E_z|$ in the x-y plane for a linear Yagi array consisting of 10 copper rods with an inter-rod spacing $s = 0.05\lambda_F$ (2 mm) for various rod heights h.

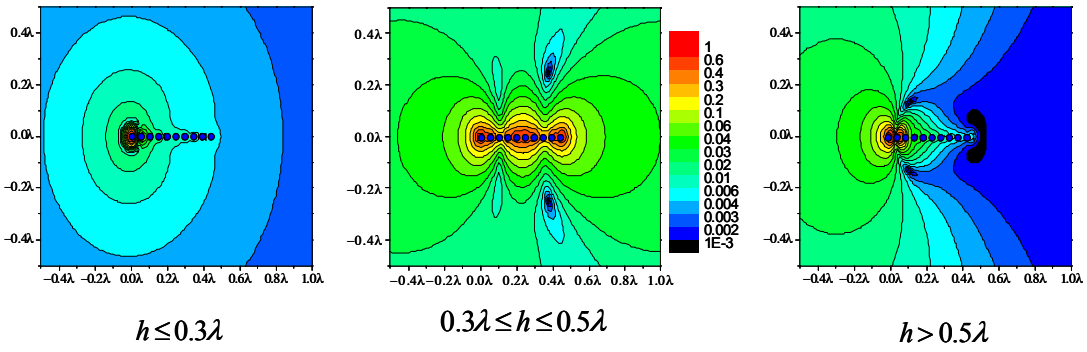

Figure 2-3 (color): Influence of rod height on the guiding properties of Yagi arrays. The contour plots show the distribution of the absolute value of the z-component of the electric field vector $|E_z|$ in the x-y plane for linear arrays of 10 rods with an inter-rod spacing of 0.05λ and variable heights h. The first rod is driven with a dipole current source at 8 GHz (λ = 3.75 cm). The color scale is exponential in the magnitude of $|E_z|$ and spans about 3 orders of magnitude.

For rods small compared to the free-space wavelength ($h \lesssim 0.3\lambda_F$), the absorption and scattering cross sections of the rods are too small to allow for efficient guiding of electromagnetic energy along the array. For medium-sized rods ($0.3\lambda_F \lesssim h < 0.5\lambda_F$), the cross sections are large enough to allow for efficient guiding of the electromagnetic energy, and the field distribution along the array shows a standing-wave type behavior due to reflection of the guided wave at the end of the structure. We will call this rod size regime the transmission window of Yagi arrays for energy guiding. For larger rods ($h > 0.5\lambda_F$), the electromagnetic waves radiated by the source dipole interfere destructively in the forward direction, causing an exponential decay of the electric field along the rod structure and a concurrent back reflection. Thus, electromagnetic energy can be guided along a Yagi array only in the transmission window for rods with $0.3\lambda_F \lesssim h < 0.5\lambda_F$.

The change in the guiding properties of Yagi arrays at a rod height $h = 0.5\lambda_F$ is due to a change in the antenna impedance of a single rod at $0.5\lambda_F$ and can be understood using a loaded transmission line analysis [40, 42] depicted in Figure 2-4.

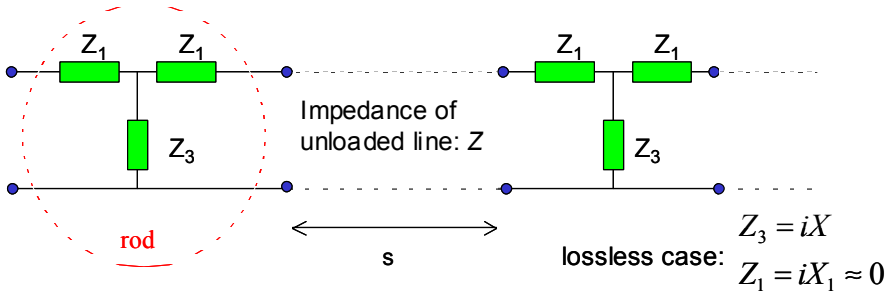

Figure 2-4 (color): Transmission line model of a Yagi array (after [40]).

The transmission line model approximates each rod as a load on an otherwise unloaded transmission line of impedance Z [40]. Analysis of the loaded line's impedance allows for the determination of the phase velocity of electromagnetic waves on the transmission line. Assuming negligible losses inside the rods with an inter-rod spacing s, the phase velocity v can be calculated from the shunt impedance iX and the impedance of the unloaded line Z to

$$\frac{v}{c} = 1 + \frac{Z\lambda_0}{4\pi s X},$$

where c and λ_0 are the free-space velocity and wavelength of the guided electromagnetic radiation. In order to allow for a guiding of electromagnetic radiation, the phase velocity must be smaller than the free-space velocity of light. This requires rods with capacitive antenna impedance $X < 0$. It is well known from antenna theory that this is the case for rods with a height $h < \lambda_F / 2$. For larger rods, the antenna impedance becomes inductive, resulting in a phase velocity greater than the free-space velocity of light and no guiding. From the view point of optical theory, a phase velocity $v < c$ implies a mean refractive index of the Yagi array greater than one, leading to convergence of the source dipole radiation along the structure analogous to a convex lens. The transmission line analysis also suggests that for capacitive rods the phase velocity decreases with decreasing inter-rod spacing s, leading to a stronger confinement of the electromagnetic energy along the array. This was confirmed using full-field electromagnetic simulations of Yagi arrays with various inter-rod spacings.

The dependence of the phase velocity of electromagnetic waves propagating on a linear Yagi array on the rod geometry can be summarized by computing the dispersion

relation $\nu(\mathbf{k})$ of the guided waves. Figure 2-5 shows this dispersion relation for a linear Yagi array consisting of 101 copper rods as obtained by full-field electrodynamic simulations.

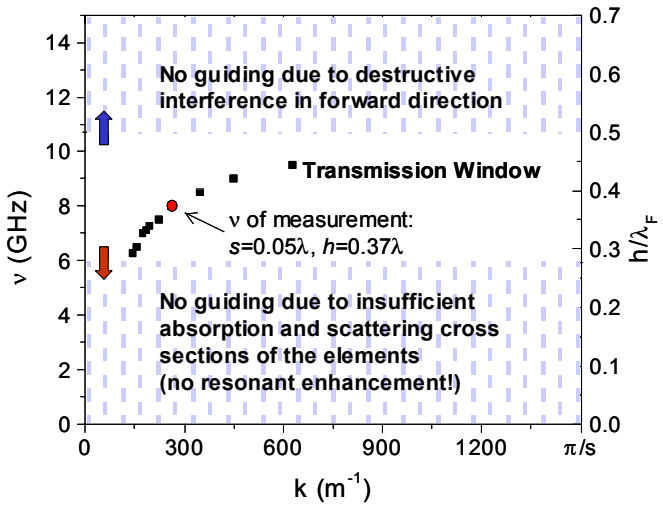

Figure 2-5: Dispersion relation for electromagnetic waves propagating on a linear Yagi array consisting of 101 copper rods obtained by electromagnetic simulations. The rods have a diameter d of 1 mm, a height h of 1.4 cm, and were spaced by s = 2 mm apart.

The rods have a diameter d = 1 mm, height h = 1.4 cm and are spaced s = 2mm apart, corresponding to the dimensions of the fabricated Yagi arrays described in section 2.3. The first rod was driven at various frequencies from 6.0 to 9.5 GHz via a current source, and the standing wave pattern along the structure was analyzed to determine the corresponding wave vector **k** of the guided waves along the structure. The decrease in slope with increasing wave vector **k** indicates a decrease of the group velocity of the electromagnetic waves. Near the zone boundary at $\mathbf{k} = \pi/s$ the ratio h/λ_F approaches

0.5, as predicted by linear antenna theory [40, 41]. At the excitation frequency of 8.0 GHz used in experiments on fabricated arrays the phase velocity is about 0.65c.

2.3 Guiding along linear and corner Yagi arrays: Experiments and simulations

This section describes three fabricated Yagi waveguide structures consisting of arrays of Cu rods, namely, a straight line, a 90-degree corner, and a tee structure. The rods have a diameter of 1 mm ($d = 0.002\lambda_F$), a height of 1.4 cm ($h = 0.37\lambda_F$), and were spaced 2 mm apart ($s = 0.05\lambda_F$). The rods were fixed in position using a Styrofoam construction that showed negligible guiding properties as depicted in Figure 2-6. The first rod was a center-fed dipole driven at 8.0 GHz using a HP 8620C sweep oscillator. The distribution of the electromagnetic field along the array was studied by local power measurements using a 1 cm long probe dipole and a HP 8472 crystal detector connected to a HP 415E standing wave meter. These measurements were performed at a distance of $0.15\lambda_F$ from the array to avoid significant interference with the propagating electromagnetic waves. None of the structures was terminated with impedance matching loads to obtain standing wave patterns for physical analysis. The results were compared to full-field electrodynamic simulations of the fabricated structures as discussed in Section 2.2.

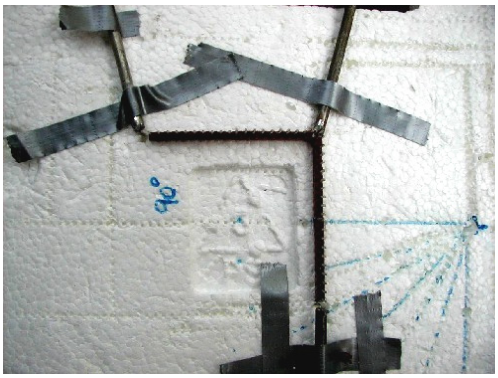

Figure 2-6 (color): Top view of a fabricated 90-degree corner Yagi structure on Styrofoam, showing a source and two probe dipoles (courtesy of Luke Sweatlock).

Figure 2-7 shows the distribution of the absolute value of the z-component of the electric field vector $|E_z|$ in the x-y plane for a linear array of 101 rods. The color scale is exponential in the magnitude of $|E_z|$ and spans three orders of magnitude. The inset shows both the measured (squares) and simulated (thin solid line) power at a distance of $0.15\lambda_F$ from the array, normalized to the power obtained at the position of the source.

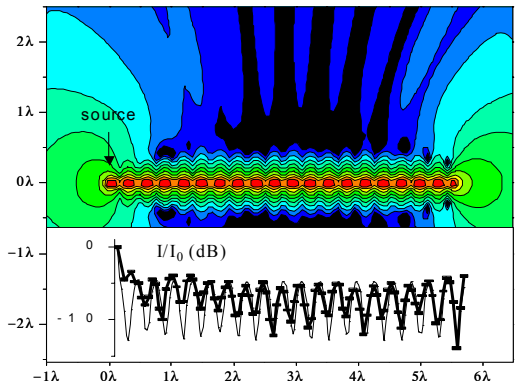

Figure 2-7 (color): Guiding energy along a linear Yagi array. The plot shows the distribution of the absolute value of the z-component of the electric field vector $|E_z|$ in the x-y plane for a linear array of 101 rods. The rods are 1 mm in diameter, 1.4 cm long, and spaced 2 mm apart. The color scale is exponential in the magnitude of $|E_z|$ and spans about 3 orders of magnitude. The inset shows both the measured (squares) and simulated (thin solid line) power at a distance of 0.15λ from the array.

Most of the energy emitted by the source is lost due to radiation into the far-field, as seen in the field plot and in the inset as an initial drop in the measured power after rod number 1. Along the array a standing wave pattern is recognized, indicating weak attenuation and strong reflection at the endpoints. The period of the standing wave obtained by simulation and experiment are in excellent agreement. The discrepancies in the measured and simulated powers can be attributed in part to the finite diameter of the probe dipole, which causes an averaging-out of the sharp features seen in the simulation. About 90% of the energy is confined within a distance of $0.05\lambda_F$ from the array, demonstrating strong guiding of the electromagnetic wave. The propagation loss α of the electromagnetic wave and its reflection coefficient R can be estimated by assuming that the standing wave pattern results form electromagnetic waves that travel back and forth along the array. From such an analysis $\alpha \approx 6$ dB/16 cm corresponding to 6dB/$4\lambda_F$ and $R \approx 75\%$ are determined. The remaining 25% of the power is radiated into the far-field at the end of the array, as can be seen in the field plot. It is important to note that radiation loss only occurs at the two ends of the linear array. More generally, radiation loss occurs at each discontinuity in the structure where the guided electromagnetic wave changes direction. For the design of more complex array structures it is important to quantify the losses at such discontinuities. For this purpose, the transport around 90-degree corners is investigated next.

Figure 2-8 shows the distribution of $|E_z|$ in the x-y plane for a corner structure consisting of two linear arrays of rods that meet at a 90-degree angle. The inset shows both the measured and simulated power at a distance of $0.15\lambda_F$ on the outside of the corner, normalized to the power obtained at the position of the source.

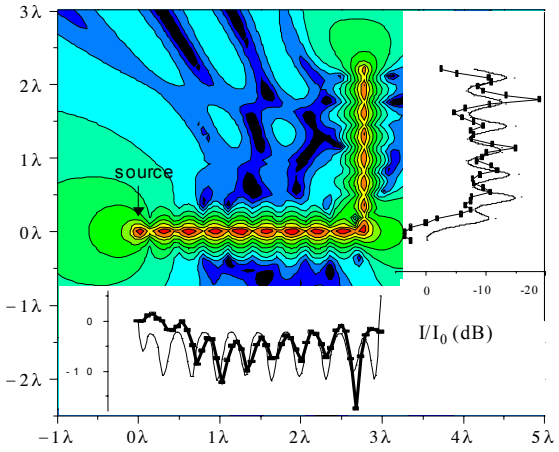

Figure 2-8 (color): Guiding energy along a corner Yagi array. The plot shows the distribution of $|E_z|$ in the x-y plane for a corner structure consisting of two linear arrays of rods that make a 90-degree angle. The rods are 1 mm in diameter, 1.4 cm long, and spaced 2 mm apart. The color scale is exponential in the magnitude of $|E_z|$ and spans about 3 orders of magnitude. The inset shows both the measured (squares) and simulated (thin solid line) power at a distance of 0.15λ from the array.

As for the straight line, simulation and experiment are in reasonable agreement. As expected, power is lost in turning the corner due to radiation into the far field. The ratio of the power in the side arm to the power in the main arm is 3-4dB. This decrease in power is due to radiation and back reflection at the corner. Similar results were found for a tee structure (Figure 2-9) in which an electromagnetic wave was injected into the stem and the power flow split into the two side arms. The ratio of the power in one side arm to the power in the stem was about 8dB. This is roughly twice the power lost in the corner structure.

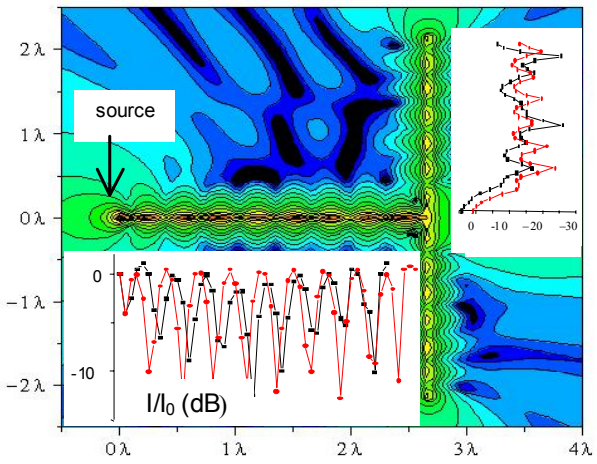

Figure 2-9 (color): Routing energy in a Yagi tee structure. The plot shows the distribution of $|E_z|$ in the x-y plane for a tee structure. The rods are 1 mm in diameter, 1.4 cm long, and spaced 2 mm apart. The color scale is exponential in the magnitude of $|E_z|$ and spans about 3 orders of magnitude. The inset shows both the measured (black squares) and simulated (red circles) power at a distance of 0.15λ from the array.

The transmission of electromagnetic energy around corners and tee structures can be optimized by the placement of additional reflector rods with a height $h > \lambda_F/2$ that frustrate radiation into the far field. A full-field electromagnetic simulation of a tee structure showed a 10% increase in the transmitted power in both arms if five reflector rods were placed as an extension to the stem after the intersection of stem and sidearms. More careful design of Yagi structures should thus allow for improved transmission coefficients for electromagnetic energy around corner and tee discontinuities, allowing for the construction of complex networks.

Apart from 90-degree corners and tee structures, another discontinuity that is worth mentioning is the breaking of the perfect periodicity in the array. It was found that the confinement of the electromagnetic energy around these arrays is not significantly altered when rods are displaced from their original positions by as much as 50% of the inter-rod

spacing. Simulations show that straight arrays with random displacements of a subset of the rods still demonstrate a comparable guiding and attenuation. If near-field coupling would be dominant, the transport would be extremely sensitive to a breaking of the perfect translation symmetry, because the strength of near-field coupling is strongly dependent on the spacing $\left(\propto d^{-3}\right)$. This strong distance dependence is well known from Förster resonance energy transfer [43]. It is thus concluded that for Yagi waveguides the intermediate-field and far-field terms play an important role in the transport. For this reason, fabrication-induced deviations from perfect translation symmetry in the array structures can be tolerated.

2.4 Towards active devices: A three-terminal modulator

The fabrication off all-optical modulators, switches and transistors is a major goal of current photonic research [6]. It is intriguing to investigate the possibility of using Yagi array waveguides as interferometers that can serve as the building blocks of an all-optical modulator. A three-terminal device can be realized out of a tee structure if one source is placed in the stem and one in the sidearm (asymmetric configuration) or if one source is placed into each sidearm (symmetric configuration). Figure 2-10 shows full-field electrodynamic simulations of the electric field around an asymmetric modulator structure.

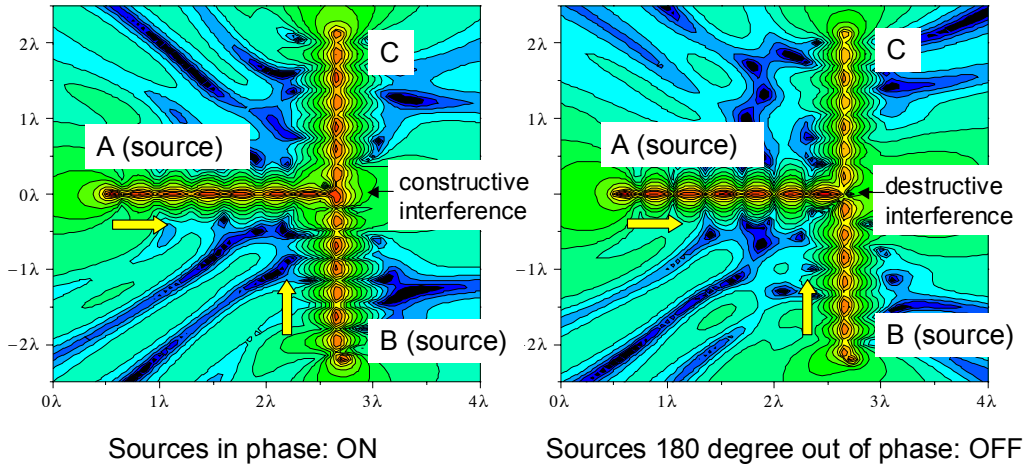

Figure 2-10 (color): Modulation of energy in Yagi arrays. The plots show the distribution of $|E_z|$ in the x-y plane for a three-terminal modulator structure. The color scale is exponential in the magnitude of $|E_z|$ and spans about 3 orders of magnitude. For sources in phase (left), the waves launched by the two sources interfere constructively at the junction. For sources out of phase (right), the waves interfere destructively.

The modulator operates by interference of the waves launched by the two sources, A and B. A constructive interference of the waves at the junction (ON state) leads to a 50% increase in transmission into side arm C compared to waves interfering destructively at the junction (OFF state). The reason that the switching efficiency is less than 100% is due to the fact that the energy propagation is not solely due to coupling between nearest neighbors. Even in the case where the waves interfere destructively at the junction rod, there is still energy leaking into arm C due to coupling between rods which are further apart. Such cross talk effects are strongly reduced in modulators with a symmetric source arrangement.

Figure 2-11 shows the modulation characteristic of a three-terminal Yagi modulator for both a non-symmetric (blue) and symmetric (red) source arrangement obtained using

full-field electromagnetic simulations. The sources are 180 degree out of phase and emit electromagnetic waves at 8.0 GHz, resulting in destructive interference at the junction. This way, a variation in modulation power M causes a change in the transmitted signal power T.

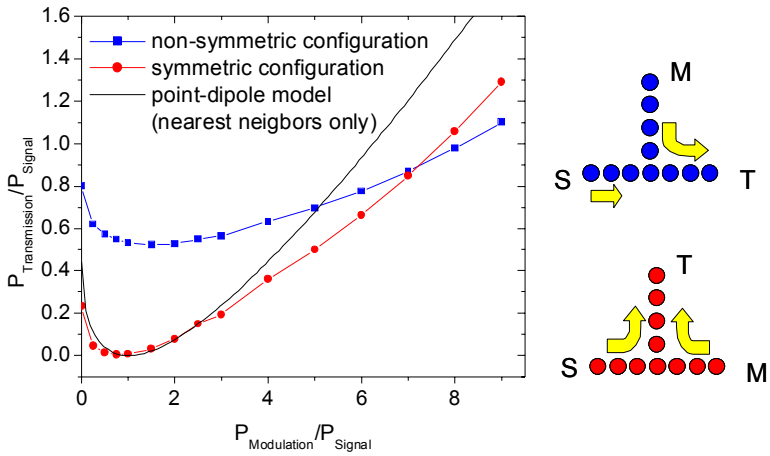

Figure 2-11 (color): Power modulation characteristic of a three-terminal Yagi modulator consisting of a tee structure and a signal source S and a modulation source M. Both sources emit electromagnetic radiation at 8 GHz and are 180 degree out of phase, leading to destructive interference at the tee intersection. A variation of the modulation power results in a modulation of the transmitted signal T. Shown are results for a non-symmetric (blue) and a symmetric (red) source arrangement obtained by simulations, and results of an analytical point-dipole model calculation (akin to [17]).

Whereas a non-symmetric configuration does not allow for a complete nulling of the transmission as discussed above, the symmetric case produces a perfect null if both sources emit electromagnetic waves at the same power. This can be directly established using the symmetry of the arrangement. Figure 2-11 also shows the results of point-dipole model calculations taking only interactions between nearest neighbors into account (akin to [17]). For small modulation powers, the simulation results for the symmetric case and the point-dipole calculations are in reasonable agreement.

Yagi tee structures thus show promise for applications as interferometer-based modulators and switches if careful attention is paid to geometry requirements arising from far-field interactions between individual rods.

2.5 The link to nanoscale plasmon waveguides

At this point, it is worthwhile to note a few analogies and differences between centimeter-scale metal-rod Yagi arrays and plasmon waveguides, consisting of nanometer-sized noble metal clusters. For the excitation of electromagnetic waves in metal-rod Yagi arrays, a radio frequency dipole antenna was used. Arrays of metal nanoclusters can be efficiently excited near their surface plasmon resonance frequency [13]. For Au, Ag, and Cu clusters in air, this resonance occurs at optical frequencies and is associated with resonantly enhanced absorption and scattering cross sections. Due to the enhanced scattering cross section, a strong coupling between the metal particles can be obtained even for cluster sizes that are small compared to the interparticle spacing s. It was suggested that a strong guiding array can be realized using nanometer-size spherical clusters with a diameter D for which $D < s << \lambda_F$ [17]. This is a necessary requirement for near-field coupling between nearest neighbors to be the only contributor to the transport. Since this condition is met in plasmon waveguides, far-field radiation at discontinuities can be expected to be of a small magnitude. This situation cannot be obtained in the radio frequency regime where the absorption and scattering cross sections of the rods are not resonantly enhanced. For radio frequencies, strong guiding can only be obtained if the height of the rods is a substantial fraction of $\lambda_F/2$, and thus $h < s << \lambda_F$ cannot hold. The positive effect of an increase of the scattering cross section near the plasmon resonance

frequency of metal clusters is counteracted by a concomitant increase in the absorption due to resistive heating. This will limit the size of functional plasmonic devices to size dimensions of a few λ_F. It has been demonstrated theoretically that functionality can indeed be obtained at this length scale [17].

2.6 Conclusions and outlook

Experiments and simulations have shown that in the radio frequency regime electromagnetic waves can be guided along one-dimensional structures consisting of closely spaced metal rods akin to Yagi arrays. Significant losses due to radiation into the far field and reflections mainly occur when the waves change direction. Linear arrays, 90-degree corner and tee structures for the guiding and routing of electromagnetic energy have been demonstrated experimentally, and an all-optical modulator has been analyzed using full-field simulations.

For Yagi array-type waveguides to find an application niche in an area that is dominated by metal stripe waveguides, the demonstration of the feasibility of functional, active devices would be a next step. Simulations suggest that modulators and switches can be built by employing interference between waves launched from different sources. The incorporation of non-linear elements to produce the necessary phase-shifts between the interfering waves could be a promising route for the fabrication of functional all-optical radio frequency devices. Also, a characterization of the dispersion properties of Yagi arrays for the guiding of electromagnetic pulses is necessary. Functional Yagi array waveguide elements could be integrated into conventional Yagi antennas for the routing of incoming or to-be-emitted information.

On a last note, the incorporation of resonant circuits on the metal rods used in Yagi waveguide arrays would allow the establishment of a “plasmon resonance”-type behavior. This way, the scattering cross sections of the rods would be resonantly enhanced, allowing for rods significantly smaller than the wavelength of the electromagnetic radiation and a closer analogy of Yagi arrays to nanoscale plasmon waveguides.

Chapter 3 Going nanoscale: Point-dipole theory of plasmon waveguides

3.1 Plasmon resonances in small metal clusters

It is well established that single noble metal nanoparticles interact strongly with visible and near-infrared light when resonantly excited at their surface plasmon frequency [13]. The resonant behavior is due to the confinement of the conduction electrons inside the particle, which sets up an effective restoring force due to surface polarization upon a light-induced displacement of the conduction electrons. For small particles (diameter $D < 15$ nm for Ag and $D < 25$ nm for Au particles), retardation of the driving light field along the particle volume is negligible and all conduction electrons are excited in phase in a collective dipole-like oscillation. At the resonance, the polarizability of the nanoparticle is resonantly enhanced. Figure 3-1 shows the flow of electromagnetic energy around a single spherical metal nanoparticle at two different excitation frequencies. When the frequency of the light is far from the intrinsic plasmon resonance frequency of the metal nanoparticle (Figure 3-1 a), the energy flow is only slightly perturbed. At the plasmon resonance frequency, the strong polarization of the particle effectively draws energy into the particle (Figure 3-1 b). The resonance in the polarizability leads to an enhanced electromagnetic near field which is confined over distances $d < \lambda$ to the surface of the nanoparticle. For Au and Ag nanoparticles, the near-field enhancement is typically on the order of 10 and can only be detected in the near field of the particle or through the

enhancement of secondary processes such as an increased nanoparticle luminescence [44-46].

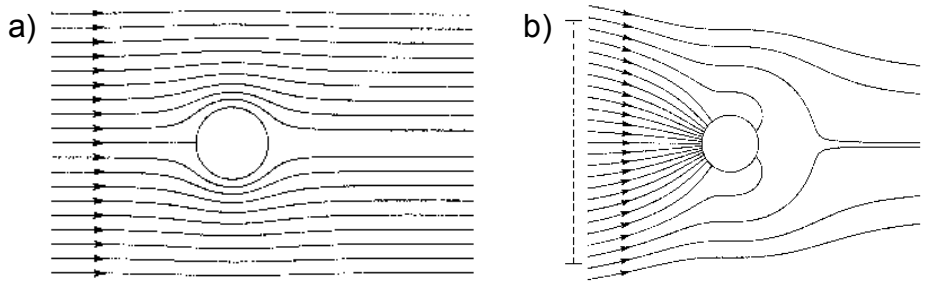

Figure 3-1: Energy flux (Poynting vector) around a metal nanoparticle under plane wave excitation at two frequencies. a) When the excitation occurs far from the plasmon resonance frequency, the energy flow is only slightly perturbed. b) When the excitation occurs at the plasmon frequency, the energy flow is directed towards the particle. The sketches show Poynting vector calculations for the absorption of electromagnetic energy [14].

In the far field, the resonance can be observed as a strong enhancement in the scattering and absorption cross sections in optical extinction measurements [13]. Quasi-static Mie-theory [47] allows for the calculation of the far-field extinction cross section σ_{ext} for a spherical nanoparticle of volume V_0 and dielectric function $\varepsilon(\omega)=\varepsilon_1(\omega)+i\varepsilon_2(\omega)$ embedded in a non-absorbing medium with dielectric constant ε_m:

$$\sigma_{ext}=9\frac{\omega}{c}\varepsilon_m^{\frac{3}{2}}V_0\frac{\varepsilon_2(\omega)}{[\varepsilon_1(\omega)+2\varepsilon_m]^2+\varepsilon_2(\omega)^2}.$$

For small damping $\left(\varepsilon_2(\omega),\frac{\partial\varepsilon_2}{\partial\omega}<<1\right)$, the resonance occurs when the Fröhlich condition

$$\varepsilon_1(\omega)=-2\varepsilon_m$$

is met.

In case of small damping, the resonance position is only dependent on the real part ε_1 of the metal dielectric function and can be shifted throughout the visible and near-infrared spectral range by embedding the particle in hosts with different dielectric constants ε_m [48]. For colloidal particles, the dipole plasmon resonance frequency can be easily probed via extinction measurements of large amounts of particles in solution. Figure 3-2 shows an absorption spectrum of 30 nm colloidal Au nanospheres immersed in water, showing a distinctive absorption peak at 2.3 eV, in agreement with Mie-theory calculations.

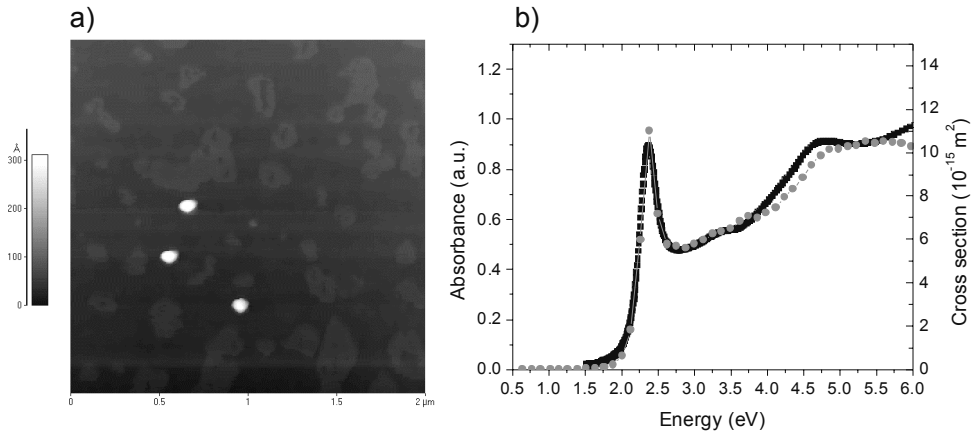

Figure 3-2: Extinction of 30 nm Au colloids. a) Atomic force microscopy image of 30 nm Au colloids deposited on a glass slide. b) Absorption spectrum of 30 nm Au colloids in water, obtained using a chemical spectrograph (black line) and Mie-theory calculations (gray circles) using the dielectric function for Au obtained by [49].

For non-spherical particles in the dipole limit ($D << \lambda$), the resonance condition is modified to account for the change in boundary conditions at the particle surface. For spheroids, this results in short-axis and long-axis dipole plasmon modes, which are shifted with respect to the plasmon dipole resonance frequency of a spherical particle

(Figure 3-3). Measurements of the far-field extinction of single noble metal nanoparticles have allowed for the determination of the plasmon resonance frequencies for a variety of particle shapes [50, 51]. It should be noted that only for free electron metals does the dipole resonance frequency ω_0 depend solely on the real part $\varepsilon_1(\omega)$ of the dielectric function and the surrounding medium ε_m, and the resonance width conversely only on $\varepsilon_2(\omega)$. For realistic metals both resonance position and width in general depend on ε_1 and ε_2.

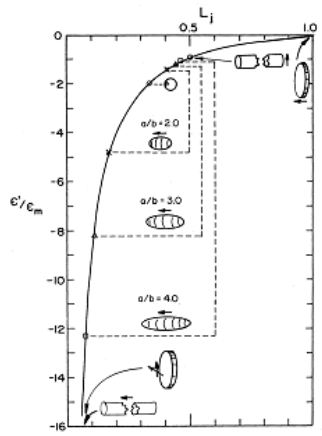

Figure 3-3: Dipole resonance position for spheroids with different aspect ratios for both the long- and the short-axis mode of excitation [14].

The finite width of the dipole plasmon resonance of a metal nanoparticle is caused by plasmon damping. The damping is due to the dephasing of the coherent conduction electron motion with time. Figure 3-4 shows a schematic of the different processes involved in the damping of a surface plasmon excited by a photon of energy $h\nu$.

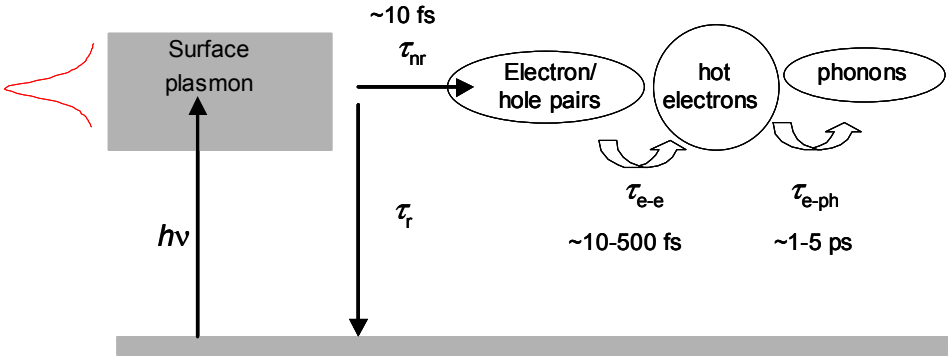

Figure 3-4: Energy relaxation of a surface plasmon. The relaxation takes place either via radiative or non-radiative processes. The non-radiative relaxation channel leads to the creation of electron-hole pairs and the subsequent relaxation into hot electrons and phonons.

The damping of the plasmon resonance is in general described via a total dephasing time T_2 and an energy relaxation time T_1 [52]. Both are related to the homogeneous linewidth Γ of the surface plasmon resonance via

$$\Gamma(\omega) = \frac{2}{T_2} = \frac{1}{T_1} + \frac{1}{T_2^*}$$

T_2^* is called the "pure dephasing time" which describes quasi-elastic electron scattering events that change the electron wave vector but not its energy. Its contribution to the total dephasing time T_2 is often combined with the energy relaxation time T_1, yielding $T_2 = 2T_1$. The damping of the plasmon resonance is thus determined by the energy relaxation time T_1, defined as

$$\frac{1}{T_1} = \frac{1}{\tau_{nr}} + \frac{1}{\tau_r}.$$

The energy relaxation of a plasmon oscillation is composed of a non-radiative decay channel with a time constant τ_{nr} and a radiative decay channel with a time constant τ_r. For metal nanoparticles with a diameter $D << \lambda$ the energy relaxation is mostly due to non-radiative processes ($\tau_r >> \tau_{nr}$) [52]. The oscillating electrons lose their energy via inelastic scattering to single electron excitations (Landau damping), so-called electron-hole states with a time constant τ_{nr} on the order of 10 fs. These transitions can be either intraband or interband, and increase with the spectral overlap of the plasmon resonance with the interband absorption edge. The electron-hole states subsequently relax via electron-electron and electron-phonon scattering on the 100 fs and 1 ps time scale.

The plasmon damping of noble metal nanoparticles with diameters 5 nm < D < 30 nm is mostly due to non-radiative processes and can thus be expressed via the materials parameters such as the optical conductivity or the dielectric function. Kreibig derived the following analytical approximation for the linewidth $\Gamma(\omega)$ based on the optical conductivity as the only damping mechanism [13]:

$$\Gamma(\omega) = \frac{2\varepsilon_2(\omega)}{\sqrt{\left(\frac{\partial \varepsilon_1}{\partial \omega}\right)^2 + \left(\frac{\partial \varepsilon_2}{\partial \omega}\right)^2}}(1+\eta).$$

Usually $\eta << 1$ holds. For free-electron metals described via a Drude model, Γ reduces to the Drude relaxation frequency γ. Figure 3-5 shows calculated plasmon decay times T_1 for Au (a) and Ag (b) nanoclusters using literature values of the dielectric functions [49, 53, 54].

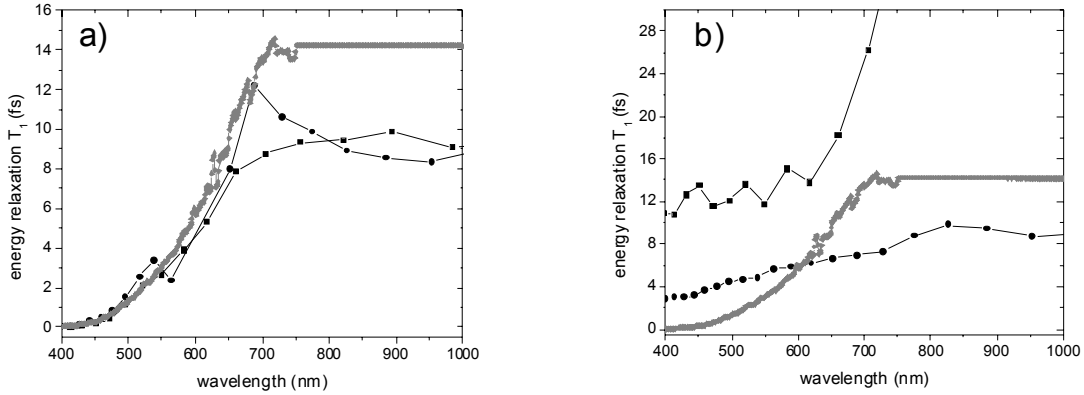

Figure 3-5: Plasmon decay time for Au (a) and Ag (b) nanoparticles using dielectric functions of Ref. [49] (black squares), [53] (black circles) and [54] (gray diamonds).

For Au nanoparticles, there is a close agreement between the decay times calculated using different sets of literature values for the dielectric function for wavelengths $\lambda < 700$ nm. The strong damping of the plasmon resonance below 700 nm is due to the absorption tail of the Au interband transitions, which extends from the band edge at 2.5 eV ($\approx$ 500 nm) down to 1.7 eV (725 nm). In this regime, a competition between plasmon excitation and d-sp interband absorption prevents efficient plasmon oscillations. Indeed, plasmon decay times of 4 fs have been reported for Au nanoparticles with a resonance wavelength $\lambda_0 = 632$ nm on a TiO_2 matrix [15], and similar values have been found from temporal studies of third harmonic generation in femtosecond spectroscopy experiments [55]. For Ag nanoparticles, there is a marked difference between the decay times calculated using the bulk dielectric data by reference [49] and references [53, 54] throughout the regime of optical wavelengths. Measurements of the decay time of silver clusters with resonance wavelengths 400 nm $< \lambda_0 <$ 630 nm yielded decay times between

2 and 4 fs [56], suggesting the use of the dielectric functions of references [53, 54] for estimations of the plasmon damping. Note that the decay times reported here are based solely on the optical conductivity (scattering of the electrons) as the damping mechanism and give thus only an upper limit for the plasmon decay time due to dephasing and interband transitions. Further decay processes such as Landau-damping and radiation damping lead to a further decrease of the plasmon decay time T_1. Radiation damping leading to energy relaxation via the emission of photons [57] is of increasing importance for larger particles ($D > 50$ nm) and leads to a red shift and broadening of the dipole resonance and excitation of higher order multipoles [58]. For very small particles ($D < 5$ nm), mostly elastic surface scattering events lead to significant resonance broadening due to a decrease of the pure dephasing time [59]. For very small clusters on substrates, chemical interface damping can be the dominating decay channel [60].

In summary, plasmon decay times $T_1 < 10$ fs can be expected for Au and Ag nanoparticles throughout the visible and near-infrared regime. This will limit the maximum size of waveguides based on plasmon-polariton excitations in noble metal nanoparticles to the submicron regime [16, 17].

3.2 Near-field particle interactions in plasmon waveguides

Advances in particle synthesis and fabrication have enabled the study of electromagnetic interactions between metal nanoparticles in ordered arrays with various particle spacings d. Such nanoparticle arrays exhibit collective dipole resonances. For $d \geq \lambda$, the collective dipole resonance frequencies and the lifetime of the plasmon oscillations are influenced predominantly by far-field dipole interactions with a d^{-1}

distance dependence [61, 62]. For closely spaced metal nanoparticles ($d < \lambda$), interactions mediated by the high electromagnetic fields near the particle surface dominate with a d^{-3} distance dependence, as will be discussed below.

An intriguing application of the interaction between metal nanoparticles is the construction of waveguides for electromagnetic energy at visible or near-infrared frequencies. It was shown that far-field interactions between Au particles in a grating can establish a surface plasmon-polariton band gap in analogy to photonic crystals, allowing for the construction of line defect waveguides [63]. It has also been shown that the minimum size of these defect waveguides is determined by the diffraction limit $\lambda/2n$ of light due to the large spacing d between adjacent particles that is necessary for the establishment of the band gap.

The strong near-field interaction of individual metal nanoparticles with light can be used to fabricate waveguides for electromagnetic energy with a lateral confinement of the guided modes below the diffraction limit of light if energy can be transferred between nanoparticles. It has indeed been shown theoretically using both extended Mie-theory [16] and a model that treats the particles as point-dipoles [17] that the dipole field resulting from a plasmon oscillation in a single metal nanoparticle can induce a plasmon oscillation in a closely spaced (interparticle spacing $d << \lambda$) neighboring particle due to near-field electrodynamic interactions. Interactions between adjacent nanoparticles in such plasmon waveguides were shown to set up coupled plasmon-polariton modes, which lead to coherent energy transport along the array [17]. The recent finding that ordered arrays of closely spaced noble metal particles show a collective behavior under broad beam illumination supports such an interaction scheme [64]. We proposed the name

"plasmon waveguides" for structures operating on this principle and the name "plasmonics" for the field of study to draw attention to the energy guiding mechanism via surface plasmons.

In the following, the nature of the propagating modes will be discussed using the analytical point-dipole model [17, 28]. When metal nanoparticles are spaced closely together (separation a few tens of nanometers), as depicted in Figure 3-6, the strongly distance-dependent near-field term in the expansion of the electric dipole interaction dominates. The interaction strength and the relative phase of the electric field in neighboring particles are both polarization and frequency dependent. This interaction leads to coherent modes with a wave vector **k** along the nanoparticle array.

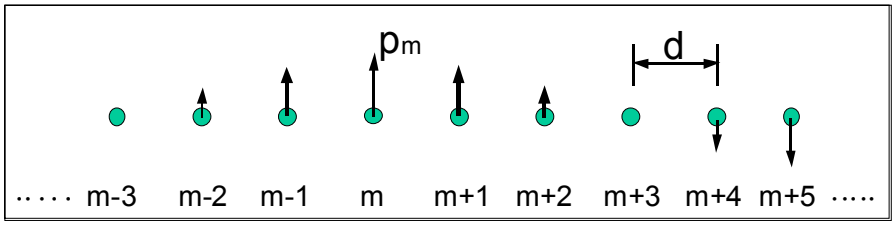

Figure 3-6: Geometry of a plasmon waveguide consisting of a chain of noble metal nanoparticles. The particles are modeled as point-dipoles with a nearest-neighbor spacing d. Each point-dipole m is attributed with a dipole moment p_m polarized either in the transverse or longitudinal direction (not shown).

One can calculate the dispersion relation $\omega(\mathbf{k})$ for energy propagation along the nanoparticle chain plasmon waveguide by modeling the chain as an one-dimensional system of coupled damped harmonic point-dipole oscillators spaced a distance $d << \lambda$ apart. Each point-dipole m is attributed with a dipole moment p_m polarized either along (longitudinal polarization) or perpendicular (transverse polarization) to the chain axis.

Taking only electromagnetic near-field interactions between adjacent point-dipoles of polarization i (longitudinal or transverse) into account, the equation of motion of an infinite chain of point-dipoles can be written as

$$\ddot{p}_{i,m} = -\omega_0^2 p_{i,m} - \Gamma_I \dot{p}_{i,m} + \frac{\Gamma_R}{\omega_0^2} \dddot{p}_{i,m} - \gamma_i \omega_1^2 \left(p_{i,m-1} + p_{i,m+1} \right).$$

This equation of motion consists of four terms. The plasmon dipole resonance is described by a harmonic oscillator term at frequency ω_0. Internal damping processes due to the optical conductivity are incorporated via the damping constant Γ_I, and radiation damping due to the oscillation of the conduction electrons [65] is modeled via a damping constant Γ_R. For Ag and Au nanoparticles in the point-dipole limit, $\Gamma_R << \Gamma_I$ holds, so the radiating oscillator damping term can be neglected [17]. The interaction between adjacent nanoparticles in the array can be taken into account via an interaction strength ω_1 derived from the electromagnetic near-field interaction term $\left(\propto d^{-3} \right)$ and a polarization-dependent constant γ_i.

Figure 3-7 shows the dispersion relation calculated using this point-dipole model for modes with the electric field polarized along the chain (longitudinal modes L) and for modes polarized perpendicular to the chain (transverse modes T). Calculations were done including nearest-neighbor coupling only (solid lines) and including up to five nearest neighbors in the coupling term (dotted lines) for an infinite linear array of point-dipoles. The inclusion of up to five nearest neighbors has little effect on the dispersion curves, confirming that in the point-dipole approximation the interaction is dominated by nearest

neighbor coupling. For both polarizations, the propagation or group velocity of the guided electromagnetic waves, given by the slope $\mathrm{d}\omega/\mathrm{d}\mathbf{k}$ of the dispersion relation, is highest at the single particle resonance frequency ω_0, corresponding to a wave vector $\mathbf{k} = \pi/2d$.

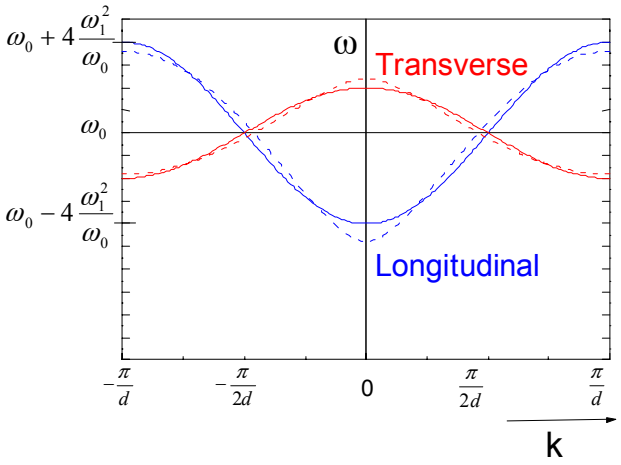

Figure 3-7 (color): Dispersion relation of a plasmon waveguide. The plot shows the dispersion relation for plasmon modes in a linear chain of metal nanoparticles with a twofold degenerate branch corresponding to transverse modes (red curves) and a branch corresponding to longitudinal modes (blue curves). Results are shown for calculations incorporating nearest-neighbor interactions only (solid curves), and including up to fifth-nearest neighbor interactions (dotted curves).

Specifically, the maximum group velocities $v_{\mathrm{maxL,T}}$ for both longitudinal (L) and transverse (T) modes calculate to

$$v_{\max L,T} = \frac{B_{L,T} \times d}{2},$$

where $B_{\mathrm{L,T}}$ is the bandwidth of the dispersion relation. Calculations for 50 nm Au spheres with a center-to-center distance of 75 nm in air show a maximum energy

propagation velocity $v_{\mathrm{maxL}} \approx 0.3c$. This is more than ten times faster than the saturation velocity of electrons in typical semiconductor devices.

Aside from the dispersion relation, another important parameter in waveguide design is loss. In plasmon waveguides, the loss can be due to radiation into the far-field and due to internal damping of the plasmon resonance. Radiation losses into the far-field are expected to be small due to the dominance of near-field coupling. Internal damping of the plasmon resonance is mainly due to resistive heating described by the plasmon linewidth Γ. At $\mathbf{k} = \pi/2d$, the plasmon amplitude decay lengths $\alpha_{\mathrm{L,T}}$ can be calculated using

$$\alpha_{L,T} \times d = \frac{\Gamma}{B_{L,T}}.$$

For the example of an Au plasmon waveguide discussed above, the corresponding energy decay length 2α amounts to 6dB/600nm for the longitudinal mode. This limits the transmission of electromagnetic energy in plasmon waveguides to the micron regime.

3.3 Routing and switching of electromagnetic energy in plasmon waveguides

The point-dipole theory of plasmon waveguides allows for the analysis of more complex structures such as 90-degree corners and tee structures for the routing and splitting of the electromagnetic energy flow [17]. Due to the strictly near-field nature of the coupling in this model, signals can be guided around 90-degree corners and split via tee structures with negligible radiation losses into the far-field at the discontinuity (see Figure 3-8). Power transmission coefficients for the guiding of energy around corners and

for signal splitting in tee structures were calculated by requiring continuity of the plasmon amplitude and of the energy flux at the corner where the wave gets partly transmitted and reflected. The transmission coefficients are a strong function of the frequency of the guided wave and its polarization, and show a maximum at the single particle dipole plasmon frequency ω_0. Transmission coefficients close to 100% are possible for propagation around 90-degree corners for certain polarizations, and lossless signal splitting was shown in tee structures [17].

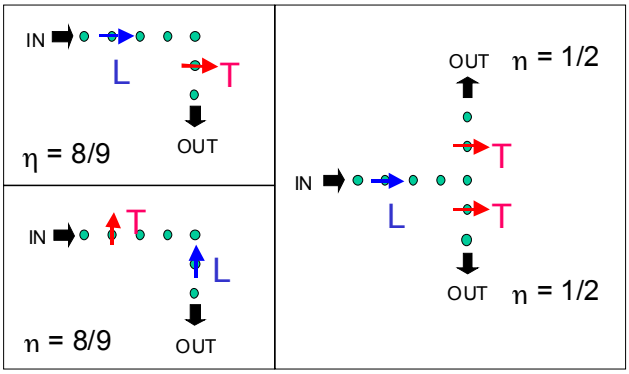

Figure 3-8 (color): Calculated power transmission coefficients η in plasmon waveguides for a 90-degree corner and a tee structure. The black arrows indicate the direction of the energy flow, the blue arrows indicate a longitudinal mode (L), and the red arrows indicate a transverse mode (T). An η value of 1 corresponds to 100% transmission.

Due to the coherent nature of the propagation, it is also possible to design all-optical modulators that rely on interference effects, such as Mach-Zehnder interferometers akin to the Yagi modulators discussed in section 2.4. Figure 3-9 shows the power modulation characteristic of an asymmetric modulator based on two guided waves interfering on a tee structure. Note that the dipole model predicts a perfect nulling if the two waves are of equal power and show a 180-degree phase difference.

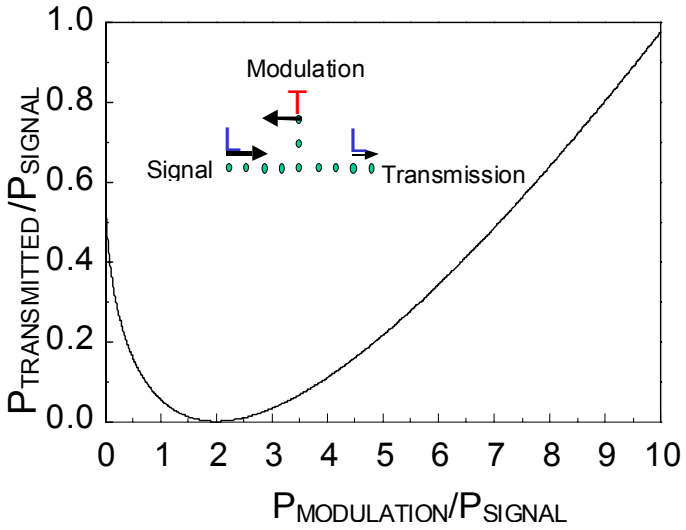

Figure 3-9 (color): A simulated nanoscale all-optical modulator. The plot shows the power modulation characteristic of an asymmetric tee modulator akin to the structures discussed in section 2.4 in the nearest-neighbor point-dipole limit. The signal and the modulation source are 180 degree out of phase. The black arrows indicate the polarization of the plasmon waves in the three arms of the tee.

3.4 Conclusions and limitations of the dipole model

The point-dipole model for energy transport in nanoscale plasmon waveguides predicts a high speed of information transport of about 10^7 m/s for waveguides consisting of noble metal particles in air. The femtosecond-timescale damping of plasmon oscillations in metal nanoparticles leads to high transmission losses due to resistive heating of about 6dB/0.5μm for Au nanoparticles in air, but small device dimensions for functional devices seem possible. Transmission, splitting and switching of signals could be potentially achieved in network structures consisting of linear plasmon waveguides.

This suggests that plasmonic devices are potential candidates for the fabrication of highly integrated optical circuits operating below the diffraction limit of light.

At the end of this chapter, two points regarding the point-dipole model deserve special attention. The first regards defects and deviations of the perfect one-dimensional translation symmetry of the nanoparticle arrays. Due to the strong distance dependence of the interparticle interaction in the point-dipole model, particle displacement and size variation lead to strong perturbations in the energy transport along the nanoparticle chains [17]. This leads to stringent requirements regarding fabrication methods for functional plasmon waveguides.

The second point that should be stressed is the fact that the point-dipole model for energy transport in plasmon waveguides is only an approximation. While plasmon oscillations of small metal nanoparticles with a diameter $D << \lambda$ indeed show a dipole-like field profile, the finite extent D of the particles leads to spatially extended charge distributions. Furthermore, the interparticle spacing d is of comparable magnitude to the diameter D of the nanoparticles constituting a plasmon waveguide. Thus, the point-dipole model of energy transport is likely to overestimate the interaction strength between adjacent nanoparticles. It is therefore important to carefully examine the validity of the results of a point-dipole analysis of plasmon waveguides.

Chapter 4 FDTD simulations of plasmon waveguides

4.1 Introduction

Finite-difference time-domain (FDTD) simulations solve the full set of Maxwell's equations on a grid and are a powerful method to model light-matter interactions in complex systems [66]. Using FDTD simulations, in this chapter an analysis of the near-field interactions of regularly spaced Au nanoparticles in air with an interparticle spacing $d << \lambda$ is presented. The dependence of the plasmon resonance frequency of the long-wavelength collective modes of plasmon waveguides on different nanoparticle chain lengths and interparticle spacings is discussed. Optical pulse propagation in plasmon waveguides is demonstrated. The predictions of the point-dipole model for the dispersion relation and pulse group velocities for energy transport in plasmon waveguides consisting of spherical nanoparticles are confirmed. Local excitation of transverse plasmon modes leads to anti-parallel group and phase velocities. Finally, the FDTD analysis is extended to spheroidal particles with an aspect ratio of 3:1 to demonstrate the ability to tune and improve the guiding properties of plasmon waveguides.

4.2 Collective far-field excitation of plasmon waveguides

In order to accurately model the material properties of Au, the dispersive behavior at visible frequencies as expressed by the dielectric function $\varepsilon(\omega) = \varepsilon_1(\omega) + i\varepsilon_2(\omega)$ has to be taken into account. Figure 4-1 shows literature values of $\varepsilon(\omega)$ obtained using

measurements on bulk films (gray circles and black squares) [49, 53] and on small Au nanoclusters with a 30 nm diameter (light gray squares) [54].

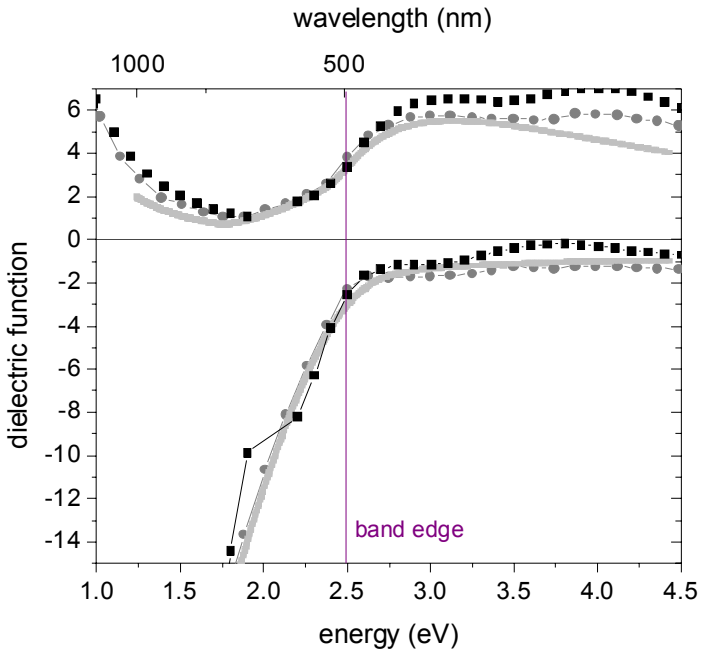

Figure 4-1: Real (lower curves) and imaginary (upper curves) part of the dielectric function of Au from the literature. Shown are data obtained from bulk measurements (gray circles [49], black squares [53]) and from measurements on Au clusters with a diameter of 30 nm (light gray squares [54].

The close agreement between the datasets implies that the dielectric function of Au nanoparticles with diameters $D > 30\,\text{nm}$ can be modeled using bulk values. Small differences in the imaginary part ε_2 due to increased surface scattering for small particles can be taken into account via an increased electron scattering time τ in numerical models.

Our FDTD simulation approach allows us to model the dielectric response of Au nanoparticles using a Drude model with a dielectric constant

$$\varepsilon(\omega) = 1 - \frac{\omega_p^2}{\omega(\omega + i\Gamma)}.$$

The free parameters to model the dielectric response of Au are the bulk plasmon frequency ω_p and the free electron scattering frequency Γ. We chose $\omega_p = 6.79\text{x}10^{15}$ rad/s in order to obtain a close match between the Drude model and the measured data around $\varepsilon_1 = -2$, which is the plasmon resonance condition of small spheres in air. In order to model the typical plasmon decay time τ of 4 fs for Au nanoparticles [15], we set the scattering frequency $\Gamma = 2.5\text{x}10^{14}$ rad/s.

Figure 4-2 describes our simulation approach for the determination of the dipole surface plasmon frequencies of Au nanoparticles for the case of a single Au sphere with a diameter of 50 nm in air. The simulation volume consists of a rectangular box of dimensions 1000 nm x 400 nm x 400 nm with the 50 nm Au sphere placed at the center as shown in the inset of Figure 4-2 a. The particles are surrounded by a medium with refractive index $n = 1$ (vacuum). The simulation box is overlaid with a rectangular grid of 1 million mesh points using a graded mesh density to ensure a high density of points near the particle. The dipole surface plasmon resonance of the nanoparticle is then determined using two simulation runs. In a first run, the nanoparticle is illuminated with a plane-wave propagating in the z-direction with the electric field polarized in the x-direction as shown in the inset of Figure 4-2 a. The frequency of the plane wave was chosen to be $6\text{x}10^{14}$ Hz (2.48 eV), as will be discussed below. The plane-wave illumination leads to the build-up of an oscillating homogeneous electric field inside the nanoparticle. A

snapshot of the electric field distribution inside the simulation volume is used as the initial field condition for a second simulation run without any external sources.

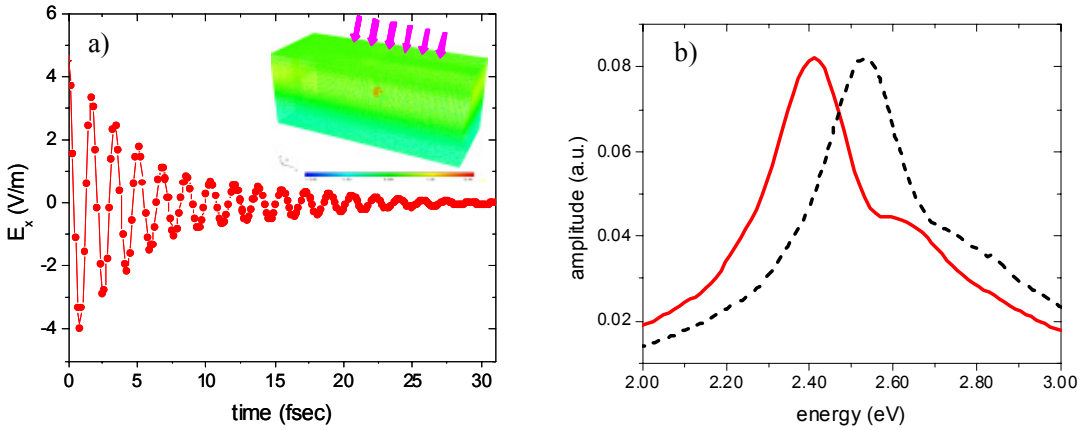

Figure 4-2 (color): Determination of the single particle plasmon resonance frequency. a) The inset shows the x-component of the electric field for a normal incidence plane-wave illumination of the simulation volume with a 50 nm Au sphere at the center. The plane wave sets up an enhanced electric field inside the particle (red color). The main graph shows the oscillatory decay of the enhanced field **E**(t) at the center of the nanoparticle after the plane wave is switched off. b) Fourier transform of **E**(t) with the dipole surface plasmon peak at 2.4 eV (red line). Also shown is the corresponding peak for a 10 nm Au sphere at 2.53 eV (black dotted line).

Figure 4-2 a shows the time evolution of the field at the center of the nanoparticle. The field decays in a damped harmonic oscillation $E(t)$ with the damping constant corresponding to the relaxation time τ of the Drude model. The Fourier transform of $E(t)$ shown in Figure 4-2 b (red line) displays a single dipole peak centered at 2.4 eV. The shoulder exhibited on the high energy side of the peak is an artifact caused by reflections at the boundaries of the simulation volume, as was verified using volumes of different sizes. The dipole peak corresponds to the position of the surface plasmon dipole resonance of the 50 nm Au sphere in air. The resonance is red-shifted compared to the

dipole resonance of a "small" Au particle at 2.58 eV obtained from quasi-static Mie-theory [13]. This red-shift is caused by radiation damping of the plasmon resonance since the particle diameter D of 50 nm is an appreciable fraction of the wavelength, so that the condition $D << \lambda$ for the quasi-static approximation does not strictly hold anymore. To verify our calculation method, we also calculated the resonance for a 10 nm Au sphere (black dotted line). In this case the dipole resonance is centered at 2.53 eV, close to the quasi-static value of 2.58 eV, demonstrating the validity of our model.

Two points regarding our simulation approach should be noted. First, the frequency of the plane wave chosen for the build-up of the initial electric field in the first simulation run is not required to be close to the plasmon resonance frequency of the investigated nanostructure in order to obtain the right position of the resonance peak, as was confirmed by a simulation run with a frequency of 3×10^{14} Hz (1.24 eV). However, a frequency close to the resonance leads to the build-up of a higher field inside the nanostructure than outside, which reduces surface polarization effects due to the initial outside field. This was seen to improve the shape of the dipole peak obtained by Fourier transform while not altering its peak position. Second, our model does not take into account a decrease in the width of the dipole resonance due to peak shifts to lower frequencies away from the onset of the interband transitions of bulk Au. This is due to the fixed electron relaxation time τ of the Drude model.

In order to determine the collective resonance energies $E_{L,T}$ of plasmon waveguide particle chains, the simulation volume is initialized with an electrostatic field chosen to resemble the $\mathbf{k} = 0$ mode profile polarized either parallel (L-modes) or perpendicular (T-modes) to the chain direction. Figure 4-3 shows an example of the field distribution

around a plasmon waveguide consisting of 5 Au nanoparticles obtained using illumination with an x-polarized plane wave propagating in the +z direction. The field is then allowed to evolve for 35 fs, and its time-dependence is analyzed to determine the resonance energies as described above.

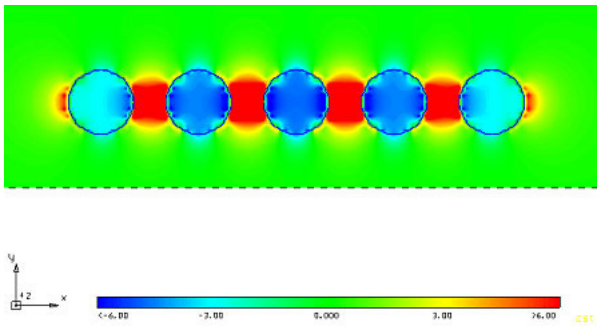

Figure 4-3 (color): Collective excitation of a plasmon waveguide. The contour plot shows the distribution of the x-component of the electric field around a five particle plasmon waveguide structure illuminated by an x-polarized plane wave propagating in the +z direction. The frequency of the plane wave is close to the collective resonance frequency of the particle array, hence the enhanced electric field inside and between the nanoparticles.

Figure 4-4 shows the position of the plasmon resonances of 50 nm Au spheres in air in nanoparticle chains of different lengths and inter-particle spacings for polarizations along (longitudinal modes L, blue squares) and perpendicular (transverse modes T, red circles) to the chain axis. Since all the particles constituting the chains are excited in phase, the plasmon resonances correspond to collective longitudinal and transverse modes of the chain as a whole. Figure 4-4 a shows the resonance energies for both polarizations for particle chains with up to 6 particles with an interparticle center-to-center spacing d of 75 nm, corresponding to $1.5D$. These resonance positions are taken as the averages of the resonance frequencies obtained for each nanoparticle in the chain. In

the case of a single Au sphere, the longitudinal and transverse resonances coincide at a resonance energy E_0 due to its spherical symmetry. For increasing particle chain lengths, the plasmon resonance energy E_L (for L polarization) shifts to lower and the energy E_T (for T polarization) to higher frequencies due to near-field interactions between the particles. The peak splitting $\Delta E = |E_T - E_L|$ saturates for particle chain lengths of 5 particles at $\Delta E \approx 200$ meV. The fact that the splitting has not yet saturated for particle chains of 3 particles shows that the coupling is not governed by nearest-neighbor interactions alone. Our results qualitatively agree with calculations for the interaction of silver nanoparticles based on Mie-theory [67] and rigorous solutions of Maxwell's equations for aggregated metal spheres [68].

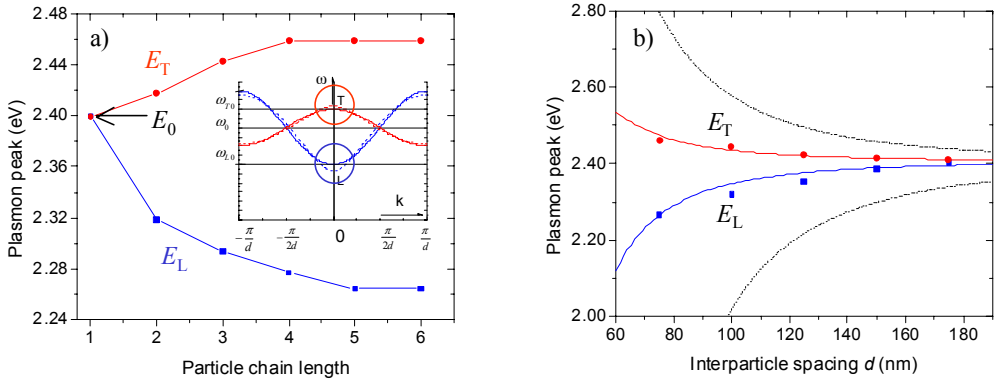

Figure 4-4 (color): Collective resonance energies of nanoparticle chain arrays. The plots show the position of the dipole resonance of 50 nm Au spheres in nanoparticle chains for a polarization along (longitudinal mode L, blue squares) and perpendicular (transverse mode T, red circles) to the chain axis, corresponding to the **k**=0 modes of the dispersion relation. a) Dependence on particle chain length with an interparticle spacing of 75 nm. b) Dependence on interparticle spacing for a chain length of 5 particles. Also shown is the dependence calculated using the point-dipole model [17] for surrounding media with n=1 (black dotted lines) and n=2.5 (blue and red lines).

Figure 4-4 b shows the dependence of the plasmon peaks $E_{L,T}$ for chains of 5 Au spheres with a diameter of 50 nm on interparticle spacing d. The peak splitting is seen to decrease with increasing interparticle spacing as d^{-3}, and for $d = 175$ nm ($3.5D$) the peaks practically coincide ($\Delta E \approx 0$). This strong dependence of the peak splitting ΔE on the interparticle spacing is characteristic for near-field interactions, and similar trends were observed in experiments using far-field spectroscopy of plasmon waveguides fabricated using electron beam lithography on ITO coated glass slides [32, 33] as described in Chapter 5. Figure 4-4 b also shows the functional dependencies for $E_{L,T}$ on the interparticle spacing as predicted by the point-dipole model for plasmon waveguides [17] of our geometry (black dotted line). While the functional form of the peak splitting decrease with increasing interparticle spacing can be well described via the point-dipole model, the absolute magnitude of the splitting is clearly overestimated. However, the experimental data is well fitted using a point-dipole model with a coupling strength reduced by a factor 6.25 (corresponding to particles embedded in an effective medium with $n = 2.5$, blue and red solid lines). This reduced coupling strength can be attributed to the fact that the 50 nm Au spheres do not behave as perfect point dipoles due to their extended charge distributions.

The peak splitting ΔE and the known functional form of the point-dipole dispersion relation $\omega(\mathbf{k})$ allow for the calculation of the maximum group velocities v_g and the energy decay lengths of the $\mathbf{k} = \pi/2d$ mode as described in section 3.2. For a peak splitting of $200\,\text{meV}$, we find $v_{gL} = 1.6\text{x}10^7$ m/s for longitudinal and $v_{gT} = 6.6\text{x}10^6$ m/s for transverse excitations. Assuming a plasmon decay time $\tau = 4$ fs for a single nanoparticle [15], the

corresponding energy decay lengths are α_L = 6dB/100nm and α_T = 6dB/40nm, respectively. The magnitude of the calculated group velocity and energy decay length are about one order of magnitude lower than the predictions of the point-dipole model [17], due to the decreased near-field coupling strength as discussed above.

A use of plasmon waveguides as means for energy transport in nanoscale optical circuits would require a reduction of the damping constant by one order of magnitude in order to allow for guiding of electromagnetic energy over distances of several hundred nanometers. This can be achieved either via an increase in the near-field coupling strength or an increase in the particle plasmon damping time τ. It has recently been shown that for Au nanoparticles a particle geometry change that red-shifts the plasmon resonance away from the interband transition edge can increase the damping time up to a factor 3 compared to nanospheres [69]. FDTD calculations of corresponding plasmon waveguides will be presented in section 4.4.

4.3 Locally excited plasmon waveguides

The obtained values for the group velocities v_g and energy attenuation lengths α rely on the analytical but approximate point-dipole model of plasmon waveguides. In order to determine the functional form of the dispersion relation $\omega(\mathbf{k})$ with a more realistic model, the propagation of electromagnetic energy through plasmon waveguide structures consisting of 9 periodically spaced Au nanospheres with a diameter D = 50 nm and a center-to-center spacing d = 75 nm was simulated using FDTD calculations. The waveguides were excited with an oscillating point-dipole placed at a distance d = 75 nm to the center of the first nanoparticle of the waveguide. In consecutive runs, the point-

dipole source was driven continuously at various frequencies in the vicinity of E_0. The field distribution along the nanoparticle chain structure, shown in Figure 4-5 for a longitudinal excitation at E_0, was then analyzed to determine the wave vector **k** of the propagating waves.

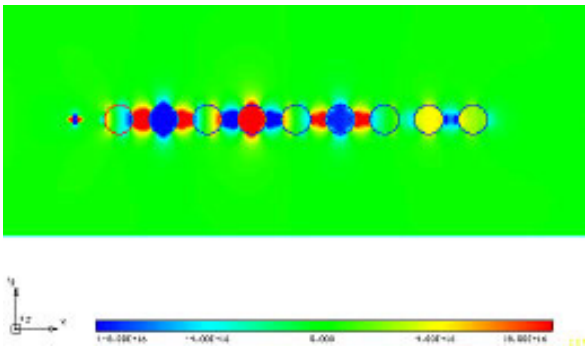

Figure 4-5 (color): Simulation of a locally excited plasmon waveguide. The contour plot shows the distribution of the x-component of the electric field around a plasmon waveguide excited by a local point-dipole source driven at E_0 with longitudinal polarization. A spatial period of 4 particle spacings can be clearly seen, corresponding to a $\mathbf{k}=\pi/2d$ mode.

Figure 4-6 a shows the thus computed dispersion relation for both longitudinal (blue squares) and transverse (red triangles) excitations, as well as the results for the $\mathbf{k} = 0$ modes obtained by plane wave excitation (circles). The dotted lines indicate the dispersion relation calculated using the point-dipole model. The obtained $\omega(\mathbf{k})$ data are in excellent agreement with the predictions from the point-dipole model despite the limitations of the latter. Figure 4-6 b shows the electric field amplitude at the center of the last nanoparticle for longitudinal excitations (blue squares). Note that the waveguide loss is minimum at the center of the dispersion band, as expected since the group velocity is maximum at this point [17]. The corresponding field amplitudes for transverse modes

(red triangles) were monitored in particle 2 because of the relatively high loss under transverse excitations, which makes a monitoring at the last particle difficult.

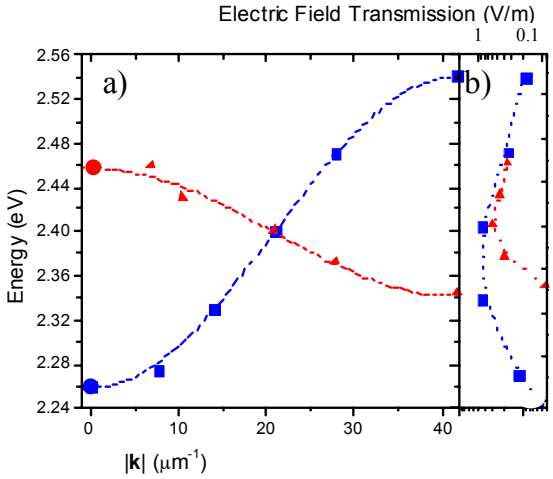

Figure 4-6 (color): Dispersion relation of plasmon waveguides obtained using FDTD simulations. a) Dispersion relation $\omega(\mathbf{k})$ for plasmon waveguides consisting of spherical particles for both longitudinal (blue squares) and transverse (red triangles) modes obtained by finite-difference time-domain calculations. Also shown are the positions of the $\mathbf{k}$=0 modes (circles) obtained from in-phase excitations and the functional dependence predicted by the point-dipole model [17] (dotted lines). b) For both longitudinal (blue squares) and transverse (red triangles) modes, the transmitted electric field (shown on top axis normalized to the field inside the first particle) in a selected particle is highest when the first particle is excited at the band center.

The previous analysis has produced an accurate description of the dispersion relation, but provided no direct evidence for the possibility of information transport using optical pulses. Therefore, the propagation of pulses through these plasmon waveguides was also examined by driving the local dipole source with a pulse centered at the resonance energy $E_0 = 2.4$ eV, corresponding to the $\mathbf{k} = \pi/2d$ mode with the highest group velocities. The width of the pulses was chosen to be 95 % of the bandwidth of the dispersion relation for each polarization in order to keep the pulse length of 30 fs well within the total simulation time of 125 fs. The upper inset of Figure 4-7 shows a snapshot of the x-

component of the electric field in the xy-plane for longitudinal polarization on a linear color scale. The periodicity of the field distribution along the chain confirms that the pulse is centered around the $\mathbf{k} = \pi/2d$ mode corresponding to a wavelength of 4 particle spacings. An analogous snapshot for the y-component of the electric field for transverse polarization is shown in the lower inset. The main part of Figure 4-7 shows the pulse position, defined as the location of maximum field amplitude, over time for both longitudinal (black squares) and transverse (black triangles) excitation. Linear fits of the datasets yield values for the group velocities of $v_{gL}^{*} = 1.7\times10^{7}$ m/s and $v_{gT}^{*} = 5.7\times10^{6}$ m/s, in good agreement with the estimates v_{gL} and v_{gT} from the point-dipole model ($v_{gL} = 0.94\times v_{gL}^{*}$ and $v_{gT} = 1.15\times v_{gT}^{*}$).

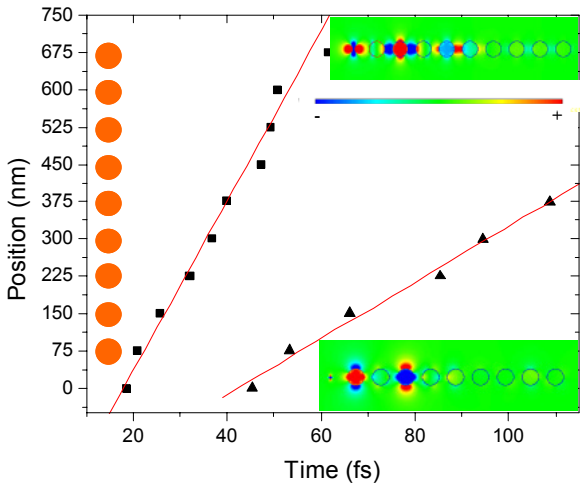

Figure 4-7 (color): Pulsed local excitation of plasmon waveguides. The plot shows the pulse peak positions over time in a plasmon waveguide consisting of spherical particles for both longitudinal (black squares) and transverse (black triangles) polarization. The spheres along the ordinate indicate the position of the Au nanoparticles. Snapshots of the x (y) – component of the electric field in the xy-plane for longitudinal (transverse) polarization are shown in the upper (lower) inset.

The energy decay lengths can be obtained from the pulse propagation simulations by monitoring the pulse height expressed as the maximum field amplitude at the center of each nanoparticle as shown in Figure 4-8 for longitudinal polarization (black line). The energy decay lengths are $\alpha_L^* = 6\text{dB}/280\text{nm}$ and $\alpha_T^* = 6\text{dB}/86\text{nm}$, respectively. Both are between a factor 2-3 higher than the energy decay lengths calculated using the point-dipole model with a plasmon decay time $\tau = 4$ fs. This discrepancy may be due to the finite size of our waveguide, resulting in a discrete spectrum of allowed modes. Nevertheless, these FDTD calculations quantitatively confirm the possibility of using plasmon waveguides for information transport with $v_g > 0.01\text{c}$.

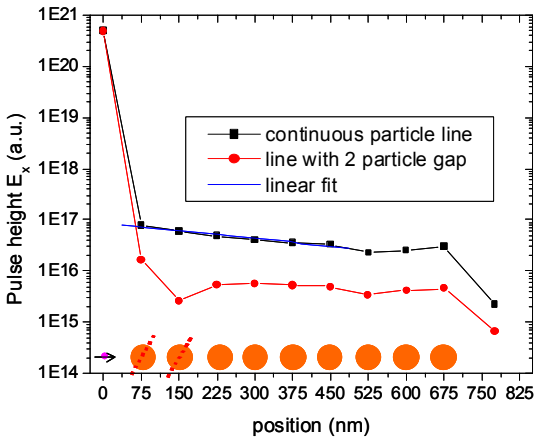

Figure 4-8 (color): Energy decay during pulse propagation in plasmon waveguides. The plot shows the maximum field amplitudes of a longitudinally polarized pulse monitored at the source position and at the center of each nanoparticle (black line) traveling through a plasmon waveguide. Also shown is data for a plasmon waveguide with the first two particles removed (red line), resulting in a decreased pulse height inside the last particle. The initial drop after the source is partly due to the point-dipole-like nature of the source.

Figure 4-8 also shows results for a plasmon waveguide with the first two particles after the source removed (red dataset), resulting in a decreased pulse height at the last

particle by about a factor 10. This directly confirms that the guiding is due to particle interactions.

The FDTD calculations clearly show the occurrence of negative phase velocities in these plasmon waveguides when excited in a transverse mode. For the transverse pulse, the group velocity and thus the direction of energy propagation and the phase velocity of the individual wave components are anti-parallel. This is illustrated in Figure 4-9, which shows three electric field snapshots spaced $\Delta t = 0.166$ fs ($\approx$10% of a cycle at E_0) apart. The wave packet is seen to move away from the source while the individual phase fronts travel towards the source. This is caused by the fact that for transverse modes a positive group velocity, required for causality, occurs at negative wave vectors **k**, as seen in the dispersion relation depicted in Figure 3-7. Plasmon waveguides could thus serve as a relatively simple model system for the investigation of negative phase velocity systems and be of value in the present discussions regarding the unique properties of these systems [70, 71].

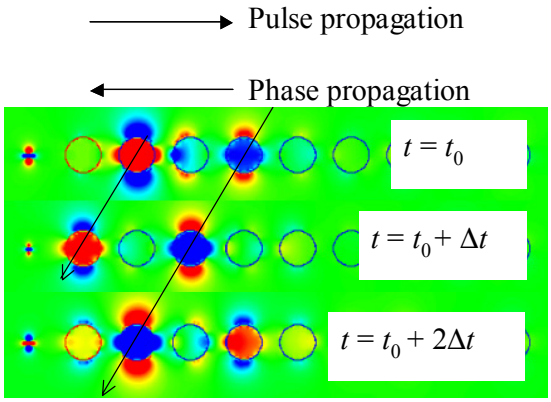

Figure 4-9 (color): Negative phase velocity in plasmon waveguides. The plots show time snapshots of the electric field for transverse pulse propagation showing negative phase velocity with anti-parallel orientation of the phase and group velocities.

4.4 Tailoring of the guiding properties by particle design

The previous analysis dealt exclusively with spherical particles. The energy guiding properties of plasmon waveguides can be optimized by a change in particle geometry to non-spherical particles as suggested by calculations based on extensions of the Mie-theory to ellipsoidal particles [72]. Rod-shaped nanoparticles with their long axis oriented perpendicular to the waveguide chain axis show an increased interparticle coupling compared to spherical particles that have the same particle volume and center-to-center spacing, as will be shown in the discussion of fabricated plasmon waveguides in section 5.4. Additionally, gold nanorods with an aspect ratio of 3:1 were shown to exhibit an increase in plasmon decay time τ by about a factor 2-3 due to a resonance shift away from the interband transition edge [69]. In order to analyze the effects of the particle shape on the group velocities for pulse propagation, we performed FDTD simulations with pulsed local excitations as described above on two plasmon waveguides consisting of spheroidal particles with an aspect ratio of 3:1 and their long axes oriented perpendicular to the waveguide axis. In the first case, the spheroids were chosen to be of the same volume and center-to-center spacing $d = 75$ nm as the 50 nm Au spheres described above, corresponding to a short axis $a = 34.7$ nm and a long axis $c = 104$ nm. The lower inset of Figure 4-10 shows a snapshot of the y-component of the electric field in the xy-plane for the propagation of a transverse pulse centered at the resonance frequency E_0 for this system, showing the $\mathbf{k} = \pi/2d$ periodicity.

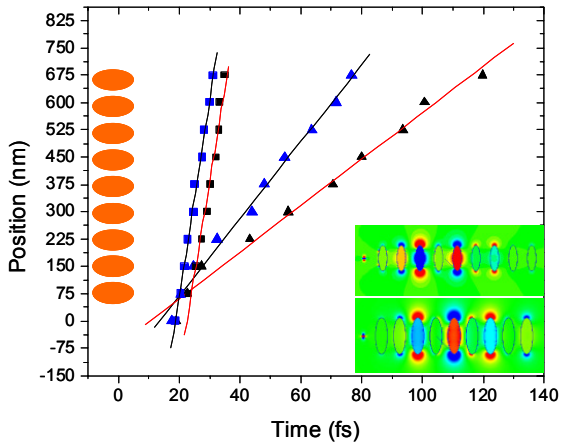

Figure 4-10 (color): Pulse propagation through spheroidal plasmon waveguides. The plot shows the pulse peak positions over time in plasmon waveguides consisting of spheroidal particles with an aspect ratio 3:1 for both longitudinal (squares) and transverse (triangles) polarizations. Shown are data for particles with the same volume as the spherical particles of **Figure 4-7** (case I, black datapoints) and for particles with an increased volume but the same short axis and surface-to-surface spacing (case II, blue datapoints). The spheroids along the ordinate indicate the position of the Au nanoparticles. The insets show field distributions of transverse pulse propagation through the waveguides for case I (lower inset) and case II (upper inset).

The main part of Figure 4-10 shows the position of the propagating pulse peaks over time for both transverse polarization (electric field polarized along the long spheroid axis, black triangles) and longitudinal polarization (electric field polarized along the short spheroid axis, black squares). Also shown are linear fits to the datasets, corresponding to group velocities $v_{3:1,T} = 6.4\text{x}10^6$ m/s and $v_{3:1,L} = 5.1\text{x}10^7$ m/s. These values are indeed larger than observed for spherical particles. For the transverse mode, the relative increase in the group velocity compared to the case of spherical particles is 12% only, even though the bandwidth obtained from the $\mathbf{k} = 0$ in-phase calculations increases by about a factor 4.5, as will be discussed in section 5.4. Conversely, for the longitudinal mode the relative increase in group velocity for the longitudinal mode is 300%, while in this case the

bandwidth does not change appreciably when going from spherical to spheroidal particles. The fact that v_g is not linearly related to ΔE suggests that $\omega(\mathbf{k})$ is strongly affected by the aspect ratio of the nanoparticles. The observed behavior could be caused by the increased radiation damping of transverse modes due to a non-homogenous polarization along the long axis, which in this geometry is no longer small compared to the wavelength λ of the exciting light [73].

The second case we investigated concerned plasmon waveguides consisting of spheroids with the same center-to-center spacing but with a larger volume (a = 50 nm and c = 150 nm) than the 50 nm diameter nanospheres. Note that these structures show an interparticle surface-to-surface spacing of 25 nm, at the limit of current electron beam lithography fabrication techniques. The results from FDTD calculations are also shown in Figure 4-10. The upper inset of Figure 4-10 shows a snapshot of the y-component of the electric field during the propagation of a transverse pulse on this structure. In this case, the maximum group velocities increase to $v^*_{3:1,T} = 1.06\times10^7$ m/s (blue triangles) and $v^*_{3:1,L} = 5.4\times10^7$ m/s (blue squares). The waveguide properties can thus be optimized by tuning the particle geometry.

4.5 Conclusions and outlook

In summary, FDTD simulations show that plasmon waveguides consisting of closely spaced Au nanoparticles allow for optical pulse propagation below the diffraction limit. The shape of the dispersion relation $\omega(\mathbf{k})$ for spherical particles obtained from FDTD calculations closely agrees with that predicted by a point-dipole calculation [17]. For spherical particles in air, the group velocities are about $0.02c$ - $0.06c$ depending on

polarization. The guiding properties can be optimized by changes in particle shape and spacing, resulting in group velocities of up to 0.2*c* for geometries that can be achieved using current fabrication techniques such as electron beam lithography. Plasmon waveguides thus have the potential to be applied in future highly integrated optical circuits, enable confinement and transport of electromagnetic energy below the diffraction limit and can be used as a model system for the study of light-matter interactions on the nanoscale.

Our FDTD simulations show that fabricated plasmon waveguides will show relatively large losses with 6dB energy decay lengths on the order of hundreds of nanometers. This will limit the size of plasmon waveguides for the propagation of electromagnetic energy to the submicron regime. In order to assess the potential use for plasmon waveguides in integrated optical devices, it is thus important to examine the possibility of attaining optical functionality for the routing and switching of electromagnetic energy on this length scale, as discussed in section 3.3. FDTD simulations can be a valuable tool for the initial examination of such devices. Figure 4-11 shows an example of a short 90-degree corner structure excited with an x-polarized pulsed point-dipole source. A comparison of the field distribution of the complete corner structure (Figure 4-11 a) with the distribution around an incomplete corner structure where one arm was removed (Figure 4-11 b) allows for the estimation of the guiding effect of the 90-degree plasmon waveguide corner. A rigorous analysis of the power transmission coefficients around the 90-degree discontinuity is complicated due to the fact that both arms of the corner need to be short to keep the simulation time manageable, leading to multiple reflections at the

discontinuity and the ends of the waveguides. This initial analysis can thus at best give estimates for the expected transmission coefficients.

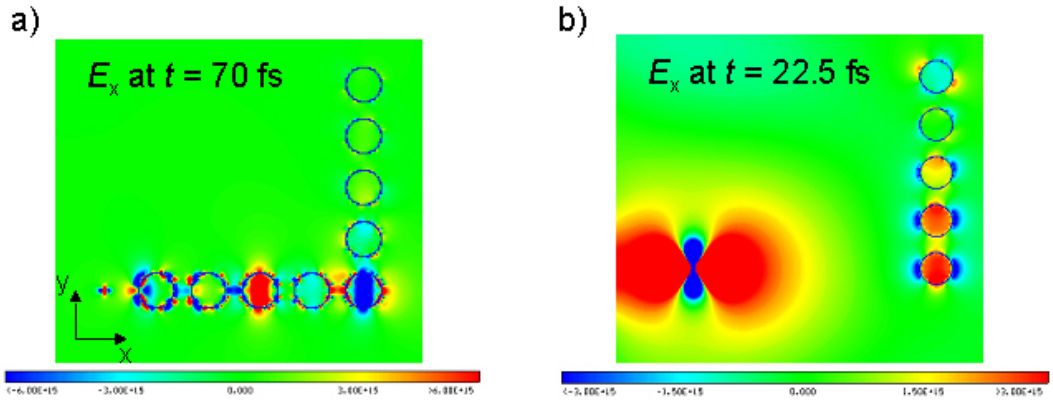

Figure 4-11 (color): FDTD simulation of a 90-degree corner plasmon waveguide. a) Time snapshot of the distribution of the x-component of the electric field around a short 90-degree corner plasmon waveguide excited by an x-polarized pulsed point-dipole source on the bottom left. The effect of the horizontal arm on the field inside the vertical arm can be assessed by comparison with a structure where the horizontal arm was taken out (b).

The analysis of the field distribution in both arms of the corner structure of Figure 4-11 a allows the estimation of the power transmission coefficient for the case of a longitudinal plasmon wave in the horizontal and a transverse plasmon wave in the vertical arm. For the simulated pulse centered around the single particle resonance energy E_0, the power transmission coefficient amounts to 12%, compared to a point-dipole model prediction of 88% for a plasmon-polariton wave at E_0 [17]. The corresponding transmission coefficient for an out-of plane excitation, leading to transverse plasmon modes in both arms, is 28%, compared to a point-dipole model prediction of 100%. The reduced transmission coefficients are partly due to radiation losses into the far-field and partly due to the finite extent of the corner arms, leading to reflections, which interfere

with the original wave. In addition, the transmission coefficients of different wave components of a pulse will in general be different. In order to assess the power transmission coefficients more carefully, simulations of larger corner arms are clearly called for, and the transmission coefficients of different pulse components have to be analyzed using Fourier transforms of the original and transmitted pulse. It is nonetheless interesting to point out the observation that the amplitude of the original pulse as it reaches the last particle of the corner structure on the top right is larger for an incomplete corner structure (Figure 4-11 b) compared to a complete corner (Figure 4-11 a). This is due to the fact that the resonantly enhanced absorption of the horizontal arm leads to a decreased amount of direct source radiation reaching the vertical arm.

In addition to passive corner and tee guiding structures for the routing of electromagnetic energy, all-optical switches employing interference between different plasmon waves could allow for the fabrication of active devices operating below the diffraction limit of light. The operation of such devices will be based on the interference of several plasmon-polariton waves with phase differences akin to a Mach-Zehnder interferometer. Figure 4-12 shows results of FDTD calculations of the field distribution around a linear plasmon waveguide consisting of nine spherical Au nanoparticles excited from both ends with pulsed point-dipolar sources for a phase difference between the sources of 180 degrees (Figure 4-12 a) and a phase difference of 0 (Figure 4-12 b).

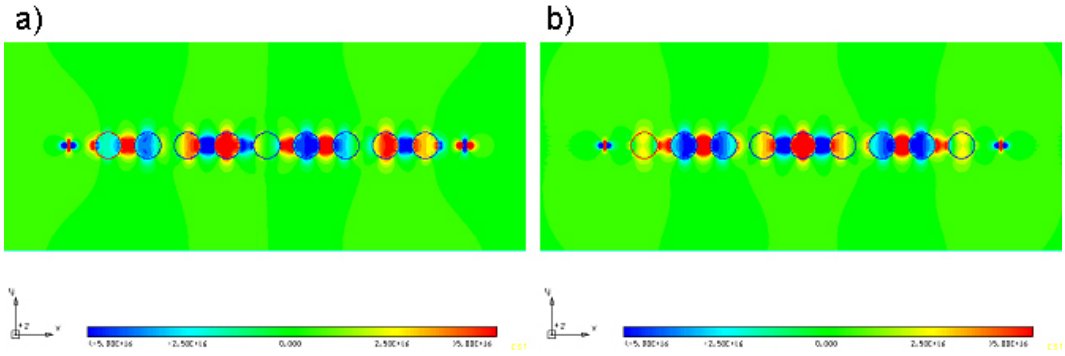

Figure 4-12 (color): Interference on plasmon waveguides. The contour plots show a time snapshot of the distribution of the x-component of the electric field around a plasmon waveguide structure excited by two x-polarized pulsed point-dipole sources placed on both sides of the waveguide on the waveguide axis. The field strength at the center particle differs for this particular snapshot by a factor 25 for sources driven 180 degree out of phase (a) and in phase (b).

The interference of the launched waves leads to a difference in field strength of a factor 25 between constructive and destructive interference at the center particle of the waveguide for this particular time snapshot, demonstrating the principle. A more detailed discussion would have to focus on time averages of the energy density for the determination of interference effects on the power distribution in plasmon waveguides. It is expected that FDTD simulations of more complex and larger plasmon waveguide structures will enable the determination of device properties of all-optical modulators and similar active devices.

Chapter 5 Fabrication and far-field properties of plasmon waveguides

5.1 Introduction

This chapter presents various approaches for the fabrication of plasmon waveguides consisting of Au and Ag nanoparticles and their far-field optical characterization for an estimation of the energy guiding parameters. Since the position and width of the plasmon dipole resonance depend on the shape and size of the metal particle, the applied fabrication methods should produce a narrow size distribution of the individual particles. Furthermore, a regular particle spacing is crucial for the transport properties due to the strong distance dependence of the electromagnetic near-field.

We have chosen Au and Ag nanoparticles with diameters between 30 and 100 nm as building blocks for plasmon waveguides. Gold and silver particles in this size regime are small enough to allow for an efficient excitation of the dipole plasmon mode only and large enough to show no enhanced damping due to surface scattering of the conduction electrons [13]. However, radiation damping can lead to an increased damping for particles with diameters $D > 50$ nm. The resonances in particles with diameters below 100 nm are conveniently located in the visible and near-infrared part of the electromagnetic spectrum for a variety of substrates and hosts (Figure 5-1). The center-to-center distance between particles was chosen to be on the same order as the particle diameter to ensure an efficient near-field coupling. The achievable minimum interparticle distance is mostly determined by the fabrication method, as will be shown.

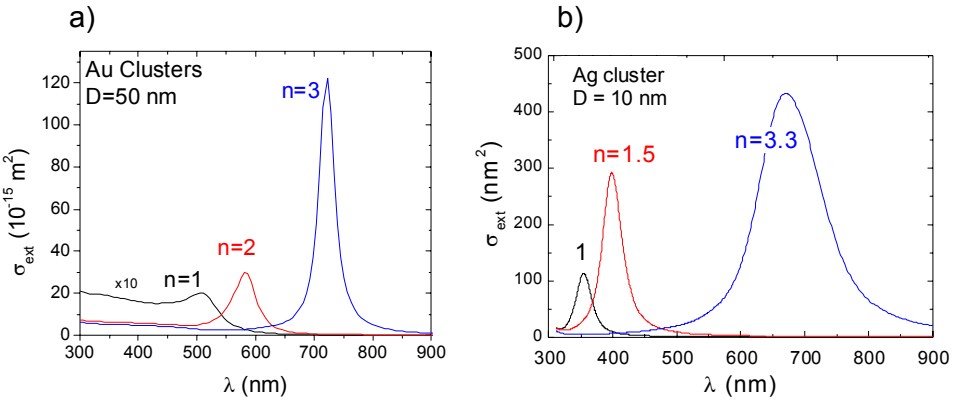

Figure 5-1 (color): Extinction coefficients of spherical Au (a) and Ag (b) clusters of diameter *D* embedded in non-absorbing matrixes of refractive index *n* calculated using quasi-static Mie-theory [47].

5.2 Fabrication of plasmon waveguides

The ease of fabrication of colloidal Au and Ag nanoparticles suggests the use of colloids as building blocks of plasmon waveguides. Colloidal particles that have been randomly deposited on a glass slide covered with a sticky poly-lysine layer can be manipulated using the tip of an atomic force microscope (AFM). Figure 5-2 shows successive AFM images of 30 nm Au particles, which were pushed into a straight line using a dedicated AFM system and manipulation software. The particles were assembled in a straight line with the feedback of the AFM turned off, and subsequently imaged with feedback in non-contact mode.

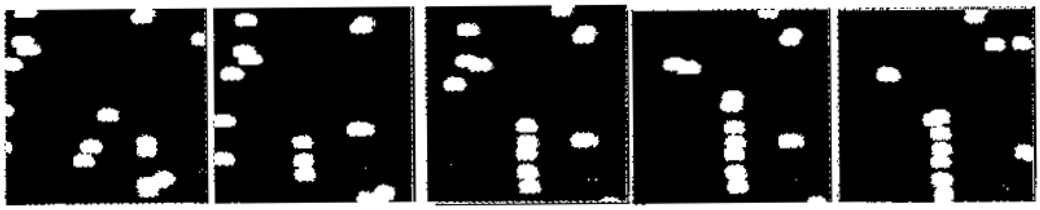

Figure 5-2: Atomic force microscopy fabrication of plasmon waveguides (I). Atomic force microscopy scans of 30 nm Au colloids deposited on a poly-lysine coated glass slide. Starting out from a random deposition, successive scans (from left to right) show the same 1x1 μm^2 area as the particles are pushed into a straight line using the tip of the atomic force microscope (courtesy of Sheffer Meltzer).

Figure 5-3 shows an AFM picture of the largest nanoparticle chain assembled using this method consisting of 10 colloidal 30 nm Au spheres. The control of the particle spacing is limited by the lateral resolution of the AFM, which makes the fabrication of one-dimensional particle arrays with a strict periodicity difficult. Nevertheless, the advantage of AFM manipulation lies in the fact that complex materials such as core-shell particles can be used as building blocks for plasmon waveguides, allowing for the possible fabrication of functional devices consisting of different materials.

Figure 5-3: Atomic force microscopy fabrication of plasmon waveguides (II). Atomic force microscopy scan of a 10 particle plasmon waveguide consisting of 30 nm colloidal Au particles. The scan shows a 1x1 μm^2 area after the randomly deposited particles were pushed in place using the AFM tip (courtesy of Sheffer Meltzer).

Another method for the fabrication of ordered arrays of noble metal nanoparticles is electron beam lithography (EBL) [18]. A schematic of the steps involved in this fabrication process is depicted in Figure 5-4. Structures can be fabricated using any material that withstands the lift-off process, such as metals and various oxides.

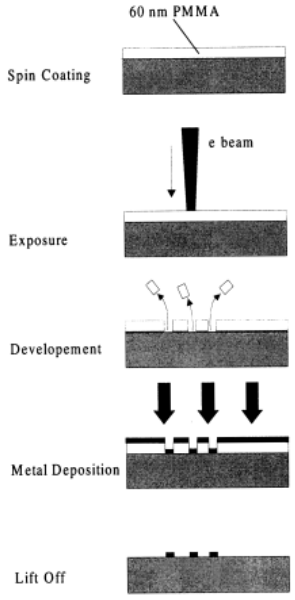

Figure 5-4: Schematic of the steps involved in an electron beam lithography fabrication process of metal nanoparticles.

Using EBL, plasmon waveguides consisting of up to 80 closely spaced Au and Ag nanoparticles with diameters between 30 and 50 nm and center-to-center spacings between 75 und 125 nm were fabricated. Examples are shown in the scanning electron micrographs of Figure 5-5. EBL provides excellent size and distance control of the nanoparticles constituting the waveguides. In order to minimize charging effects during fabrication, the structures were fabricated on a quartz glass slide covered with a thin indium-tin-oxide (ITO) layer. The layer thickness was chosen to be less than 10 nm to

suppress guiding of EM energy at the frequencies of interest [74]. The height of the fabricated nanoparticles was confirmed using atomic force microscopy. The following section will describe the optical analysis of particle interactions in these plasmon waveguides using far-field polarization spectroscopy.

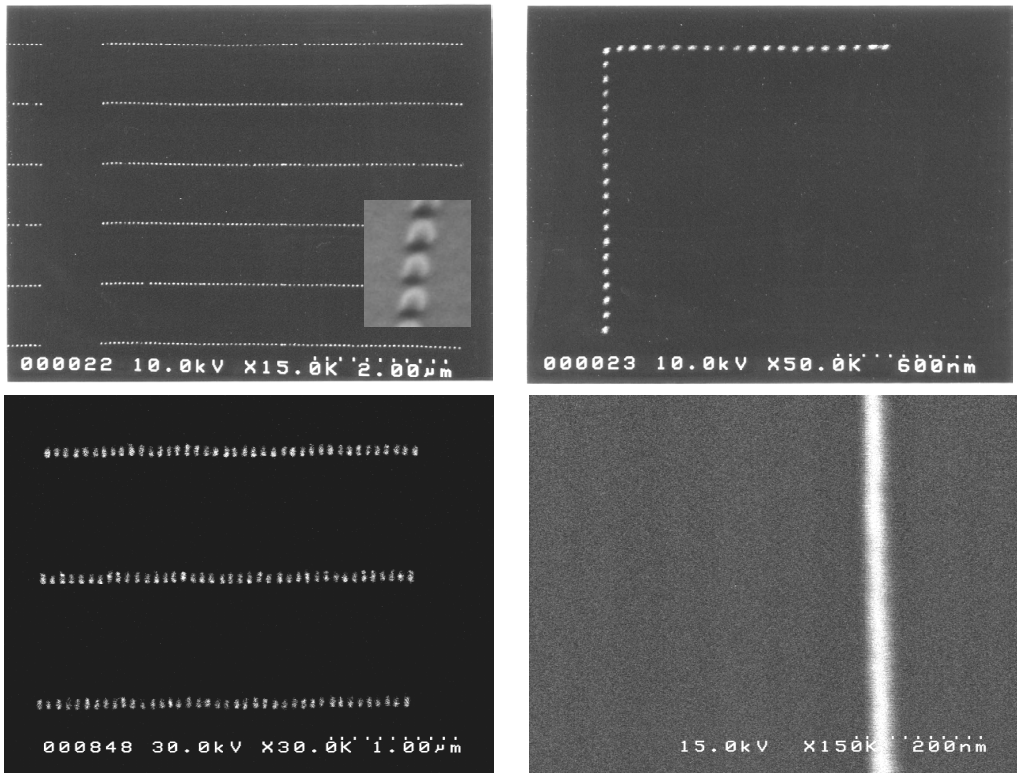

Figure 5-5: Plasmon waveguides fabricated using electron beam lithography. Scanning electron micrographs of plasmon waveguides consisting of spherical 50 nm Au particles taken at normal incidence of the electron beam (top row). The inset shows a micrograph where the sample stage was tilted by 70 degrees to visualize the almost spherical shape of the nanoparticles. Also shown is an example of a waveguide consisting of rod-shaped Ag particles with an aspect ratio of 3:1 (bottom left) and a Ag nanowire (bottom right).

5.3 Far-field characterization of interparticle coupling in plasmon waveguides

In order to allow for an optical characterization with a high signal-to-noise ratio of the fabricated plasmon waveguides using far-field spectroscopy, we fabricated large area arrays in a 100 μm x 100 μm grid with a grating constant of 1 μm. Cross talk between adjacent structures is expected to have a negligible effect on the dispersion relation since it takes place via far-field scattering of the individual nanoparticles with a distance dependence of d^{-1}, whereas near-field interactions of adjacent particles in each waveguide show a d^{-3} dependence and dominate at small distances [17]. Moreover, the grating constant of 1.0 μm does not coincide with a grating order transition of increased far-field scattering [75], which further minimizes the far-field dipolar interactions. Thus, results from far-field spectroscopy on these arrays reflect the properties of individual plasmon waveguides. Our experimental setup consisted of a white halogen light source, a polarizer allowing for the selective excitation of the longitudinal or transverse modes and a computer-operated microspectrometer attached to an inverted optical microscope, which allowed for an easy localization of the plasmon waveguide structures.

The following discussion will center around the far-field optical characterization of plasmon waveguides consisting of up to 80 Au nanoparticles with diameters $D = 50$ nm and center-to-center particle spacings of 75, 100, and 125 nm, respectively. Figure 5-5 (upper left) shows a scanning electron micrograph of such plasmon waveguides resolving individual particles. The image was taken at normal incidence of the electron beam and confirmed a diameter of 50 nm ($R = 25$ nm) and a center-to-center spacing d of 75 nm ($3R$) of adjacent particles. Also, the grating constant of 1 μm between neighboring

structures was confirmed. Using atomic force microscopy, the height of the nanoparticles was determined to be 50 nm. The inset of Figure 5-5 shows a scanning electron micrograph of individual nanoparticles of the waveguide where the sample stage was tilted by 70 degrees in order to allow for a determination of the shape and aspect ratio of individual particles. We attribute the almost spherical shape of individual particles to room temperature annealing processes after the metallization and lift-off. The in-plane symmetry of the particles was confirmed by polarization spectroscopy on a regular grating of individual particles with a grating constant of 250 nm, showing only a small inherent single particle optical anisotropy (peak shift $2x10^{13}$ rad/s between longitudinal and the transverse modes).

Figure 5-6 shows a far-field extinction spectrum of plasmon waveguides with a 75 nm interparticle distance taken at normal incidence illumination with a spot size of 100 μm diameter for a polarization either in the direction of the waveguide axis (longitudinal polarization L) or perpendicular to it (transverse polarization T). Also shown is the extinction spectrum for illumination with unpolarized light (U). The extinction spectra show a dipolar plasmon peak for longitudinal and transverse illumination at angular frequencies of $E_L = 2.05$ eV and $E_T = 2.12$ eV, respectively, corresponding to wavelengths of maximal extinction of 604 and 585 nm. The extinction peak for unpolarized light lies between those two frequencies. The position of the dipole plasmon resonance is influenced both by the substrate and interparticle interactions [13], and this accounts for a shift of the resonance compared to single Au nanoparticles in air, which lies at 2.58 eV [13]. However, the polarization dependence of the peak positions indicates that near-field optical interactions are present between the nanoparticles

constituting the waveguide, which is consistent with theoretical work on electromagnetic interactions between closely spaced aggregates and chains of metal nanoparticles [67, 68].

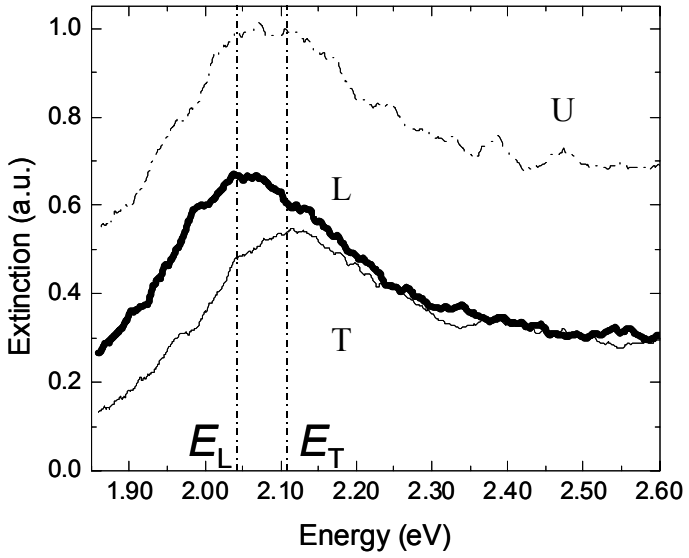

Figure 5-6: Far-field extinction spectrum of plasmon waveguides for both the longitudinal (thick line L) and the transverse (thin line T) mode of collective excitation. The peak positions for the L and T modes (marked with straight dashed lines) are located at different energies due to optical near-field interactions. Also shown is the extinction spectrum for unpolarized light (dotted line U).

The polarization dependence of the collective plasmon resonance of the plasmon waveguides can be understood from the point-dipole model presented in Chapter 3. The inset of Figure 5-7 shows the dispersion relation (frequency ω versus wave vector **k**) of guided modes in plasmon waveguides consisting of an infinite linear array of point dipoles spaced a distance $d << \lambda$ apart, the validity of which was confirmed in Chapter 4 using FDTD simulations. The solid lines show the dispersion relation assuming nearest-

neighbor coupling only, and the dotted lines take interactions between five nearest neighbors into account. The group velocity of the energy transport is given by the slope of the dispersion relation and has a maximum at a resonance energy E_0 of the waveguide. In Chapter 3, it was shown that E_0 corresponds to the surface plasmon resonance energy of a single particle and that particle chains can be excited most efficiently at this frequency using local excitation of single particles. In our experimental configuration all particles are excited in-phase, corresponding to $\mathbf{k} = 0$. In this case the group velocity is zero for both the longitudinal and the transverse branch and no transport of energy takes place. These collective modes occur at energies E_L for longitudinal and at E_T for transverse polarization. Both are shifted with respect to the energy E_0: The longitudinal mode is shifted to lower energies, and the transverse mode is shifted to higher energies, as seen in Figure 5-6. The ratio of the respective shifts is predicted to be 2:1 [17]. The extinction maxima in the far-field extinction spectra shown in Figure 5-6 directly yield values for E_L and E_T.

We fabricated plasmon waveguides with interparticle spacings of 75 nm ($3R$), 100 nm ($4R$) and 125 nm ($5R$) to study the influence of the interaction strength on the energy difference $\Delta E = E_T - E_L$. Polarization spectroscopy experiments as outlined above gave respective values E_L and E_T for these interparticle spacings. A plot of the position of E_L and E_T versus the interparticle spacing is shown in Figure 5-7.

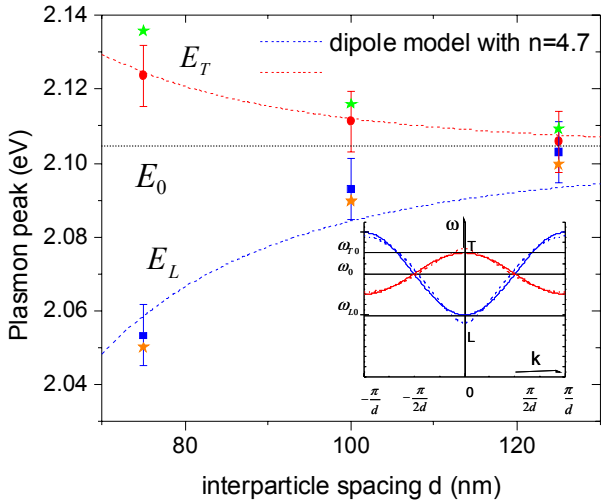

Figure 5-7 (color): Collective resonance energy of plasmon waveguides versus interparticle spacing. The plot shows the dependence of the plasmon peak energy on the interparticle spacing d for both the longitudinal (blue squares) and the transverse excitation (red circles) of the collective mode as obtained using far-field spectroscopy. The dotted red and blue lines show the $1/d^3$ dependence predicted by the point-dipole interaction model. The inset shows the dispersion relation of plasmon waveguides calculated using this point dipole model. Also shown are results from FDTD simulations (stars).

As can be seen, the energy difference ΔE of the $\mathbf{k} = 0$ modes is strongly dependent on the interparticle spacing, and drops below our experimental accuracy for an interparticle distance of $5R$ (the extinction peaks practically coincide ($E_L = E_T = E_0$)). The value of E_0 is deduced from the point of convergence of the extinction peaks. A fit of both curves for the longitudinal and the transverse mode shows a d^{-3} dependence of the position of the extinction peaks, which is consistent with the coupled point-dipole model for plasmon waveguides [17]. Also, the peak shifts of the longitudinal collective modes with respect to E_0 are larger than the shifts of the transverse collective modes as predicted by our dipole theory. For plasmon waveguides with individual nanoparticles spaced 75 nm apart, the ratio of the peak shifts is 2.3:1, close to the predicted value of 2:1. The difference is

attributed to particle interactions between next-nearest neighbors and the small inherent optical anisotropy of individual particles outlined above. The strong dependence of the peak shifts on interparticle spacing and the agreement with the dipole model of plasmon waveguides shows that the observed effects are indeed the result of near-field interactions between nanoparticles in plasmon waveguides. Figure 5-7 also shows the results of FDTD simulations of the sample geometry (stars). In order to model the presence of the glass substrate ($n = 1.5$) in the simulations, the medium surrounding the particles was taken to have an effective refractive index $n = 1.2$ for the transverse mode. The effective index for the longitudinal modes is slightly lower ($n = 1.15$) due to a stronger confinement of the optical near-field, which reduces particle-substrate interactions. Experiment and simulations are in good agreement. The good agreement of the experimentally probed $\mathbf{k} = 0$ points of the dispersion relation with predictions from the point-dipole model suggests that the model is indeed valid and that plasmon waveguides should allow for energy transport when locally excited in a mode with a finite wave vector $\mathbf{k}$ as outlined in section 4.3.

To determine the maximum group velocity of information transport in plasmon waveguides, the full dispersion relation for non-zero wave vectors $\mathbf{k}$ has to be known. This can be determined using the point-dipole model and the experimentally obtained energies E_L and E_T. We calculated the most efficient resonance energy for transport to be $E_0 = 2.105$ eV (590 nm) and a corresponding maximum group velocity $v_g = 4.0\text{x}10^6$ m/s for the longitudinal mode for plasmon waveguides with an interparticle distance of 75 nm. The bandwidth for this mode, which puts an upper limit to the rate of information transfer that can be achieved, was calculated to be 95 meV (23 THz). This is in good

agreement with point-dipole model calculations if the reduced interparticle coupling is taken into account.

Energy transport in plasmon waveguides relies on the excitation of modes with a finite wave vector $\mathbf{k} \neq 0$. The functional form $\omega(\mathbf{k})$, the group velocity and the energy propagation loss all depend on the number of directly interacting nanoparticles. In the remaining part of this chapter, this optical near-field interaction range is examined via far-field extinction measurements on arrays of short plasmon waveguides fabricated using electron beam lithography.

We fabricated multiple sets of samples consisting of Au nanoparticles with diameters $D = 50$ nm and center-to-center spacings $d = 75$ nm for chain lengths of 3, 5, and 7 particles using electron beam lithography on ITO coated glass slides. Extinction measurements as described above allowed for the determination of the collective plasmon resonance frequencies for both longitudinal and transverse modes. Figure 5-8 shows the energies $E_{L,T}$ of the collective modes for plasmon waveguides with 1, 3, 5, 7 and 80 particles for both L and T polarizations as obtained by far-field experiments (circles). The peak splitting ΔE between the longitudinal and the transverse modes increases with particle chain length and saturates at $\Delta E = 65$ meV for about 7 particles. The observed trend in $E_{L,T}$ is in qualitative agreement with Mie-theory calculations for silver nanoparticle chains in air [67]. Figure 5-8 also shows the results of FDTD simulations (stars) using the effective surrounding medium approach outlined above. Experiment and simulations are in good agreement. Note that whereas the point-dipole model of plasmon waveguides predicts that nearest-neighbor interactions dominate in plasmon waveguides, the increase in peak splitting between particle chains with 3 and 5 particles suggests that

also second nearest-neighbor interactions need to be taken into account to correctly describe the waveguide properties.

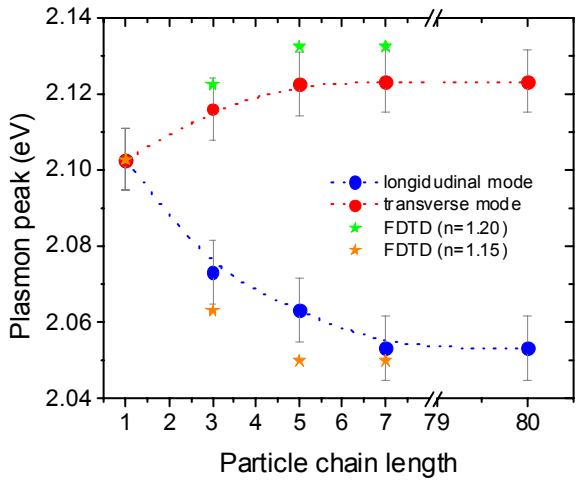

Figure 5-8 (color): Collective resonance energy of plasmon waveguides versus particle chain length. The plot shows the dependence of the plasmon peak position on the particle chain length for both longitudinal (blue circles) and transverse excitation (red circles) of the collective mode as obtained using far-field spectroscopy. Also shown are results from FDTD simulations (stars).

As discussed above, the peak splitting ΔE is a direct measurement of the particle interaction strength, which in turn determines the bandwidth $B_{L,T} = 2\left|E_{L,T} - E_0\right|$ available for transport for L and T modes. In our case, $B_L = 95$ meV (23 THz) for the longitudinal mode. As pointed out, the interaction strength also puts an upper limit to the group velocity $v_{gL,T}$ for energy transport, and this together with the resistive damping of the oscillation determines the minimum energy loss of propagating waves in plasmon waveguides. The plasmon wave attenuation coefficient $\alpha_{L,T}$, which describes the exponential attenuation of the electric field of the propagating plasmon wave, is given by

$\alpha_{L,T} = \Gamma / 2v_{gL,T}$, with Γ being the homogeneous linewidth of the plasmon dipole resonance. Using simple algebraic manipulations outlined in section 3.2, it follows that at the point $\mathbf{k} = \pi / 2d$ of maximum group velocity the attenuation coefficient $\alpha_{L,T} \times d = \Gamma / B_{L,T}$. This quantity can be calculated using quantities obtained from far-field measurements alone. In the case of 50 nm Au spheres, Γ = 180 meV, as obtained directly from the far-field measurements and confirmed using near-field spectroscopy as described in section 6.3, corresponding to a decay time τ of 3.6 fs close to the decay time of single Au nanospheres on TiO_2 [15]. We thus obtain $\alpha_L \approx 2.5\text{x}10^7\ \text{m}^{-1}$ for the fabricated structures with an interparticle spacing $d = 3R$, corresponding to an energy loss $2\alpha_L$ of about 6dB/30nm, showing that the current geometry cannot produce long range energy transfer for the selected materials.

5.4 Conclusion and outlook: Decrease of waveguide loss by particle design

Far-field optical spectroscopy allows for the investigation of the interparticle coupling strength in plasmon waveguides via the determination of the collective plasmon resonance energies of the longitudinal and transverse $\mathbf{k} = 0$ modes of the dispersion relation. For plasmon waveguides consisting of 50 nm Au particles fabricated using electron beam lithography on ITO coated quartz substrates, the interparticle coupling is reduced due to substrate polarization effects, and the far-field analysis suggests a large energy attenuation on the order of 6dB/30nm.

In order to allow for the application of plasmon waveguides in integrated optical circuits, the attenuation losses must be decreased. This can be achieved either via a reduction of the homogeneous linewidth Γ of the plasmon oscillation or via an increase of the interparticle coupling to increase ΔE and thus the group velocity v_g. Both goals can be achieved via a change to materials with a longer electron relaxation time τ such as Ag or a change in particle shape. For Au nanoparticles, it has recently been shown that Au nanorods with aspect ratios of 3:1 show a decrease in homogeneous linewidth by a factor 2.25 due to a resonance shift away from the interband transition edge [69]. To illustrate the effect of changing the particle shape, Figure 5-9 b shows FDTD simulation results (blue diamonds) for the transverse collective mode of an array of nanorods approximated with spheroids with their long axis perpendicular to the waveguide chain axis as described in section 4.4 for the same particle volume and center-to-center spacing as in the nanosphere case. The results show a maximum bandwidth $B_T = 360$ meV for the transverse mode, which is indeed larger than in the nanosphere case graphed for comparison in Figure 5-9 a. Assuming that the dispersion relation predicted by the point-dipole model still holds, the corresponding attenuation coefficient is $\alpha = 2.7\text{x}10^6$ m^{-1} and the energy loss 6 dB/260 nm, a factor ~9 less than in the nanosphere case. As the results of FDTD simulations of plasmon waveguides consisting of spheroidal particles in section 4.4 have shown, such waveguides indeed show higher group velocities and thus increased attenuation lengths compared to waveguides consisting of spherical particles, but not to the extent that the point-dipole model suggests. This is due to a change in the dispersion properties as explained in the discussion around Figure 4-10. The stated energy attenuation length of 6dB/260nm is thus an upper estimate of the attenuation length.

Since in our FDTD simulations the dielectric response of metals is modeled using a Drude type dielectric function and does thus not include interband processes, there is no pronounced difference between plasmon bandwidths obtained for Ag and Au particles.

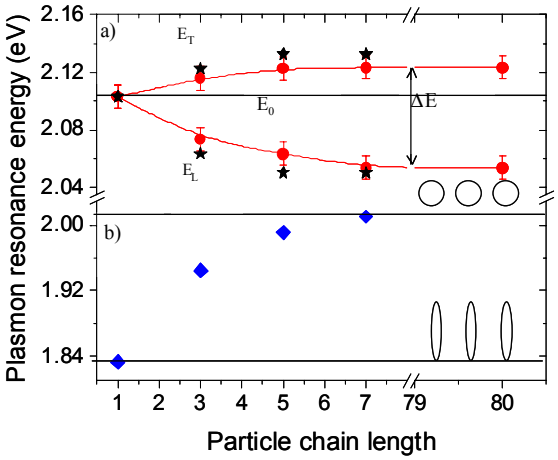

Figure 5-9 (color): Collective resonance energies of chains of spherical and spheroidal particles. a) Collective plasmon resonance energies for both longitudinal (E_L) and transverse (E_T) excitations for Au nanoparticle arrays of different lengths obtained via far-field spectroscopy (red circles) and finite-difference time-domain simulations (black stars). b) Simulation results for the collective plasmon resonance energies for transverse excitation of Au spheroids with aspect ratios 3:1 (blue diamonds)

Figure 5-10 (thick line) shows a far-field extinction spectrum for plasmon waveguides consisting of rod-shaped Ag particles with an aspect ratio of 3:1, corresponding to particle dimensions of 90 nm x 30 nm x 30 nm as shown in the inset. The surface spacing between adjacent nanorods is 50 nm, which is the closest inter-rod spacing achieved in our electron beam lithography setup, resulting in a center-to-center spacing of 80 nm. Figure 5-10 also shows a far-field extinction spectrum with the rod-shaped particles arranged in a grid with a grating constant 1 μm (thin line), corresponding to the long-axis plasmon mode of single particles. As can be seen, the transverse

extinction peak is blue-shifted for the particle arrays compared to the single particles, yielding a bandwidth $B_T = 340$ meV for the transverse collective mode, in good agreement with the FDTD results presented above.

In summary, rod-shaped nanoparticles enable the fabrication of plasmon waveguides with an increased interparticle coupling. This is expected to result in increased group velocities and energy attenuation lengths for energy transport. Further optimization of waveguide geometry and material is expected to allow for energy propagation over several hundred nanometers.

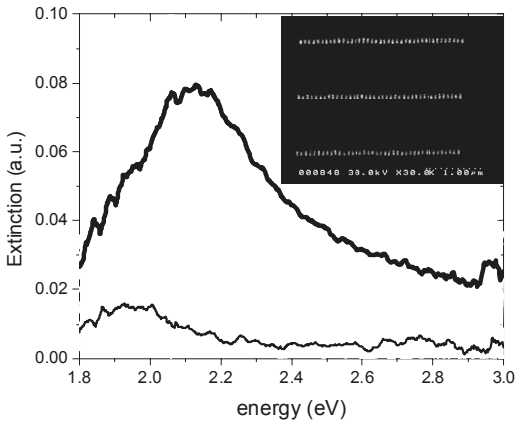

Figure 5-10: Far-field extinction of rod shaped particles. The plot shows far-field extinction spectra of plasmon waveguides consisting of rod-shaped Ag particles with a 3:1 aspect ratio for the transverse mode of excitation (thick line) and for single nanoparticles (thin line).

Chapter 6 Local excitation of plasmon waveguides

6.1 Introduction

In the preceding chapter, far-field spectroscopy allowed for the investigation of interparticle coupling in plasmon waveguides and for an estimation of the group velocity and energy attenuation length for energy transport in conjunction with the theory presented in Chapter 3 and Chapter 4. However, as pointed out far-field spectroscopy only allows for the in-phase excitation of the long-wavelength $\mathbf{k} = 0$ modes of the dispersion relation (Figure 6-1 dotted circles). Since $\mathrm{d}\omega/\mathrm{d}\mathbf{k}$ and thus the group velocity is zero for these modes, no energy can be transported in plasmon waveguides excited by broad-beam illumination [64]. A direct observation of energy transport requires the excitation of a finite $\mathbf{k} \neq 0$ mode such as the $\mathbf{k} = \pi/2d$ mode of maximum group velocity (Figure 6-1 solid circle). Thus, a local excitation source of plasmon waveguides is required.

In recent years, the emerging field of near-field scanning optical microscopy has revolutionized the investigation of localized electromagnetic fields such as evanescent, non-propagating electromagnetic waves and the analysis of local optical properties of materials below the diffraction limit [76]. Thus, a near-field scanning optical microscope (NSOM) [77] was chosen as the tool of choice for localized excitation and analysis of plasmon waveguides.

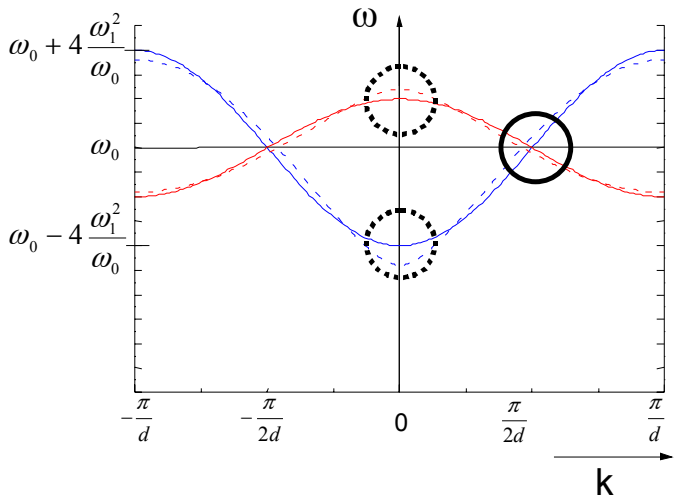

Figure 6-1 (color): Dispersion relation of a plasmon waveguide consisting of spherical nanoparticles. Only the long-wavelength modes with zero group velocity (marked by dotted circles) can be probed using far-field excitation. Excitation of a finite wave vector mode such as the mode of maximum group velocity (marked by solid circle) requires local excitation of the waveguide.

The investigation of light-matter interactions occurring on the nanoscale below the diffraction limit of light requires the probing and manipulation of evanescent fields. The first manipulation of an evanescent electromagnetic field goes as far back as Newton in the form of the optical tunneling effect, depicted in its modern form in Figure 6-2. In this case, an evanescent field is created above a prism by total internal reflection of a light beam. This field can be converted into propagating electromagnetic waves by placing a second prism a distance $d < \lambda$ into the near-field of the first prism. Since evanescent fields contain high wave vector components, the propagation of which into the far-field is forbidden, the conversion of evanescent fields into propagating fields is necessary for the study of optical interactions below the diffraction limit.

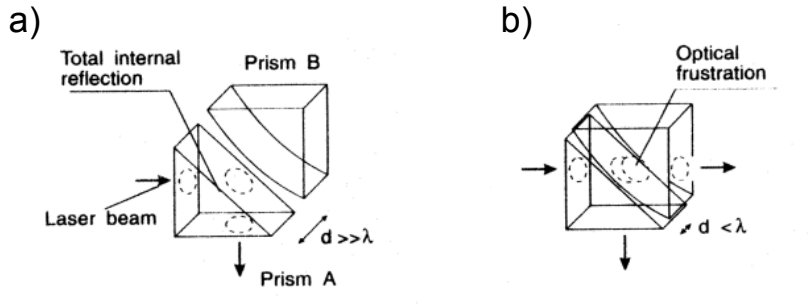

Figure 6-2: The optical tunneling effect. a) A laser beam is reflected by 90 degrees due to total internal reflection at the slanted side of prism A, resulting in an evanescently decaying field perpendicular to the slanted side. b) A second prism B placed at a distance $d<\lambda$ to prism A frustrates total internal reflection by converting the evanescent field into propagating electromagnetic waves. After [77].

While in the optical tunneling effect this is accomplished via the placement of a second prism in the near-field of the first, in near-field optical microscopy a local nanoscopic probe akin to the tip of an atomic force microscope is used for this purpose. In a so-called apertureless NSOM [78], the probe itself is optically opaque, serving as a mere perturbation of the evanescent near-fields under study, and both optical excitation and detection are employed using simple diffraction-limited Gaussian beams. While apertureless NSOMs often show superior optical resolution, for our purpose a localized excitation source is necessary, requiring an aperture-type NSOM as depicted in Figure 6-3. Building on the theory of diffraction by small holes with a subwavelength diameter [79-81], in an aperture-type NSOM the localized probe itself consists of a metal or dielectric probe with an optically transparent part at the apex, enabling local illumination with light fields (illumination mode, Figure 6-3 b) or local collection of evanescent light fields (Figure 6-3 a and d). In illumination mode, the tip of an aperture-type NSOM effectively serves as a localized light source, enabling near-field spectroscopy and photoluminescence studies with collection in the far-field [82-85]. Theoretical studies

have further shown that the near-field excitation process can be viewed as a special example of a dipole-dipole energy transfer [86].

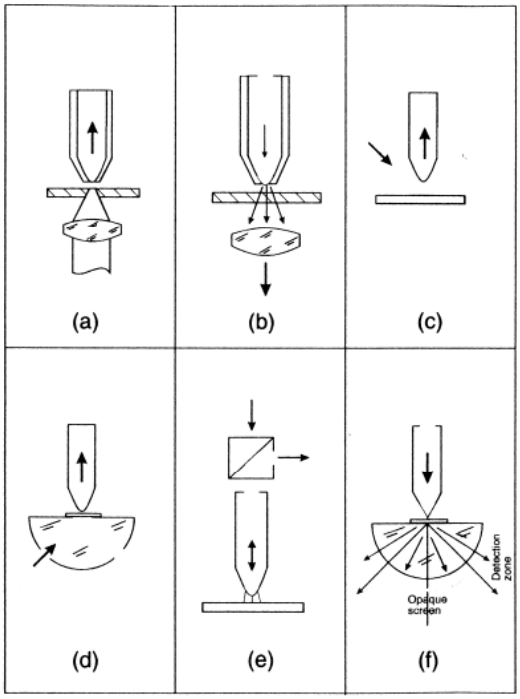

Figure 6-3: Aperture-type NSOM geometries such as transmission collection (a), transmission illumination (b) and total internal reflection collection mode (d). After [77].

In addition to near-field optical investigations and spectroscopic studies of a variety of systems, near-field optical microscopes have also enabled the localized study of the properties and propagation of surface plasmons both in metal films [87, 88] and nanoparticles [89]. In addition, powerful theoretical tools such as the Green dyadic technique have been developed to analyze the optical near-fields of the tip-substrate system [90] and energy propagation in nanowires [91].

In this chapter, an experimental study of plasmon waveguides using an aperture-type illumination-mode NSOM will be presented. The NSOM tip is used as a localized light source to excite finite $\mathbf{k} \neq 0$ wave vector modes for energy propagation, and experimental evidence for subwavelength scale energy transport is presented.

6.2 Transmission NSOM analysis of plasmon waveguides: Facts and artifacts

Our NSOM system builds on a Nanonics NSOM-100 scanhead [92, 93] consisting of a piezoelectric flatbed scanner and a head plate incorporating a diode laser and a photodetector for the monitoring of the tip motion. The scanhead is placed on the stage of a conventional inverted optical microscope (Figure 6-4). This way, the sample under study placed on the flatbed scanner can easily be examined, and the light scattered by the sample in NSOM illumination mode can be collected using an objective with a large working distance for analysis.

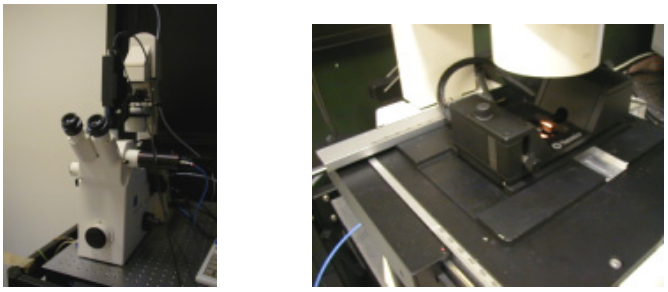

Figure 6-4 (color): The Nanonics NSOM-100 scanning head, integrated into a conventional inverted optical microscope system.

Figure 6-5 shows a picture of a typical Nanonics NSOM tip used in our experiments. The tip is drawn from a conventional optical fiber that is tapered down and bent at an angle to enable a normal force type AFM feedback control where light emanating from the diode laser incorporated in the head plate is reflected from the cantilever and monitored with the photodiode. This way, sample topography information can be collected both in contact and non-contact mode together with the optical image as the sample is scanned underneath the tip. In contact mode, the deflection of the otherwise stationary cantilever is used as the feedback signal, while in non-contact mode changes of the amplitude of the oscillating tip caused by topography-dependent shifts in the resonance frequency of the tip-sample system are employed for the same purpose. During scanning, the feedback loop ensures that the gap between the tip and the sample is held constant using the z-motion of the flatbed scanner (constant gap mode).

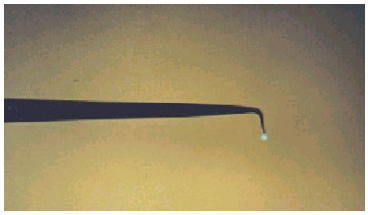

Figure 6-5 (color): Nanonics NSOM tip drawn from a conventional optical fiber that has been tapered down and bent to enable an AFM-type normal force feedback. The light emanating from the aperture in illumination mode can be seen (courtesy of Nanonics Imaging Ltd).

During the tip production process, the end part of the optical fiber is coated with a thin aluminum coating, and a small aperture at the end of the bent tip is created. In our experiments, we typically used NSOM tips with a 100 nm aperture fabricated using

multi-mode optical fibers with a 50 μm core diameter to ensure a large optical transmission through the aperture in illumination mode.

The investigation of the electron beam fabricated plasmon waveguides with our NSOM system requires the use of non-contact mode feedback for scanning. This way, tip-sample interactions can be minimized. Figure 6-6 shows the results of a contact mode scan of plasmon waveguides consisting of spherical nanoparticles. The large tip-sample interactions led to a complete destruction of the scanned area (a). A scanning electron microscope analysis of the tip after scanning revealed that the tip had picked up some of the particles from the substrate (b).

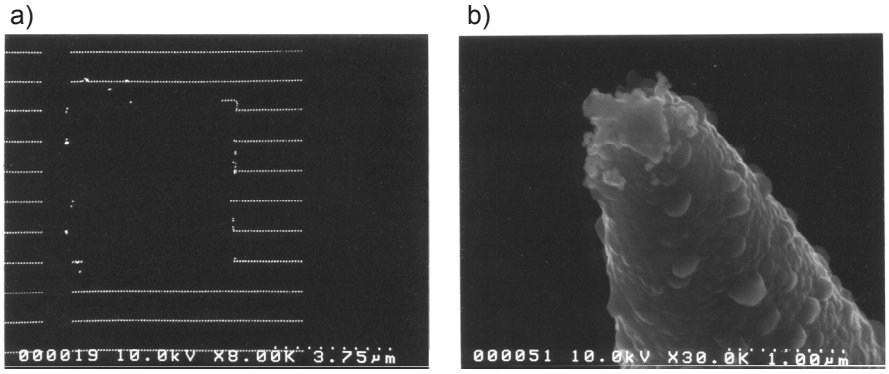

Figure 6-6: Fragility of plasmon waveguides prevents contact mode scanning. a) Scanning electron micrograph of nanoparticle plasmon waveguide structures after a contact mode NSOM scan. The particles have been swept aside by the tip. b) Scanning electron micrograph of the tip used. The aperture is blocked by nanoparticles that have been picked up during the sweeping. Some of the particles apparently fused.

Figure 6-7 shows both the topography (a) and transmitted light image (b) of a NSOM scan of plasmon waveguide structures consisting of 50 nm spherical Au particles with a center-to-center spacing of 75 nm obtained using a 100 nm aperture NSOM tip. Laser light from an Argon-pumped dye laser at the surface plasmon resonance frequency of

590 nm was coupled into the fiber tip for a local excitation of the sample. The topography image clearly shows single nanoparticles despite tip convolution effects. Compared to the topography image, the transmitted light image (b) is far more complex and shows a wealth of interesting features.

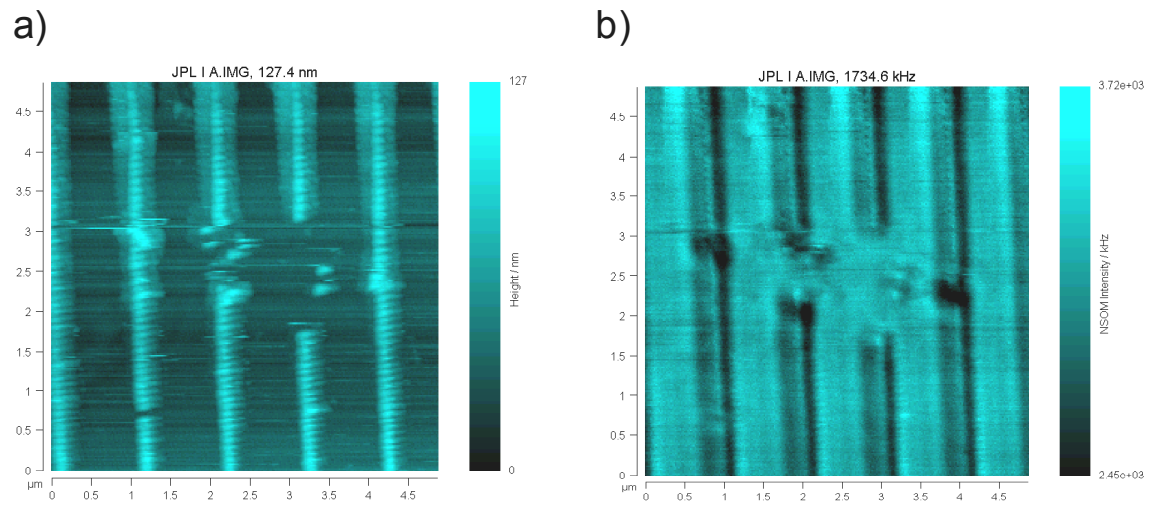

Figure 6-7 (color): Topography (a) and transmitted light (b) NSOM image of plasmon waveguides consisting of spherical Au nanoparticles. During scanning, the sample was locally illuminated at 590 nm with a 100 nm aperture tip.

For each plasmon waveguide, at least three features can be distinguished in the upper part of Figure 6-7 b: a dark straight line, single black dots, and a bright line. While the dark straight lines were seen to be the typical feature of all transmission NSOM scans of plasmon waveguides for closely spaced nanoparticles, the black dots and the bright lines did not occur in all images. The emergence of a dark line can be attributed to a shadowing effect of the nanoparticle structure. Part of the light emanating from the tip is blocked by the particle structure, resulting in decreased transmission into the far-field. Theoretical studies of the tip-nanoparticle system support this interpretation [94, 95]. The

fact that our scan shows a straight line instead of single nanoparticles can be explained by the poor optical resolution of the system that prohibits the detection of single closely spaced nanoparticles. On the other hand, the dark black dots next to the straight dark line in the upper part of Figure 6-7 b can be interpreted as shadows of single particles. This degree of optical resolution is extraordinary, since the nanoparticles constituting the waveguides show a surface-to-surface spacing of only 25 nm. This superior optical resolution could be due to a local nanometer-sized scattering center in the vicinity of the tip aperture which fell off the tip during the scan, explaining the lack of single particle optical resolution in the lower part of the image.

While the dark features are direct optical signatures of the Au nanoparticles, the straight bright lines are signs of topography artifacts induced by the sample motion. Such height-induced artifacts are typical for constant-gap NSOM systems [96-99] and do not show in constant-height images. These artifacts can usually be detected by their rigorous spatial overlap with the topography image. In contrast, purely optical features are usually slightly displaced from the topography structures due to the fact that topography images usually occur at the point of largest protrusion of the tip which does not coincide with the center of the aperture. Figure 6-8 shows a clear example of this effect for an NSOM scan of solid 50 nm Au nanowires in the form of a three-dimensional surface plot. The topography of the plot reflects the sample topography, and the transmitted NSOM image is encoded in the color of the surface. The dark optical signatures of the nanowires are seen to be displaced from the topography protrusions, in agreement to the qualitative theory outlined above.

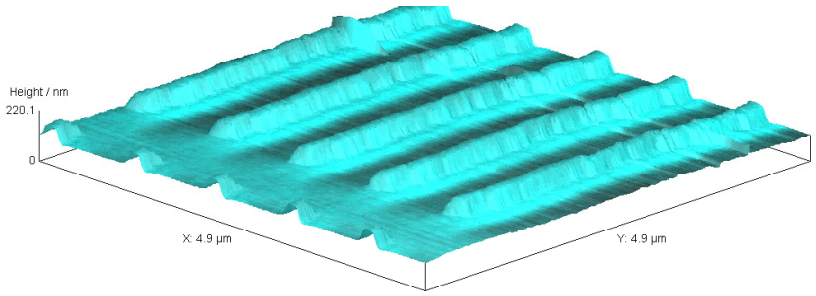

Figure 6-8 (color): Topography and transmitted NSOM image of solid Au nanowires combined into a three-dimensional surface plot. The topography represents the height information, and the color scale the optical transmission. The optical shadow of the transmitted light image is slightly displaced to the topography image.

The last point in the discussion of transmission NSOM scans of metal nanoparticle plasmon waveguide structures concerns the dependence of the optical image on the wavelength of the exciting light. As noted in the preceding discussion, in a usual transmission NSOM scan nanoparticle arrays appear as dark areas of decreased transmission due to absorption and shadowing. In fact, it was shown both theoretically and experimentally that the detailed structure of the transmission NSOM image for Au nanoparticles is mainly influenced by the thickness of the metal coating of the tip used for scanning [94, 95]. It is therefore difficult to see wavelength dependent effects on the optical transmission and thus signs of a plasmon-enhanced absorption for excitation at the plasmon resonance frequency of the particles. In fact, transmission scans of Au plasmon waveguide structures similar to the one discussed above did not show a discernable dependence on the wavelength of the exciting light. This could partly also be due to the fact that single particle optical resolution was not achieved in most scans. Nevertheless, in the scan that achieved single particle optical resolution depicted in Figure 6-7 b, bright, dot-like areas are seen to surround some of the dark single nanoparticle images. This

could be due to a field enhancement effect in the vicinity of the nanoparticles caused by the excitation of the plasmon resonance. Similar observations of a "bright halo" surrounding metal nanoparticles excited at the plasmon resonance have recently been reported [82].

In summary, transmission NSOM scans of metal nanoparticle plasmon waveguide structures show decreased transmission compared to scans of the ITO glass substrate. Due to tip convolution and the complicated optical interaction between the metal-coated tip and the nanoparticles, wavelength dependent effects on the optical transmission spectra cannot easily be verified. While typical optical resolutions are in the range of a couple of 100 nm, in one case an optical resolution of < 25 nm has been achieved.

6.3 Molecular fluorescence as a probe for localized electromagnetic fields

As described in the previous section, the tip of an illumination-mode NSOM can be used as a localized excitation source of nanoparticles in plasmon waveguide structures. In addition, a local detector that is sensitive to electromagnetic fields is necessary in order to obtain experimental evidence for energy transport from the excitation source along the waveguide. We used fluorescent molecules that can be excited at frequencies around the surface plasmon frequency of the nanoparticles constituting the waveguides for this purpose.

The effects of localized electromagnetic fields occurring at surfaces on the spectroscopic properties of molecules have been under intense investigation for the last decades, both from a fundamental point of view and for applications such as surface

enhanced Raman spectroscopy [100]. More recently, the effects of electromagnetic near-fields on molecular fluorescence have been under study, and thin films of fluorescent molecules have been used to determine the influence of nanoscopic probe tips on the fluorescence yield [101]. While fluorescent molecules usually show a quenching of the total fluorescence in the vicinity of metal surfaces due to non-radiative transitions, it has been shown that the field enhancement due to surface plasmons can reduce this quenching [102] and in fact lead to a net increase in fluorescence for certain distances between the molecule and the metal surface [103]. This effect has been employed in the study of the spatial profile of propagating surface plasmons on a metal film coated with a thin layer of fluorescent molecules [104, 105].

For an application of fluorescent molecules as detectors for transport of electromagnetic energy in plasmon waveguides, a placement of the molecules at specific positions in the vicinity of a plasmon waveguide is desirable. For this purpose, fluorescent polystyrene spheres with a diameter of 100 nm were used. These nanospheres are commercially available with a number of fluorescent dyes covering the visible and near-infrared range of the electromagnetic spectrum. It has recently been shown that such dyes can be excited with the tip of an illumination-mode NSOM and the fluorescence be collected in the far-field [106], and fluorescent nanospheres have allowed for the topographical and optical characterization of NSOM tips [107].

Figure 6-9 shows a far-field spectrum of a thin film of aggregated nile-red fluorescent nanospheres excited with an Argon laser at 514 nm. The power of the exciting laser light was 50 μW and the spot size around 1 mm. The exciting laser light was blocked with a 520 nm long pass filter in the detection path of the photoluminescence setup. This way, a

clear fluorescence spectrum peaking around 610 nm was obtained. Significant bleaching of the fluorescence on a time scale of minutes occurred for the laser power and spot size used.

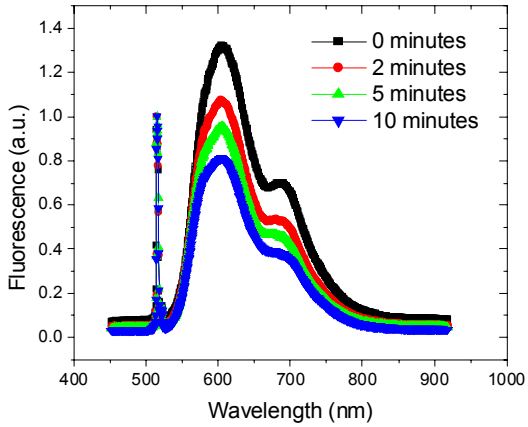

Figure 6-9 (color): Far-field spectrum of the fluorescence of a thin film of aggregated nile-red fluorescent nanospheres obtained using a photoluminescence setup. The spheres were excited using the 514 nm line of an Argon laser, and the fluorescence was collected between 520 and 930 nm. Significant fluorescent bleaching occurs for far-field excitation.

In order to investigate the nanosphere fluorescence using the tip of our NSOM as the excitation source, the setup was modified with a variety of filters in the far-field detection path as depicted in Figure 6-10 to allow for the blocking of the exciting laser light and fluorescent detection. Additionally, for nanospheres fluorescing above 620 nm, the red laser of the NSOM topography-feedback system was additionally exchanged for an infrared laser emitting at 908 nm.

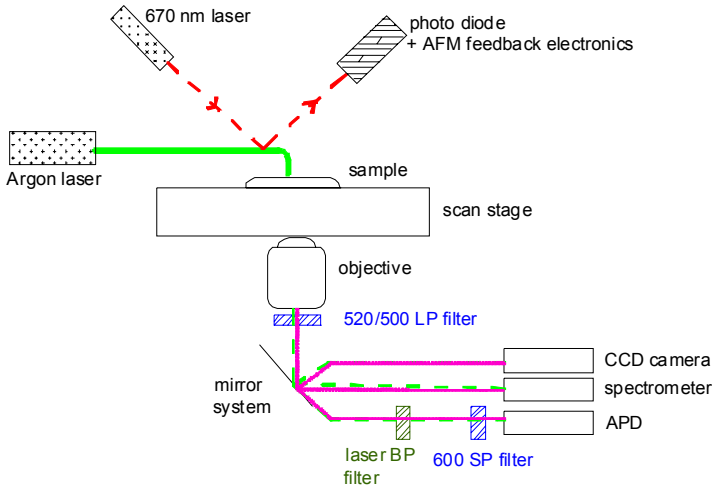

Figure 6-10 (color): Fluorescent NSOM setup. Using a variety of filters in the far-field detection path, the exciting laser light can be blocked and the fluorescence of the sample under study collected and analyzed using a CCD camera, spectrometer or an avalanche photo diode.

Figure 6-11 shows both the topography (a) and the fluorescence NSOM image (b) for a sample consisting of 100 nm nile-red fluorescent nanospheres randomly deposited on a glass slide coated with a sticky poly-lysine layer. Despite considerable tip convolution effects visible in the topography image (a), single-particle resolution is achieved in both the topography and fluorescent NSOM channel. The optical image (b) shows the fluorescence of single particles for three different excitation powers expressed as the number of photons emanating from the tip measured by an avalanche photo diode without blocking the excitation beam in the detection path. Excitation powers around 40 MHz are necessary for good signal-to-noise ratios. For these excitation powers, the typical dye peak fluorescence was found to be about a factor five to ten above the electric dark noise of the avalanche photo diode. Note that high excitation powers > 10 MHz are already close to the damaging threshold of the metal-coated NSOM tips. The efficient excitation of fluorescent nanospheres requires thus excitation powers close to the limit of

our NSOM system. Similar power requirements were found for nanospheres fluorescing in different parts of the visible regime of the electromagnetic spectrum.

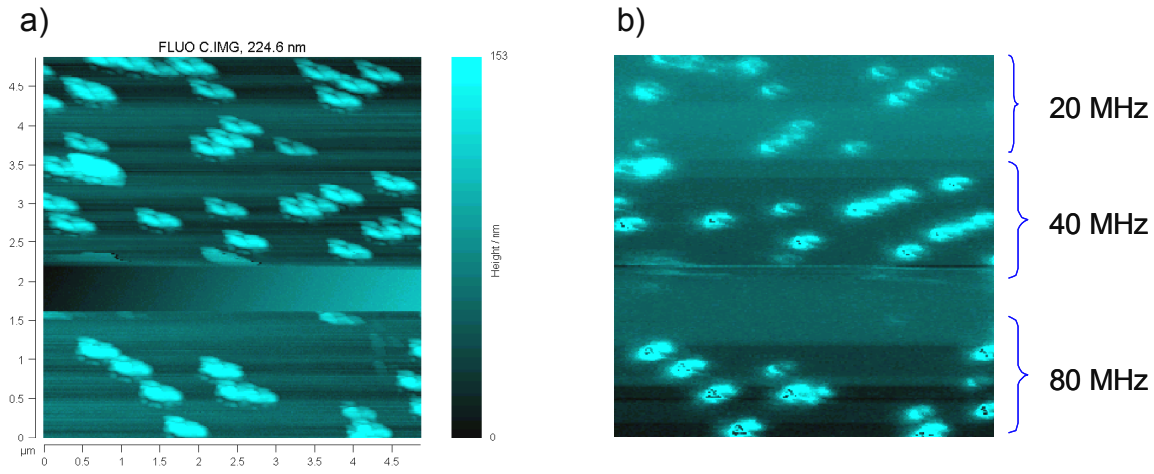

Figure 6-11 (color): Topography (a) and fluorescent NSOM image (b) of 100 nm polystyrene nanospheres deposited on a poly-lysine-coated glass slide. The fluorescence image shows the dye intensity for different excitation counts of 20, 40 and 80 MHz as measured on an avalanche photo diode.

The topography and the fluorescent NSOM image of the fluorescent nanospheres typically show different resolutions due to tip geometry effects. Figure 6-12 a shows an additional example of a topography scan of the nile-red nanospheres discussed above. Due to tip-convolution effects in the topography channel, the lateral width of a single 100 nm sphere is about 500 nm, while the optical width displayed in the fluorescent NSOM image of Figure 6-12 b is on the order of 250 nm. For typical NSOM tips with an aperture of 100 nm, the full width at half maximum of a single fluorescent sphere is on the order of 200-400 nm. Contrary to far-field excitations of the fluorescent nanospheres described above, no significant bleaching of the spheres occurred during successive NSOM scans of the same area, despite the fact that each scan took about 1 h to complete.

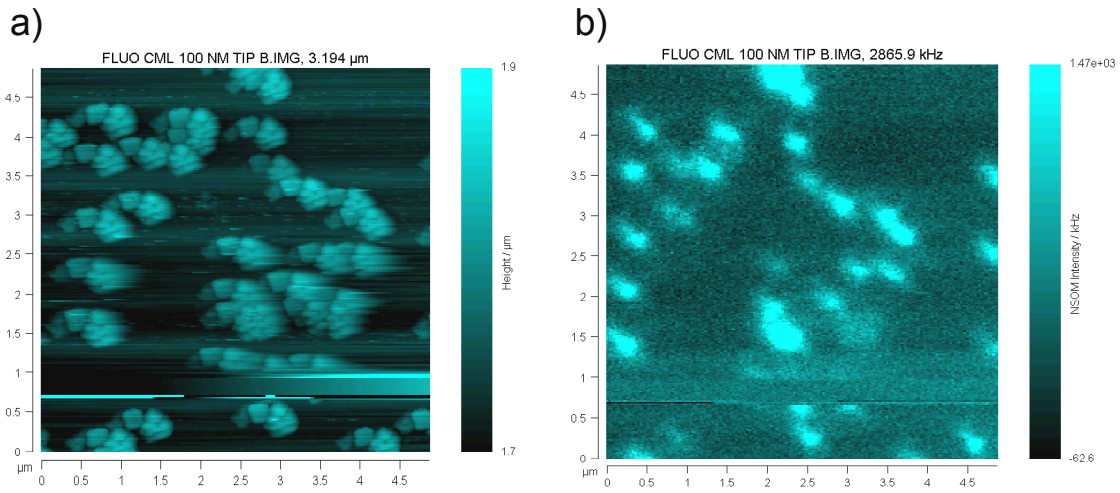

Figure 6-12 (color): Topography (a) and fluorescent NSOM scan (b) of 100 nm fluorescent nile-red nanospheres. The topography and optical resolution are clearly different due to tip-convolution effects.

The fluorescent spheres described above can be used as local probes for the electromagnetic field around the metal nanoparticles constituting plasmon waveguides. This way, the plasmon resonance frequency and decay time can be determined in a near-field spectroscopy experiment using the dye fluorescence as an indicator of the electromagnetic field enhancement around the metal nanoparticle structures as the excitation frequency is varied in the vicinity of the plasmon resonance.

Figure 6-13 a shows a schematic of this near-field fluorescence spectroscopy experiment. The NSOM tip is used as a local excitation source to probe the properties of the nanoparticles constituting the plasmon waveguides. An excitation laser frequency in the vicinity of the single particle dipole resonance leads to the build-up of an enhanced electromagnetic field proportional to the plasmon decay time [15] around the particle structure. This local field is probed via fluorescent molecules attached to the tip, and the

radiation of these molecules is detected in the far-field. The fluorescent molecules chosen show a constant absorption in the vicinity of the dipole resonance frequency. The emitted intensity of fluorescent radiation is thus a direct measurement of the local field [103]. Figure 6-13 b shows the enhancement of the fluorescent intensity as the excitation frequency is scanned through the dipole resonance frequency for plasmon waveguides consisting of spherical Au particles. The obtained intensity data can be fitted with a Lorentz line shape with a full width at half maximum of about 180 meV, corresponding to a decay time of 3.6 fs, which is in close agreement with measurements of the homogeneous linewidth for single Au nanoparticles on a TiO_2 substrate [15].

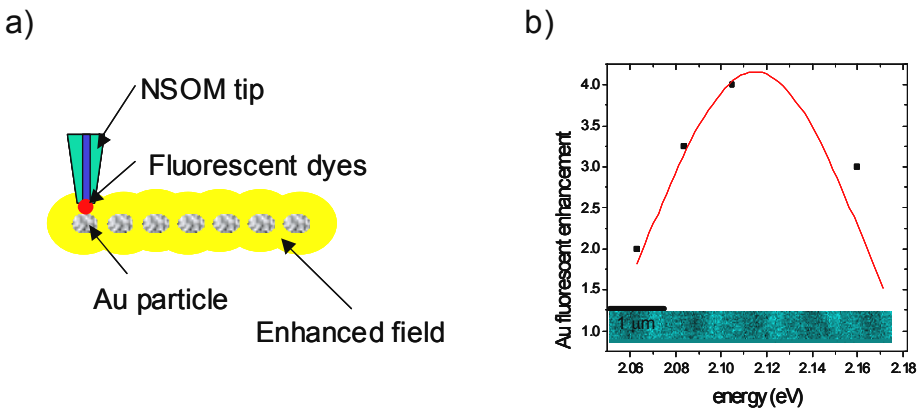

Figure 6-13 (color): Fluorescence near-field spectroscopy of plasmon waveguides. a) The Au nanoparticles are excited with the tip of a scanning near-field optical microscope (NSOM) in the vicinity of their plasmon resonance. The enhanced field around the particles is probed via fluorescent molecules attached to the NSOM tip. b) Fluorescence intensity versus excitation energy of the laser light, showing the homogenous line shape of the plasmon resonance. The inset shows the fluorescent intensity variation in a scan over 4 plasmon waveguides spaced 1 micron apart.

In summary, fluorescent nanospheres can be used as a tool for the local probing of electromagnetic fields in the vicinity of plasmon waveguide structures. In the next

section, the spheres are employed as local probes for the detection of energy transport in a locally excited plasmon waveguide.

6.4 Local excitation and detection of energy transport in plasmon waveguides

The plasmon waveguides used in this analysis of energy transport consist of rod-shaped Ag nanoparticles with dimensions of 90 nm x 30 nm x 30 nm and a surface-to-surface spacing of 50 nm between adjacent particles. The long axes of the individual nanoparticles were oriented perpendicular to the waveguide chain axis in order to allow for an increased near-field coupling between the particles as described in section 5.4. The structures were fabricated using electron beam lithography with lift-off on ITO coated quartz slides, which allowed for a good control over particle size and spacing. The inset of Figure 6-14 shows a scanning electron micrograph of a plasmon waveguide of this geometry. In order to determine the plasmon resonances of the fabricated structures with a high signal-to-noise ratio using far-field spectroscopy, a large number of plasmon waveguides were arranged in a 100 μm x 100 μm grid with a grating constant of 1 μm as depicted in Figure 6-15 b. As described in section 5.3, cross talk between different waveguides is negligible for this grating constant. This way, far-field extinction spectra on these arrays probe the near-field coupling between the nanoparticles comprising each waveguide only and reflect thus the properties of individual plasmon waveguides.

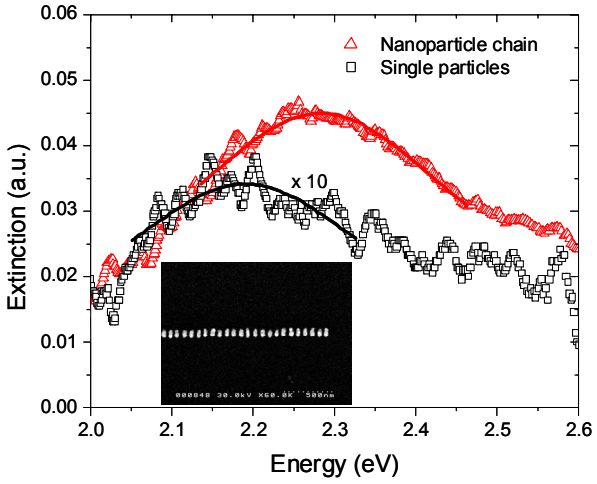

Figure 6-14 (color): Far-field extinction spectrum of Ag nanoparticle chains and single particles. The far-field extinction spectrum of a plasmon waveguide consisting of Ag nanorods with a 3:1 aspect ratio and a surface-to-surface spacing of 50 nm between adjacent particles shows a plasmon resonance peak shift to higher energies (red triangles and Lorentz fit) compared to the extinction spectrum of isolated, non-interacting particles (black squares and Lorentz fit). The exciting light was polarized along the long axis of the nanorods, perpendicular to the particle chain axis. The inset shows an SEM micrograph of the plasmon waveguide under study.

Figure 6-14 shows the far-field extinction spectrum of the fabricated plasmon waveguides taken under normal incidence white light illumination with a spot size of 100 μm and a polarization along the long axis of the nanoparticles and thus perpendicular to the waveguide chain axis (red data points). Also shown is the extinction spectrum of a grid of single Ag nanoparticles of the same geometry with an interparticle spacing of 1 μm, for which the interparticle coupling is negligible (black data points). The single particle extinction spectrum peaks at 2.18 eV for a polarization along the long particle axis, corresponding to a resonance wavelength of 570 nm. The extinction spectrum of the plasmon waveguide shows a resonance shift of about 100 meV to higher energies due to near-field coupling between the particles, in agreement with the numerical simulations

presented in section 4.4. According to these simulations, a resonance shift of 100 meV should translate into a maximum energy attenuation length on the order of 6 dB/200 nm for an excitation at the single particle resonance at 2.18 eV, at which the energy transfer in a plasmon waveguide is most efficient.

In order to directly observe signs of energy transport in the fabricated plasmon waveguides, a local excitation of a non-zero wave vector **k** is necessary as opposed to an in-phase excitation of the particle arrays as a whole at **k** = 0 using far-field illumination. To accomplish this, the tip of an illumination mode near-field optical microscope (Nanonics NSOM-100) was used as a local excitation source for nanoparticles in plasmon waveguides. Light from a dye laser at a wavelength of 570 nm, corresponding to the single particle resonance, was used in order to excite the mode of least damping. The light was coupled into a multimode optical fiber attached to the Al-coated NSOM tip used for excitation. Figure 6-15 a shows a schematic of our principle of excitation and energy transport detection.

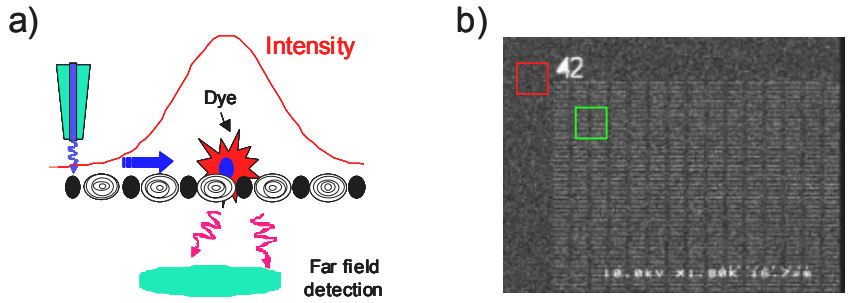

Figure 6-15 (color): Near-field optical microscopy excitation and energy transport detection of plasmon waveguides. a) Sketch of the experiment. Light emanating from the tip of an illumination-mode near-field optical microscope (NSOM) locally excites a plasmon waveguide. The waveguide guides the electromagnetic energy to a fluorescent nanosphere, and the fluorescence intensity for varying tip positions is collected in the far-field. b) SEM micrograph of a 100 x 100 μm grid consisting of Ag plasmon waveguides.

Power transport away from the directly excited nanoparticles of the plasmon waveguide is probed via the placement of polystyrene nanospheres filled (Molecular Probes Fluospheres F-8801, diameter 110±8 nm) with fluorescent molecules in close proximity to the waveguide structure. For this, the electron beam fabricated plasmon waveguide sample was coated with a thin poly-lysine layer, and the nanospheres were subsequently randomly deposited from an aqueous solution. The fluorescent dyes used show a strong absorption peaking at 580-590 nm near the plasmon resonance wavelength of a single fabricated Ag particle and emit radiation peaking at 610 nm, which is detected in the far-field using a band pass filter and an avalanche photo diode. This scheme enables the observation of energy transport in the following way: first, energy is transferred from the illuminating tip to the plasmon waveguide. The excitation subsequently propagates along the nanoparticle structure and excites a fluorescent nanosphere placed on top of a waveguide at a sufficient distance from the excitation source. Energy transport would result in dye emission even when the tip is located away from the dye, and thus would manifest itself in an increased spatial width of the fluorescence spot of a nanosphere attached to a plasmon waveguide compared to a single free nanosphere.

Figure 6-16 a and b show simultaneously obtained topography and fluorescent NSOM scans of the control area outside the grid (Figure 6-15 b, red box) with single nanospheres only and of the plasmon waveguide grid (Figure 6-15 b, green box) together with fluorescent nanospheres, respectively. The samples were illuminated at the single particle resonance at 570 nm using a NSOM tip with a 100 nm aperture. The scan direction was perpendicular to the plasmon waveguides, and images were built up from

left to right. The fluorescence NSOM spots of nanospheres located on top of plasmon waveguides were examined. In addition, NSOM scans of isolated nanospheres were used as a reference.

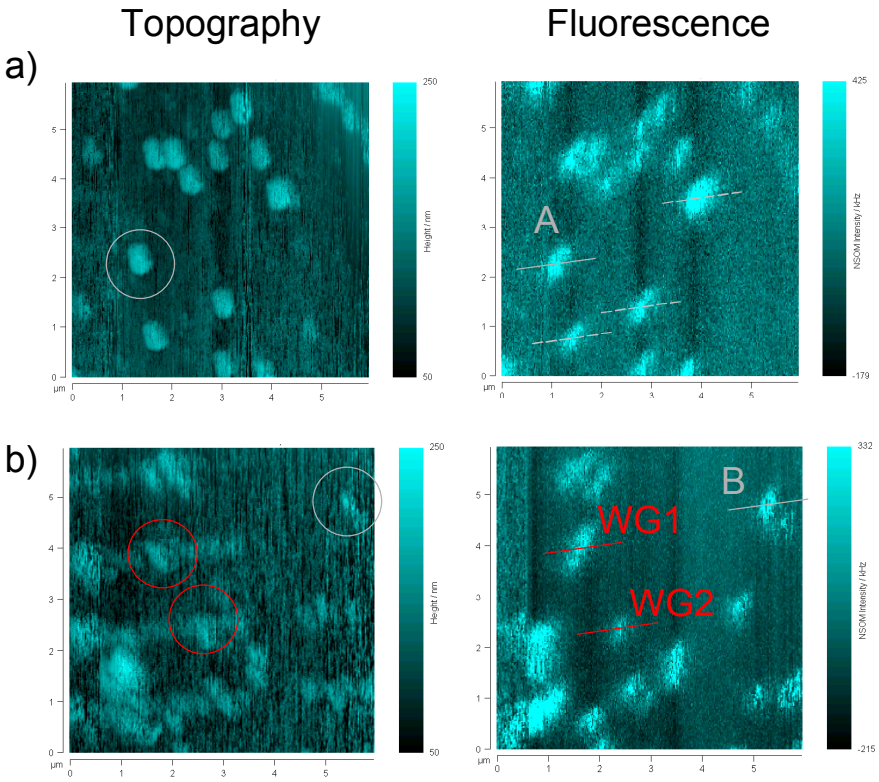

Figure 6-16 (color): Topography and fluorescent NSOM scans. The images show topography and fluorescent NSOM scan of a 6 x 6 μm^2 area consisting of single fluorescent nanospheres (a, area highlighted by red box in **Figure 6-15** b) and an area consisting of fluorescent nanospheres in the vicinity of plasmon waveguides (b, area highlighted by green box in **Figure 6-15** b). The fluorescent intensity of two single nanospheres (gray circles) can be compared to the intensity distribution of nanospheres on top of plasmon waveguides (red circles) using data cuts (gray and red lines) of the fluorescent intensity along the waveguide axis.

Figure 6-16 a shows the scan of the control area consisting of single nanospheres only, which was taken immediately before the scan of the plasmon waveguide area. Single nanospheres are clearly resolved in both the topography and the fluorescent NSOM image, with an arbitrary control particle highlighted (gray circle). Intensity

variations are observed between different fluorescent nanospheres, which are attributed to slight variations in the nanosphere diameter, and the elongation of the fluorescent spots is due to a tip artifact. Figure 6-16 b shows the subsequent scan of a sample area comprising 4 plasmon waveguides in the left part of the image and fluorescent nanospheres. Two nanospheres (highlighted by red circles) are found to be located on top of plasmon waveguides, while one nanosphere at the right side of the scan area (gray circle) is positioned at a distance from a waveguide structure and can thus serve as a further control to ensure that the tip characteristics did not change during the scans. The widths of the fluorescence spots of both the two control nanospheres of Figure 6-16 a and Figure 6-16 b, respectively, and of the nanospheres attached to waveguides of Figure 6-16 b were examined by taking cuts through the NSOM data parallel to the plasmon waveguide direction as highlighted in the fluorescent images.

Figure 6-17 shows averages of five parallel cuts through fluorescent nanosphere spots A, B, WG1 and WG2. Gaussian fits to the data for both the control spheres (black and red lines and data points) and the two spheres attached to plasmon waveguides (green and blue lines and data points) are included. The control nanospheres A and B were scanned before and after scanning the waveguide structures, and in both cases show similar fluorescent full widths at half maximum (FWHM) of 174±17 and 193±23 nm. Analyses of additional control spheres yielded similar widths of 160±12, 205±13, and 188±17 nm, respectively. This confirms that the tip profile did not change appreciably during the scans. By contrast, the fluorescent spots WG1 and WG2 of the nanospheres attached to the plasmon waveguides show a FWHM of 329±14 and 343±27 nm, respectively. The resulting average fluorescence spot FWHM of control spheres is

185±38 nm, while the average width of nanospheres on waveguides is 336±30 nm. The broadening of the fluorescence spots due to the presence of the plasmon waveguide is thus 151±48 nm.

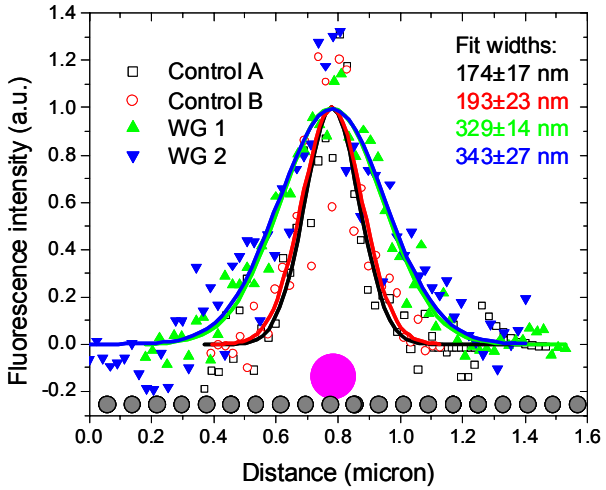

Figure 6-17 (color): Evidence for energy transport in plasmon waveguides via the width of the fluorescence intensity of fluorescent nanospheres. Shown are averages of five parallel cuts along the plasmon waveguide direction through the fluorescent spots highlighted in **Figure 6-16** a and b for both single nanospheres (control A and B, black and red datapoints) and nanospheres located on top of plasmon waveguides (WG 1 and WG2, green and blue datapoints) as depicted in the inset. Gaussian line shape fits to the data show an increased width for nanospheres located on plasmon waveguides.

If the observed broadening of the fluorescent width of waveguide nanospheres is due to transport of electromagnetic energy along the waveguide, no difference in FWHM between control and waveguide nanospheres is expected in the direction perpendicular to the waveguide axis. Indeed, the fitted FWHMs in this direction are found to be equal within the fit error, giving 364±36 nm for control A and B and 352±40 nm for the waveguide nanospheres WG1 and WG2. Note that these values are rather large due to the shape of the tip aperture (see NSOM scans in Figure 6-16).

The increase in the width of the nanosphere fluorescence of about 150 nm for spheres attached to a plasmon waveguide structure can be attributed to local excitation of the plasmon waveguide followed by energy transport along the waveguide toward the fluorescent dye particle. This type of excitation is known to dominate over excitation by direct scattering of the exciting radiation from individual nanoparticles [30]. From Figure 6-17 it is clear that for a free standing nanosphere the fluorescence signal decreases below the dark noise level if the tip is located approximately 200 nm away from the sphere center, while a fluorescent nanosphere attached to a plasmon waveguide can be excited from distances up to 500 nm via the plasmon waveguide. Our results thus provide direct evidence for energy transport over this distance. To obtain quantitative information on the energy decay length we have performed exponential fits on the tails of the fluorescence intensity of the waveguide nanospheres at distances >200 nm away from the nanosphere center. At this distance excitation via the plasmon waveguide dominates over direct dye excitation. These fits yield a decay length of 6 dB/195±28 nm, which is in excellent agreement with the estimate of 6 dB/200 nm obtained from our far-field measurements and theoretical predictions.

6.5 Conclusions and outlook

Using the tip of an illumination-mode NSOM and fluorescent dye nanospheres as detectors, we have shown experimental evidence for energy transport in plasmon waveguides over distances of about 0.5 μm. A number of points regarding the development and the execution of this experiment should be noted.

The detection of energy transport relied on the placement of the fluorescent nanospheres in the near-field of the plasmon waveguide structures. While in the foregoing experiment this was achieved using a random deposition of fluorescent spheres from an aqueous solution, a more controlled placement of the fluorescent nanospheres is desirable. We investigated the feasibility of this using the AFM pushing technique described in section 5.2. Figure 6-18 shows an example of this technique for fluorescent nanospheres with a diameter of 100 nm. Starting with a random deposition of the nanospheres from an aqueous solution as outlined above (Figure 6-18 a), selected particles in close proximity to a plasmon waveguide are pushed to the desired positions, in this case the end of a waveguide (Figure 6-18 b). This way, the energy transport properties of plasmon waveguides could in principle be examined in more detail. However, this technique was found to be only of limited use due to the fact that the nanospheres deformed during the manipulation. The damaged nanospheres further showed considerable smearing during NSOM scans akin to the ones outlined above. In most cases, fluorescent molecules started to stick to the tip, thus making an unambiguous detection of energy transport difficult for the manipulated nanospheres. Nevertheless, the AFM pushing technique could prove to be of value for the manipulation of more rigid detector units such as II-VI semiconductor nanocrystals.

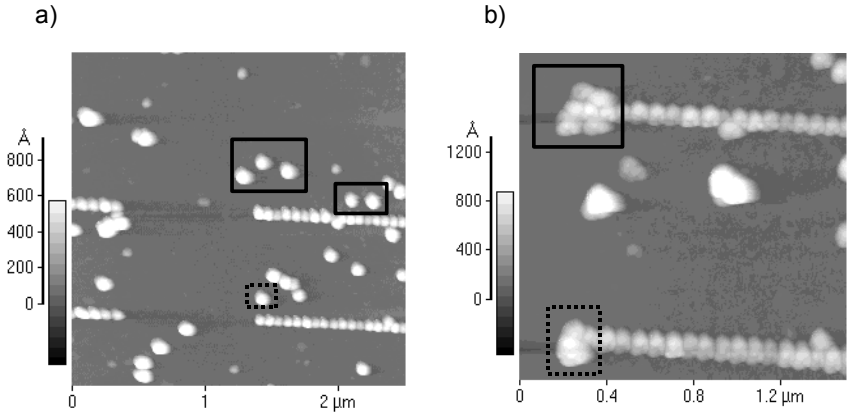

Figure 6-18: Placement of fluorescent nanospheres along plasmon waveguide structures using the tip of an atomic force microscope. Starting from a random deposition (a), the highlighted particles are pushed to the end of two plasmon waveguides (b) using the atomic force microscopy technique described in section 5.2 (courtesy of Sheffer Meltzer).

The second point that should be noted regards the suitability of an NSOM tip as a local excitation source for plasmon waveguides and fluorescent nanospheres. As noted above, our ability to detect energy transport in plasmon waveguides over larger distances than 0.5 µm was severely limited by the fact that even the direct excitation of the fluorescent nanospheres required optical power densities at the damage threshold of the aluminum coated NSOM tips. Furthermore, the detection of subtle differences in the width of the dye fluorescence required the use of a tip with a superior optical resolution for relatively large tip apertures of 100 nm that had to be used to ensure a high throughput for fluorescence excitation. It was found that only a small fraction of the nearly one hundred tips used in our experiments were suitable. Thus, the design of high-throughput NSOM tips is a desireable, and a significant amount of effort is spent to determine tip designs optimized for efficient localized excitations of nanostructures [108, 109]. This together with phase-sensitive fluorescent NSOM detection techniques [110]

could allow for energy transfer detection experiments akin to the one outlined above with a larger dynamic range.

A further complication was caused by the fragility of both our electron beam fabricated plasmon waveguide structures and fluorescent dye nanospheres, which rendered most tips unusable due to the pick-up of fluorescent nanospheres during a single scan. This did not allow for a detailed study of the frequency-dependence of energy transport in plasmon waveguides, which would have required that the area under study be scanned multiple times at different wavelengths. As noted above, the use of more rigid semiconductor nanoparticles as detectors could circumvent this problem and allow for a more detailed study.

As a last point, it should be noted that the tip of an illumination-mode NSOM is clearly not the most efficient way to locally excite plasmon waveguides. Due to the highly divergent beam emerging from the aperture, several propagating modes at different wave vectors **k** will be excited simultaneously, rendering the experimental determination of the dispersion relation difficult. In addition, the analysis of pulsed excitations of plasmon waveguides will be complicated by pulse distortions occurring at the aperture of the tips [111]. Furthermore, light emerging from an NSOM tip aperture is in general not perfectly polarized, leading to the excitation of both longitudinal and transverse plasmon-polariton modes. In fact, even a perfectly polarized point-dipole excitation source would excite differently polarized plasmon modes in a nanoparticle chain when the source is located above the nanoparticle structure as in the NSOM excitation geometry. Figure 6-19 shows snapshots of electric field distributions for this excitation geometry obtained using FDTD simulations where the tip is approximated as

an x-polarized point-dipole located above a plasmon waveguide consisting of nine closely spaced spherical Au nanoparticles oriented along the x-direction. Figure 6-19 a shows the x-component and Figure 6-19 b the z-component of the electric field, respectively, on the same linear color scale at a time t = 26 fs after the pulse-driven point-dipolar source is turned on.

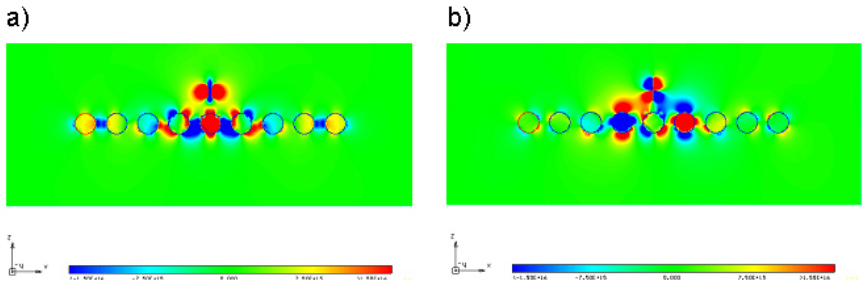

Figure 6-19 (color): Polarization effects of NSOM excitations of plasmon waveguides. The plots show the distribution of the x-component of the electromagnetic field around a plasmon waveguide structure consisting of 9 closely spaced Au nanoparticles. The particle structure is locally excited by an x-polarized point-dipole source located above the particle structure. Shown are time-snapshots of the x- (a) and z-component (b) of the electric field, respectively, showing that the dipole source excites plasmon oscillations of several polarizations in the nanoparticles constituting the waveguides.

As Figure 6-19 b shows, this excitation geometry leads to a significant plasmon oscillation in the z-direction for the nanoparticles adjacent to the particle located underneath the source. It was found that this leads to a significant perturbation of the near-field coupling between the particles in the chain and a lowering of the group velocity of about 25% compared to an excitation geometry where the source is placed on the plasmon waveguide axis as described in section 4.3, which minimizes the excitation of off-axis plasmon oscillations.

In summary, despite theoretical and experimental caveats, the use of the tip of an illumination-mode NSOM as a local excitation source for plasmon waveguides allowed for the direct detection of energy transport in plasmon waveguides over distances of about 0.5 μm.

Chapter 7 Conclusions and outlook

The optical properties of plasmon waveguides consisting of ordered arrays of closely spaced metal nanoparticles were analyzed both theoretically and experimentally. For small spherical particles with a diameter $D << \lambda$, the analytical point-dipole model presented in Chapter 3 allows for the determination of the dispersion properties and group velocities for the transport of electromagnetic energy. However, a strictly point-dipolar interaction model overestimates the interparticle coupling, as was confirmed using FDTD calculations presented in Chapter 4 and far-field polarization spectroscopy on fabricated plasmon waveguides presented in Chapter 5. For spherical Au nanoparticles with a diameter $D = 50$ nm and an interparticle spacing $d = 75$ nm in air, the maximum group velocity for longitudinal excitation is $0.06c$, corresponding to an energy attenuation length of about 6dB/100nm. The guiding properties can be optimized by a change in particle shape and material. As an example, it was shown that spheroidal particles with a 3:1 aspect ratio show up to a threefold increase in group velocity.

For plasmon waveguides fabricated using electron beam lithography as presented in Chapter 5, the polarizability of the substrate leads to a reduced interparticle coupling strength, resulting in an energy decay length estimate of 6dB/30nm for plasmon waveguides consisting of spherical Au particles with the geometry discussed above. In this case, the high loss renders this particular plasmon waveguide geometry of limited use for practical applications. In order to obtain a plasmon waveguide with a larger energy attenuation length, a change in particle material to silver and particle shape to spheroidal particles is necessary. This allows for the fabrication of a plasmon waveguide with

increased interparticle coupling, which together with the reduced plasmon damping of silver nanoparticles allows an energy attenuation length estimate on the order of 6dB/200nm. Indeed, local excitations of these structures using the tip of an illumination mode NSOM together with localized energy detectors in the form of fluorescent nanospheres confirmed energy transport over a distance of about 0.5 μm.

Using FDTD simulations as a design tool, it should be possible to further optimize the energy guiding parameters of plasmon waveguides. For Ag nanoparticles, the increase in interparticle coupling with aspect ratio has to be balanced with a concomitant increase in radiation damping in order to maximize the energy attenuation length. For Au nanoparticles, rods of an aspect ratio of at least 3:1 will ensure an increased plasmon decay time due to a resonance shift of the long axis mode to the near-infrared away from the interband transition edge [69]. At the same time, the volume of the spheroids has to be kept small in order to minimize radiation damping. This way, plasmon waveguides based on Ag and Au nanoclusters with energy attenuation lengths of a couple of hundred nanometers should be possible throughout the visible and near-infrared part of the electromagnetic spectrum. In addition, the use of specially designed substrates for the increase of interparticle plasmon interactions should be explored.

The defining factor concerning the applicability of plasmon waveguides in future highly integrated optical circuits is their submicron energy attenuation length. Plasmon waveguides will thus not be the waveguides of choice for energy transfer over several microns, but could serve as functional end-structures and routing devices operating below the diffraction limit. In the remainder of this thesis, potential applications of plasmon waveguides will be discussed.

In order for plasmon waveguides to find useful applications despite their short energy attenuation lengths it is useful to restate the two properties that render them superior over conventional waveguides. First and foremost, plasmon waveguides allow energy localization and mode sizes on the nanoscale below the diffraction limit of light. In addition, functional devices such as routing structures and all-optical modulators based on interference between phase-shifted plasmon-polariton waves seem feasible. This possibility of attaining a high degree of functionality over distances of a few hundred nanometers would ensure a reasonably high number of functional elements per unit of energy attenuation, which is a more important device characteristic than energy loss per unit length. In this thesis, we have at best hinted at the possibility of functional devices in the form of routing structures such as 90-degree corners and all-optical modulators (sections 2.3, 2.4, 3.3, 4.5). The fabrication of such guiding geometries using electron beam lithography poses no additional challenges, and Figure 7-1 shows an example of a tee structure consisting of spherical Au nanoparticles.

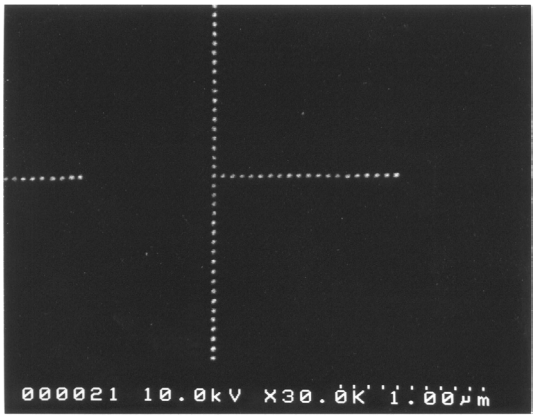

Figure 7-1: A plasmon waveguide tee structure fabricated using electron beam lithography.

The determination of the power transmission coefficients of routing structures and the modulation characteristics of tee interferometers will require a refined excitation and energy transfer detection mechanism using multiple local excitation sources and detectors. Clearly, the tip of an illumination-mode NSOM does not provide the best localized excitation mechanism due to the relatively large aperture and highly divergent beam which leads to an excitation of multiple plasmon-polariton modes as discussed in section 6.5. In integrated optical chips, a coupling of plasmon waveguides to more conventional guiding structures such as dielectric slab waveguides is necessary. The design of subwavelength optical excitation sources is an active field of study at the moment, and promising techniques which could be used as excitation mechanisms for plasmon waveguides such as the beaming of light from subwavelength apertures [112] or the plasmon coupling between a metal nanowire and nanoclusters have been demonstrated [113]. Using the later method, a plasmon waveguide could be excited via the diffraction limited far-field excitation of a metal stripe that is subsequently tapered down to ensure a high spatial overlap between the nanowire and the nanoparticle plasmon modes. In fact, the recent demonstration of composite plasmon resonant nanowires [114] will allow for the fabrication of functional subwavelength nanowire guiding structures which could be combined with metal nanoparticle plasmon waveguides in integrated optical components. The advantage of nanoparticle chains over nanowires is due to the fact that the plasmon resonances of metal nanoparticles are highly tunable, and the controlled excitation of multipolar plasmon excitations in nanoparticles [115] could be employed for mode design. In addition to optical excitation techniques such as apertures and nanowires, the possibility of electrical excitation of plasmon oscillations in metal

nanoparticles is intriguing from the viewpoint of integrated electro-optical devices. However, this particular field of study is still in its infancy [116].

In addition to localized excitation sources, a more robust detection scheme for energy transport than the fluorescent nanospheres described in Chapter 6 is necessary for the optimization of the guiding properties and the investigation of interference effects in modulating structures. As mentioned in section 6.5, rigid semiconductor nanocrystals in combination with AFM pushing techniques show significant promises.

On a last note, a few potential applications of plasmon waveguides will be presented in the hope of stimulating further interest and research in the fascinating field of nanoscale metal optics. Recently, two-dimensional optical elements such as mirrors, beam splitters and interferometers based on plasmon-polaritons on patterned metal films have been demonstrated [117], and nanoscale plasmon waveguides should allow for the fabrication of similar elements operating on the nanoscale.

As an example, the high spatial localization of energy in plasmon waveguides suggests their use as end-structures attached to dielectric waveguides for the channeling of electromagnetic energy to nanoscale or molecular detectors as sketched in Figure 7-2. The large absorption and scattering cross section of metal nanoparticles excited at their surface plasmon resonance frequency should allow for a rather efficient coupling to conventional dielectric slab waveguides. Plasmon waveguides would thus be of interest as energy concentrators, e.g., for Raman or fluorescence spectroscopy or other lab-on-a-chip applications.

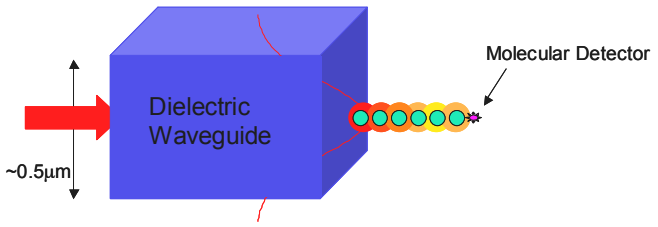

Figure 7-2 (color): Application of a plasmon waveguide as an energy collimator at the end of a conventional dielectric waveguide. The enhanced absorption cross section at resonance leads to a collimation of the beam energy and channels it to a molecule.

Figure 7-3 shows an envisioned application of an all-optical plasmon waveguide switch where a modulation signal is used to control the degree of coupling between two resonant cavities that evanescently couple to the plasmon waveguide. Note that the whole coupling structure could be of lateral dimensions of a few hundred nanometers.

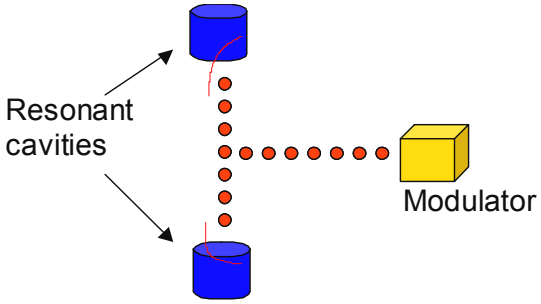

Figure 7-3 (color): Application of a plasmon waveguide as an all-optical modulator linking two resonant cavities. The coupling between the cavities is mediated by a short plasmon waveguide and can be controlled via a modulation source akin to the discussions in Chapter 3.3.

As a last example, Figure 7-4 shows a sketch of plasmon waveguide arrays that evanescently couple two dielectric slab waveguides. The metal nanoparticles are embedded in a photo-addressable birefringent polymer matrix. This way, the dielectric

environment and thus the position of the plasmon resonance can be controlled optically, which in turn allows for an optical control of the coupling between the two dielectric waveguides. Electrical control of the plasmon resonance using electro-optical materials such as liquid crystals has recently been demonstrated [118], which would allow for the fabrication of integrated plasmon waveguide devices with electrically controllable guiding properties.

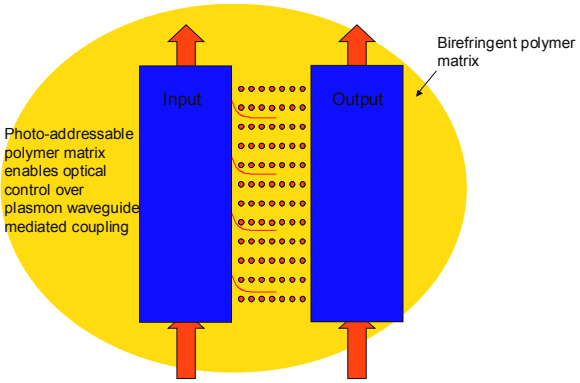

Figure 7-4 (color): Application of a plasmon waveguide as an optically tunable waveguide coupler. Nanoparticle arrays are embedded in an optically addressable birefringent polymer matrix. A far-field illumination of the waveguides changes the refractive index of the surrounding polymer matrix and thus the coupling between the two dielectric waveguides.

In summary, future applications of plasmon waveguides as highly integrated optical coupling and switching devices seem possible. Further research into the amount of optical functionality that can be achieved using metal nanoscale structures should enable a wealth of interesting applications.

Bibliography

1. Saleh, B. E. A. and M. C. Teich, *Fundamentals of Photonics*. 1991, New York: Wiley.
2. Mekis, A., J. C. Chen, I. Kurland, S. Fan, P. R. Villeneuve, and J. D. Joannopoulos, *High transmission through sharp bends in photonic crystal waveguides.* Physical Review Letters **77**(18), 3787-3790 (1996)
3. Moosburger, J., M. Kamp, A. Forchel, S. Olivier, H. Benisty, C. Weisbuch, and U. Oesterle, *Enhanced transmission through photonic-crystal-based bent waveguides by bend engineering.* Applied Physics Letters **79**(22), 3579-3581 (2001)
4. Painter, O., R. K. Lee, A. Scherer, A. Yariv, J. D. O'Brian, P. D. Dapkus, and I. Kim, *Two-dimensional photonic band-gap defect mode laser.* Science **284**(5421), 1819-1821 (1999)
5. Raether, H., *Surface Plasmons on smooth and rough surfaces and on gratings*. 1988, Berlin: Springer.
6. Tominaga, J., C. Mihalcea, D. Büchel, H. Fukuda, T. Nakano, N. Atoda, H. Fuji, and T. Kikukawa, *Local plasmon photonic transistor.* Applied Physics Letters **78**(17), 2417-2419 (2001)
7. Kottmann, J. P. and O. J. F. Martin, *Plasmon resonant coupling in metallic nanowires.* Optics Express **8**(12), 655-663 (2001)

8. Kottmann, J. P., O. J. F. Martin, D. R. Smith, and S. Schultz, *Plasmon resonances of silver nanowires with a nonregular cross section.* Physical Review B **64**, 235402 (2001)

9. Lamprecht, B., J. R. Krenn, G. Schider, H. Ditlbacher, M. Salerno, N. Felidj, A. Leitner, F. R. Aussenegg, and J. C. Weeber, *Surface plasmon propagation in microscale metal stripes.* Applied Physics Letters **79**(1), 51-53 (2001)

10. Weeber, J. C., A. Dereux, C. Girard, J. R. Krenn, and J. P. Goudonnet, *Plasmon polaritons of metallic nanowires for controlling submicron propagation of light.* Physical Review B **69**(12), 9061-9068 (1999)

11. Dickson, R. M. and L. A. Lyon, *Unidirectional plasmon propagation in metallic nanowires.* Journal of Physical Chemistry B **104**, 6095-6098 (2000)

12. Takahara, J., S. Yamagishi, H. Taki, A. Morimoto, and T. Kobayashi, *Guiding of a one-dimensional optical beam with nanometer diameter.* Optics Letters **22**(7), 475-477 (1997)

13. Kreibig, U. and M. Vollmer, *Optical properties of metal clusters*. 1995, Berlin: Springer.

14. Bohren, C. F. and D. R. Huffman, *Absorption and scattering of light by small particles*. 1983, New York: Wiley.

15. Klar, T. A., M. Perner, S. Grosse, G. von Plessen, W. Spirkl, and J. Feldmann, *Surface-plasmon resonances in single metallic particles.* Physical Review Letters **80**(19), 4249-4252 (1998)

16. Quinten, M., A. Leitner, J. R. Krenn, and F. R. Aussenegg, *Electromagnetic energy transport via linear chains of silver nanoparticles.* Optics Letters **23**(17), 1331-1333 (1998)

17. Brongersma, M. L., J. W. Hartman, and H. A. Atwater, *Electromagnetic energy transfer and switching in nanoparticle chain arrays below the diffraction limit.* Physical Review B **62**, R16356 (2000)

18. Craighead, H. G. and G. A. Niklasson, *Characterization and optical properties of arrays of small gold particles.* Applied Physics Letters **44**(12), 1134-1136 (1984)

19. Müller, T., K.-H. Heinig, and B. Schmidt, *Template-directed self-assembly of buried nanowires and the pearling instability.* Materials Science and Engineering C **19**, 209-213 (2002)

20. Hoogenboom, J. P., D. L. J. Vossen, C. Faivre-Moskalenko, M. Dogterom, and A. van Blaaderen, *Patterning surfaces with colloidal particles using optical tweezers.* Applied Physics Letters **80**(25), 4828-4830 (2002)

21. McMillan, R. A., C. D. Paavola, J. Howard, S. L. Chan, N. J. Zaluzec, and J. D. Trent, *Ordered nanoparticle arrays formed on engineered chaperonin protein templates.* Nature Materials **1**, 247-252 (2002)

22. Citrin, D. S., *Coherent transport of excitons in quantum-dot chains: role of retardation.* Optics Letters **20**(8), 901-903 (1995)

23. Poddar, P., T. Telem-Sharif, T. Fried, and G. Markovich, *Dipolar interactions in two- and three-dimensional magnetic nanoparticle arrays.* Physical Review B **66**, 060403(R) (2002)

24. Yariv, A., Y. Xu, R. K. Lee, and A. Scherer, *Coupled-resonator optical waveguide: a proposal and analysis.* Optics Letters **24**(11), 711-713 (1999)

25. Maier, S. A., M. L. Brongersma, and H. A. Atwater, *Electromagnetic energy transport along arrays of closely spaced metal rods as an analogue to plasmonic devices.* Applied Physics Letters **78**(1), 16-18 (2001)

26. Maier, S. A., M. L. Brongersma, and H. A. Atwater, *Electromagnetic energy transport along Yagi arrays.* Materials Science and Engineering C **19**, 291-294 (2002)

27. Maier, S. A., M. L. Brongersma, and H. A. Atwater, *Electromagnetic energy transport along Yagi arrays*, in *MRS Proceedings*. 2001. p. E2.9.

28. Maier, S. A., M. L. Brongersma, P. G. Kik, S. Meltzer, A. A. G. Requicha, and H. A. Atwater, *Plasmonics - a route to nanoscale optical devices.* Advanced Materials **13**(19), 1501-1505 (2001)

29. Link, S. and M. A. El-Sayad, *Shape and size dependence of radiative, non-radiative and photothermal properties of gold nanocrystals.* International Reviews in Physical Chemistry **19**(3), 409-453 (2000)

30. Maier, S. A., P. G. Kik, and H. A. Atwater, *Optical pulse propagation in metal nanoparticle chain waveguides.* Physical Review Letters **submitted**, (2002)

31. Maier, S. A., P. G. Kik, M. L. Brongersma, H. A. Atwater, S. Meltzer, A. A. G. Requicha, and B. E. Koel, *Observation of coupled plasmon-polariton modes of plasmon waveguides for electromagnetic energy transport below the diffraction limit*, in *MRS Proceedings*. 2002. p. Y3.6.

32. Maier, S. A., M. L. Brongersma, P. G. Kik, and H. A. Atwater, *Observation of near-field coupling in metal nanoparticle chains using far-field polarization spectroscopy.* Physical Review B **65**, 193408 (2002)

33. Maier, S. A., P. G. Kik, and H. A. Atwater, *Observation of coupled plasmon-polariton modes in Au nanoparticle chain waveguides of different lengths: Estimation of waveguide loss.* Applied Physics Letters **81**, 1714-1716 (2002)

34. Maier, S. A., P. G. Kik, H. A. Atwater, S. Meltzer, A. A. G. Requicha, and B. E. Koel, *Observation of coupled plasmon-polariton modes of plasmon waveguides for electromagnetic energy transport below the diffraction limit*, in *Proceedings of SPIE*. 2002. pp. 71-82.

35. Maier, S. A., P. G. Kik, M. L. Brongersma, and H. A. Atwater, *Electromagnetic energy transport below the diffraction limit in periodic metal nanostructures*, in *Proceedings of SPIE*. 2001. pp. 22-30.

36. Maier, S. A., P. G. Kik, H. A. Atwater, S. Meltzer, E. Harel, B. E. Koel, and A. A. G. Requicha, *Local detection of electromagnetic energy transport below the diffraction limit in metal nanoparticle plasmon waveguides.* Nature Materials **accepted**, (2003)

37. Atwater, H. A., *Guiding light.* OEmagazine **2**(7), 42-44 (2002)

38. Spector, J. O., *An investigation of periodic rod structures for Yagi aerials.* Journal of IEE **105**, 38-43 (1958)

39. Brown, J. and J. O. Spector, *The radiating properties of end-fire aerials*, in *Proceedings I.E.E.* 1957. pp. 27-34.

40. Sengupta, D. L., *On the phase velocity of wave propagation along an infinite Yagi structure.* IRE Transactions of Antennas and Propagation **AP-7**, 234-239 (1959)

41. Serracchioli, F. and C. A. Levis, *The calculated phase velocity of long end-fire uniform dipole arrays.* IRE Transactions of Antennas and Propagation **AP-7**, 424-434 (1959)

42. Silver, S., *Microwave Antenna Theory and Design*. 1949: McGraw-Hill.

43. Förster, T., *Zwischenmolekulare Energiewanderung und Fluoreszenz.* Annalen der Physik **2**, 55 (1948)

44. Boyd, G. T., Z. H. Yu, and Y. R. Shen, *Photoinduced luminescence from the noble metals and its enhancement on roughened surfaces.* Physical Review B **33**(12), 7923-7935 (1986)

45. Mohamed, M. B., V. Volkov, S. Link, and M. A. El-Sayad, *The 'lightning' gold nanorods: fluorescence enhancement of over a million compared to the gold metal.* Chemical Physics Letters **317**, 517-523 (2000)

46. Wilcoxon, J. P., J. E. Martin, F. Parsapour, B. Wiedenman, and D. F. Kelley, *Photoluminescence from nanosize gold clusters.* Journal of Chemical Physics **108**(21), 9137-9143 (1998)

47. Mie, G., *Beiträge zur Optik trüber Medien, speziell kolloidaler Metallösungen.* Annalen der Physik **25**, 377 (1908)

48. Nolte, D. D., *Optical scattering and absorption by metal nanoclusters in GaAs.* Journal of Applied Physics **76**(6), 3740-3745 (1994)

49. Johnson, P. B. and R. W. Christy, *Optical constants of the noble metals.* Physical Review B **6**(12), 4370-4379 (1972)

50. Mock, J. J., M. Barbic, D. R. Smith, D. A. Schultz, and D. Schultz, *Shape effects in plasmon resonance of individual colloidal silver nanoparticles.* Journal of Chemical Physics **116**(15), 6755-6759 (2002)

51. Sönnichsen, C., S. Geier, N. E. Hecker, G. von Plessen, J. Feldmann, H. Ditlbacher, B. Lamprecht, J. R. Krenn, F. R. Aussenegg, V. Z.-H. Chan, J. P. Spatz, and M. Möller, *Spectroscopy of single metallic nanoparticles using total internal reflection microscopy.* Applied Physics Letters **77**(19), 2949-2951 (2000)

52. Heilweil, E. J. and R. M. Hochstrasser, *Nonlinear spectroscopy and picosecond transient grating study of colloidal gold.* Journal of Chemical Physics **82**(11), 4762-4770 (1985)

53. Palik, E. D., *Handbook of optical constants*. 1985, London: Academic Press.

54. Quinten, M., *Optical constants of gold and silver clusters in the spectral range between 1.5 eV and 4.5 eV.* Zeitschrift für Physik B **101**, 211-217 (1996)

55. Lamprecht, B., J. R. Krenn, A. Leitner, and F. R. Aussenegg, *Resonant and off-resonant light-driven plasmons in metal nanoparticles studied by femtosecond-resolution third-harmonic generation.* Physical Review Letters **83**(21), 4421-4424 (1999)

56. Silva, T. J., *Master's thesis*. 1994, San Diego: UCSD.

57. Kokkinakis, T. and K. Alexopoulus, *Observation of radiative decay of surface plasmons in small silver particles.* Physical Review Letters **28**(25), 1632-1634 (1972)

58. Wokaun, A., J. P. Gordon, and P. F. Liao, *Radiation damping in surface-enhanced Raman scattering.* Physical Review Letters **48**(14), 957-960 (1982)

59. Kreibig, U. and L. Genzel, *Optical absorption of small metallic particles.* Surface Science **156**, 678-700 (1985)

60. Hövel, H., S. Fritz, A. Hilger, U. Kreibig, and M. Vollmer, *Width of cluster plasmon resonances: bulk dielectric functions and chemical interface damping.* Physical Review B **48**(24), 18178-18188 (1993)

61. Lamprecht, B., G. Schider, R. T. Lechner, H. Ditlbacher, J. R. Krenn, A. Leitner, and F. R. Aussenegg, *Metal nanoparticle gratings: influence of dipolar particle interaction on the plasmon resonance.* Physical Review Letters **84**(20), 4721-4724 (2000)

62. Linden, S., J. Kuhl, and H. Giessen, *Controlling the interaction between light and gold nanoparticles: selective suppression of extinction.* Physical Review Letters **86**(20), 4688-4691 (2001)

63. Bozhevolnyi, S. I., J. Erland, K. Leosson, P. M. W. Skovgaard, and J. M. Hvam, *Waveguiding in surface plasmon polariton band gap structures.* Physical Review Letters **86**(14), 3008-3011 (2001)

64. Krenn, J. R., A. Dereux, J. C. Weeber, E. Bourillot, Y. Lacroute, J. P. Goudonnet, G. Schider, W. Gotschy, A. Leitner, F. R. Aussenegg, and C. Girard, *Squeezing the optical near-field zone by plasmon coupling of metallic nanoparticles.* Physical Review Letters **82**(12), 2590-2593 (1999)

65. Jackson, J. D., *Classical Electrodynamics*. 2 ed. 1975, New York: Wiley.

66. Shlager, K. L. and J. B. Schneider, *A selective survey of the finite-difference time-domain literature.* IEEE Antennas & Propagation Magazine **37**(4), 39-56 (1995)

67. Quinten, M. and U. Kreibig, *Absorption and elastic scattering of light by particle aggregates.* Applied Optics **32**(30), 6173-6182 (1993)

68. Gerardy, J. M. and M. Ausloos, *Absorption spectrum of clusters of spheres from the general solution of Maxwell's euqations. II. Optical properties of aggregated metal spheres.* Physical Review B **25**(6), 4204-4229 (1982)

69. Sönnichsen, C., T. Franzl, T. Wilk, G. von Plessen, J. Feldmann, O. Wilson, and P. Mulvaney, *Drastic reduction of plasmon damping in gold nanorods.* Physical Review Letters **88**(7), 077402 (2002)

70. Pendry, J. B., *Negative refraction makes a perfect lens.* Physical Review Letters **85**(18), 3966-3969 (2000)

71. Lakhtakia, A., M. W. McCall, W. S. Weiglhofer, J. Gerardin, and J. Wang, *On mediums with negative phase velocity: a brief overview*. 2002, arXiv.

72. Calander, N. and M. Willander, *Theory of surface-plasmon resonance optical-field enhancement at prolate spheroids.* Journal of Applied Physics **92**(9), 4878-4884 (2002)

73. Scharte, M., R. Porath, T. Ohms, M. Aeschlimann, J. R. Krenn, H. Ditlbacher, F. R. Aussenegg, and A. Liebsch, *Do Mie plasmons have a longer lifetime on resonance than off resonance?* Applied Physics B **73**, 305-310 (2001)

74. Salerno, M., N. Felidj, J. R. Krenn, A. Leitner, and F. R. Aussenegg, *Near-field optical response of a two-dimensional grating of gold nanoparticles.* Physical Review B **63**, 165422 (2001)

75. Schider, G., J. R. Krenn, W. Gotschy, B. Lamprecht, H. Ditlbacher, A. Leitner, and F. R. Aussenegg, *Optical properties of Ag and Au nanowire gratings.* Journal of Applied Physics **90**(8), 3825-3830 (2001)

76. Hsu, J. W. P., *Near-field scanning optical microscopy studies of electronic and photonic materials and devices.* Materials Science and Engineering **33**, 1-50 (2000)

77. Courjon, D. and C. Bainier, *Near field microscopy and near field optics.* Reports on Progress in Physics **57**, 989-1028 (1994)

78. Yang, T. J., G. A. Lessard, and S. R. Quake, *An apertureless near-field microscopy for fluorescence imaging.* Applied Physics Letters **76**(3), 378-380 (2000)

79. Bethe, H. A., *Theory of diffraction by small holes.* Physical Review **66**(7,8), 163-182 (1944)

80. Bouwkamp, C. J., *On Bethe's theory of diffraction by small holes.* Philips Research Reports **5**, 321-332 (1950)

81. Bouwkamp, C. J., *On the diffraction of electromagnetic waves by small circular disks and holes.* Philips Research Reports **5**, 401-422 (1950)

82. Emonin, S., T. Held, N. Richard, O. Hollrichter, and O. Marti, *Multicolor images acquistion by scanning near-field optical microscopy.* Journal of Applied Physics **90**(9), 4820-4824 (2001)

83. Seidel, J., Grafström, C. Loppacher, S. Trogisch, F. Schlaphof, and L. M. Eng, *Near-field spectroscopy with white-light illumination.* Applied Physics Letters **79**(14), 2291-2293 (2001)

84. Safvi, S. A., J. Liu, and T. F. Kuech, *Spatial resolution of localized photoluminescence by near-field scanning optical microscopy.* Journal of Applied Physics **82**(11), 5352-5359 (1997)

85. Hecht, B., H. Bielefeldt, D. W. Pohl, L. Novotny, and H. Heinzelmann, *Influence of detection conditions on near-field optical imaging.* Journal of Applied Physics **84**(11), 5873-5882 (1998)

86. Sekatskii, S. K. and G. Dietler, *Near-field optical excitation as a dipole-dipole energy transfer process.* Journal of Microscopy **194**, 255-259 (1999)

87. Specht, M., J. D. Pedarnig, W. M. Heckl, and T. W. Hänsch, *Scanning plasmon near-field microscope.* Physical Review Letters **68**(4), 476-479 (1992)

88. Hecht, B., H. Bielefeldt, L. Novotny, Y. Inouye, and D. W. Pohl, *Local excitation, scattering, and interference of surface plasmons.* Physical Review Letters **77**(9), 1889-1892 (1996)

89. Markel, V. A., V. M. Shalaev, P. Zhang, W. Huynh, L. Tay, T. L. Haslett, and M. Moskovits, *Near-field optical spectroscopy of individual surface-plasmon modes in colloid clusters.* Physical Review B **59**(16), 10903-10909 (1999)

90. Leveque, G., G. Colas des Francs, C. Girard, J. C. Weeber, C. Meier, C. Robilliard, R. Mathevet, and W. John, *Polarization state of the optical near field.* Physical Review E **65**, 036701 (2002)

91. Weeber, J. C., A. Dereux, C. Girard, G. Colas des Francs, J. R. Krenn, and J. P. Goudonnet, *Optical adressing at the subwavelength scale.* Physical Review E **62**(5), 7381-7388 (2000)

92. Lewis, A., K. Lieberman, N. Ben-Ami, G. Fish, E. Khachatryan, U. Ben-Ami, and S. Shalom, *New design and imaging concepts in NSOM.* Ultramicroscopy **61**, 215-220 (1995)

93. Lieberman, K., N. Ben-Ami, and A. Lewis, *A fully integrated near-field optical, far-field optical, and normal-force scanned probe microscopy.* Review of Scientific Instruments **67**(10), 3567-3572 (1996)

94. Liu, A., A. Rahmani, G. W. Bryant, L. J. Richter, and S. J. Stranick, *Modeling illumination-mode near-field optical microscopy of Au nanoparticles.* Journal of the Optical Society of America A **18**(3), 704-716 (2001)

95. Richter, L. J., C. E. Jordan, R. R. Cavanagh, G. W. Bryant, A. Liu, and S. J. Stranick, *Influence of secondary tip shape on illumination-mode near-field scanning optical microscopy images.* Journal of the Optical Society of America A **16**(8), 1936-1946 (1999)

96. Hecht, B., H. Bielefeldt, Y. Inouye, D. W. Pohl, and L. Novotny, *Facts and artifacts in near-field optical microscopy.* Journal of Applied Physics **81**(6), 2492-2498 (1997)

97. Walford, J. N., J. A. Porto, R. Carminati, J.-J. Greffet, P. M. Adam, S. Hudlet, J.-L. Bijeon, A. Stashkevich, and P. Royer, *Influence of tip modulation on image formation in scanning near-field optical microscopy.* Journal of Applied Physics **89**(9), 5159-5169 (2001)

98. Gucciardi, P. G. and M. Colocci, *Different contrast mechanisms induced by topography artifacts in near-field optical microscopy.* Applied Physics Letters **79**(10), 1543-1545 (2001)

99. Jordan, C. E., S. J. Stranick, L. J. Richter, and R. R. Cavanagh, *Removing optical artifacts in near-field scanning optical microscopy by using a three-dimensional scanning mode.* Journal of Applied Physics **86**(5), 2785-2789 (1999)

100. Metiu, H., *Surfaced enhanced spectroscopy.* Progress in Surface Science **17**, 153-320 (1984)

101. Hamann, H. F., M. Kuno, A. Gallagher, and D. J. Nesbitt, *Molecular fluorescence in the vicinity of a nanoscopic probe.* Journal of Chemical Physics **114**(19), 8596-8609 (2001)

102. Knobloch, H., H. Brunner, A. Leitner, F. R. Aussenegg, and W. Knoll, *Probing the evanescent field of propagating plasmon surface polaritons by fluorescence and Raman spectroscopies.* Journal of Chemical Physics **98**(12), 10093-10095 (1993)

103. Das, P. C. and A. Puri, *Energy flow and fluorescence near a small metal particle.* Physical Review B **65**, 155416 (2002)

104. Andrew, P. and W. L. Barnes, *Molecular fluorescence above metallic gratings.* Physical Review B **64**, 125405 (2001)

105. Ditlbacher, H., J. R. Krenn, N. Felidj, B. Lamprecht, G. Schider, M. Salerno, A. Leitner, and F. R. Aussenegg, *Fluorescence imaging of surface plasmon fields.* Applied Physics Letters **80**(3), 404-406 (2002)

106. Fujihira, M., H. Monobe, N. Yamamoto, H. Muramatsu, N. Chiba, K. Nakajima, and T. Ataka, *Scanning near-field optical microscopy of fluorescent polystyrene spheres with a combined SNOM and AFM.* Ultramicroscopy **61**, 271-277 (1995)

107. Höppener, C., D. Molenda, H. Fuchs, and A. Naber, *Simultaneous topographical and optical characterization of near-field optical aperture probes by way of imaging fluorescent nanospheres.* Applied Physics Letters **80**(8), 1331-1333 (2002)

108. Krug II, J. T., E. J. Sanchez, and X. S. Xie, *Design of near-field optical probes with optical field enhancement by finite difference time domain electromagnetic simulation.* Journal of Chemical Physics **116**(24), 10895-10901 (2002)

109. Song, K.-B., J. Kim, and K.-H. Park, *Technique to enhance the throughput on a near-field aperture by the use of the self-focusing effect.* Applied Physics Letters **80**(16), 2827-2829 (2002)

110. Sekatskii, S. K., G. T. Shubeita, and G. Dietler, *Time-gated scanning near-field optical microscopy.* Applied Physics Letters **77**(14), 2089-2091 (2000)

111. Mitrofanov, O., M. Lee, L. N. Peiffer, and K. W. West, *Effect of chirp in diffraction of short electromagnetic pulses through subwavelength apertures.* Applied Physics Letters **80**(8), 1319-1321 (2002)

112. Lezec, H. J., A. Degiron, E. Devaux, R. A. Linke, L. Martin-Moreno, F. J. Garcia-Vidal, and T. W. Ebbesen, *Beaming light from a subwavelength aperture.* Science **297**, 820-822 (2002)

113. Krenn, J. R., J. C. Weeber, A. Dereux, E. Bourillot, J. P. Goudonnet, G. Schider, A. Leitner, F. R. Aussenegg, and C. Girard, *Direct observation of localized surface plasmon coupling.* Physical Review B **60**(7), 5029-5033 (1999)

114. Mock, J. J., S. J. Oldenburg, D. R. Smith, D. A. Schultz, and S. Schultz, *Composite plasmon resonant nanowires.* Nano Letters **2**(5), 465-469 (2002)

115. Krenn, J. R., G. Schider, W. Rechberger, B. Lamprecht, A. Leitner, and F. R. Aussenegg, *Design of multipolar plasmon excitations in silver nanoparticles.* Applied Physics Letters **77**(21), 3379-3381 (2000)

116. Nilius, N., N. Ernst, and H.-J. Freund, *Tip influence on plasmon excitations in single gold particles in an STM.* Physical Review B **65**, 115421 (2002)

117. Ditlbacher, H., J. R. Krenn, G. Schider, A. Leitner, and F. R. Aussenegg, *Two-dimensional optics with surface plasmon polaritons.* Applied Physics Letters **81**(10), 1762-1764 (2002)

118. Müller, J., C. Sönnichsen, H. von Poschinger, G. von Plessen, T. A. Klar, and J. Feldmann, *Electrically controlled light scattering with single metal nanoparticles.* Applied Physics Letters **81**(1), 171-173 (2002)